Nanoscale

REVIEW

View Article Online
View Journal | View Issue

Cite this: *Nanoscale*, 2026, **18**, 537

Advances in visible and ultraviolet self-powered photodetectors: exploring 2D materials and Janus heterostructures

Umer Ahsan,[a] Ehsan Elahi,[a] Abdul Sattar,[b] Kalyan Jyoti Sarkar,[a] Muhammad Asad,[a] Hina Mustafa,[b] Muhammad Irfan,[c] Muhammad Ammar Sabar[d] and Zdenek Sofer *[a]

Self-powered photodetectors (SPPDs) are becoming crucial in energy-efficient optoelectronics. They operate without any external power, utilizing built-in electric fields and photovoltaic effects. Their applications range from wearable sensors to optical communication. Recent advancements in 2D materials, perovskites, Janus heterostructures, Schottky junctions, and flexible substrates have significantly improved their responsivity, broadband absorption, and mechanical flexibility. However, challenges in stability, large-scale fabrication, and charge transport efficiency remain, hindering their commercial adoption. This review critically examines the recent progress in heterostructure-based SPPDs, addressing key challenges in their device performance, material integration, and scalability. While previous researches have explored individual material platforms, gaps remain in long-term stability, interface defects, and large-area processing. This study highlights the potential of novel fabrication techniques and doping strategies to enhance the detection performance by analyzing advances in interface engineering, band alignment, and hybrid material systems. Results highlight the promise of self-driven optimization, flexible electronics, and photodetectors based on quantum materials, offering valuable insights into the future trajectory of self-powered optoelectronics. This review highlights the existing challenges and opportunities, offering insights for future advancements in high-performance, self-sustaining photodetection technologies.

Received 9th August 2025,
Accepted 7th October 2025

DOI: 10.1039/d5nr03378k

rsc.li/nanoscale

1. Introduction

In the realm of modern technology, photodetectors play a pivotal role, converting optical energy into electronic energy, which is utilised in various electronic devices.[1–3] This technology is widely used in image processing applications,[1,2] optical communication,[3,4] and other domains, thereby playing an indispensable role in our daily lives. Photodetectors are fast and sensitive devices for efficient light detection at various wavelengths, enhancing optical communication systems. For instance, the photodetectors on smartphones enable the screen to adjust to the surrounding brightness conditions[8] automatically. In cameras, charge-coupled devices are used to ensure that precise images are captured. Night observation and security surveillance require infrared detectors.[5,6] Additionally, photodetectors are utilized to obtain high-quality medical images.[7,8] Depending on the device design, photodetectors (PDs) often require an external bias to allow the mobility of photogenerated charge carriers (electrons and/or holes) for photocurrent generation.[9,10] However, by adjusting the energy band gaps of individual materials, it is possible to establish an internal electric field between them and to utilize it as the energy for the photodynamic carriers. Self-powered photodetectors operate without any external bias and are considered technologically essential for low-power electronics, such as image sensing and optical communications.[11,12] Self-powered photodetectors (SPPDs) rely on several fundamental mechanisms that allow them to operate autonomously without requiring any external power source. The core principle behind their functionality is the photovoltaic effect, which enables the conversion of optical energy into electrical energy. In self-powered devices, photogenerated electron–hole pairs are separated by built-in electric fields, which drive the flow of carriers and generate a photocurrent. For materials like transition metal dichalcogenides (TMDCs), such as MoS_2 and WSe_2, the internal electric fields are generated at the interfaces between

[a]*Department of Inorganic Chemistry, University of Chemistry and Technology Prague, Technická 5, Prague 616628, Czech Republic. E-mail: Zdenek.Sofer@vscht.cz*
[b]*Department of Physics, COMSATS University Islamabad, Lahore Campus, Lahore 54000, Pakistan*
[c]*College of Engineering Physics, Shenzhen Technology University, Shenzhen 518118, China*
[d]*Department of Automotive Engineering, University of Bedfordshire, Luton Campus, UK*

the material and the electrodes, particularly through the formation of asymmetric Schottky junctions. As a result, self-powered photodetectors not only significantly lower the unit cost of the device but also drastically reduce the overall system size.[13–16] This is, nevertheless, constrained by the rigorous criteria for excellent performance in portable applications, which preclude the use of traditional methods involving bulk semiconductors in the construction of SPPDs.[17] Moreover, new methodologies and material choices are necessary for state-of-the-art SPPDs to overcome their limitations and increase their applicability. The research presented in this review is significant as it provides a comprehensive overview of the advancements in self-powered photodetectors, shedding light on their potential applications and guiding future innovations in the field.

2. Overview of 2D materials for SPPDs

Ultrathin PDs have been used as photo-absorbers employing two-dimensional materials (2D) such as graphene and TMDCs.[18,19] Due to their efficient surface-to-volume ratios and compatibility with standard lithography techniques in lateral dimensions, 2D materials can be effectively utilized in electronics or signal processing applications. Currently, researchers are exploring new materials including graphene and other 2D materials, which exhibit strong covalent intralayer bonding and weak van der Waals (vdW) interlayer bonding. It is further divided into various material groups such as graphene, TMDCs (MoS_2, WSe_2, and $MoSe_2$), semiconducting dichalcogenides ($MoTe_2$ and WTe_2), layered semiconductors (GaSe, GaS, GaTe, and InSe),[20,21] complex molecular structures such as perovskites[22] and 2D organic molecular crystals (OMCs).[23,24] The 2D materials possess exceptional electrical characteristics, making them highly promising for advanced photodetectors due to their flexibility. Due to their excellent mechanical strength and optical transparency, 2D materials such as graphenes are auspicious for fabricating transparent electrodes and flexible optoelectronic devices.[25] For PDs, graphene is the first 2D material due to its outstanding electrical properties including a high mobility up to 200 000 $cm^2 V^{-1}$ and a bandwidth up to 40 GHz.[26–29] However, the absence of a bandgap in graphene and the associated generation of dark current result in significant noise contributions to the signal, significantly limiting its application in further photodetection. Recently, there has also been considerable interest in 2D TMDCs[13] due to their high mobility,[30] considerable absorbance,[31–33] and adjustable bandgap.[34] Furthermore, the flexibility and transparency of the atomically thin TMDCs are excellent and, thus, hold great promise for future wearable photodetectors and machine vision systems.[35] TMDCs with intrinsically passivated surfaces, lacking dangling bonds, offer a straightforward method for fabricating constructed heterostructures. TMDCs have great potential for broad applications in photodetection across the terahertz (THz), infrared (IR), visible, and ultraviolet (UV) spectral ranges, with the band topology adjustable by varying the number of layers.[36–38]

2.1. Molybdenum disulfide (MoS_2)

MoS_2 has recently garnered much interest among the TMDCs in photodetection. Due to the multiple layers in 2D materials like MoS_2, the bandgap can be modified, and a small amount of internal dielectric shielding is present. The group VI TMDCs contain a layer of transition metal atoms (Mo and W) sandwiched between two layers of chalcogen atoms (S, Se, and T).[39] An indirect energy band gap of around 1.2 eV[11] defines the bulk electronic structure of MoS_2. At the monolayer limit, like other group VI TMDCs, MoS_2 modifies its energy band structure. This adaptation enables a direct electronic transition from the K and K' points of the Brillouin zone and a 1.8 eV band gap.[40] In addition, TMDCs are reported to exhibit large spin–orbit coupling (SOC),[30,39,41] which is related to the d-orbitals of transition metals. The SOC removes the degeneracy at the valence band, producing two higher energy levels at the K and K' points. A separation of 160 meV in the energy of these maxima is observed in a monolayer MoS_2 material.[41] There is broken degeneracy in MoS_2, and its potential use in optoelectronic applications within the scope of valleytronics is enabled by the presence of this broken degeneracy. This characteristic makes them suitable as stable carriers in electronic device applications.[42–44]

2.2. Molybdenum diselenide ($MoSe_2$)

$MoSe_2$ is a new member of the family of TMDC materials. The bulk exhibits an indirect band gap of 1.1 eV,[45] which can be reduced to 1.5 eV[46] through exfoliation to a few layers. This material shows promise for near-infrared photodetection and a layered crystal similar to that of MoS_2 in a monolayer. However, its broader bandgap distinguishes $MoSe_2$ from MoS_2, which affects the properties of its optical absorption and photoluminescence. The strong PL and high charge carrier mobility of this material make it a promising candidate for various optoelectronic applications. $MoSe_2$ exhibits favorable electrical characteristics and efficient light absorption across visible to near-infrared wavelengths. It has demonstrated significant potential for developing advanced devices, including field-effect transistors, phototransistors, and photodetectors.[47]

2.3. Tungsten disulfide (WS_2)

Another 2D material, WS_2, has attracted significant interest due to its high surface-to-volume ratio, adjustable bandgap, and excellent electronic properties.[48] This is because the direct bandgap in the monolayer form is around 2.0 eV, which explains the remarkable optical characteristics of WS_2, especially the intense absorption in the visible range. As the thickness increases, it changes to an indirect bandgap of 1.4 eV. For example, in the monolayer form, the quantum yield for the photoluminescence of WS_2 is high, and such a material is highly desirable for optoelectronic applications.[49]

2.4. MXene

Two-dimensional transition metal carbides, nitrides, or carbonitrides (MXene) also attracted significant attention as a

potentially vast family of inorganic materials. They possess a general formula. $M_{n+1}X_nT_x$ is the general notation of MXene in which M denotes an early transition metal (by multiples or by a random sequence), X is the carbon and/or nitrogen element, and T_x is the surface termination (reactive end groups, halogens, and chalcogens). Their metallic conductivity facilitates efficient charge transport, which is essential for fast response times in photodetectors. Additionally, the large surface area and hydrophilic nature of MXenes enable facile integration with other semiconducting nanomaterials, allowing for the design of hybrid structures with enhanced light absorption and improved photogenerated carrier separation. The presence of surface terminal groups (such as OH, F, and O) can be tailored to modulate the work function, making MXenes versatile as electrodes, transport layers, or even active materials in self-powered photodetectors. Their ability to operate over a broad spectral range, from UV to NIR, further reinforces their role in next-generation, flexible, and high-performance photodetectors.[50]

2.5. Black phosphorus (BP)

Another type of 2D material, black phosphorus (BP), is a promising material for PDs with a broad band owing to its direct bandgap, which is dependent on the thickness from around 0.3 eV in bulk[51] to about 2 eV in monolayer.[36] This may lead to high-performance optoelectronic devices in the medium wavelength infrared (MWIR) region. BP thin films support monolithic integration with conventional electronic materials, such as silicon, and can be deposited on any substrate, including typical ones like flexible substrates.[52,53] Traditional narrow-band gap semiconductors with bulk lattices such as mercury cadmium telluride (CdTe) and indium arsenide (InAs) are not flexible enough for future system integration. BP thin films exhibit a small bandgap compared to the zero bandgap, which gives rise to low dark current and low-noise photodetection. For example, BP thin films (generally in the order of 10–20 nm for our photodetectors) possesses a bandgap comparable to that of the bulk form (~0.3 eV) and superior photon absorption to 2D single layers of graphenes or transition metal dichalcogenides.[54] However, many BP-based photodetectors have low responsivity, making it difficult to detect weak optical signals.

2.6. Perovskites

The development of perovskite materials has transformed the field of self-powered photodetectors (SPPDs), opening up new opportunities for low-energy optoelectronic devices. Perovskites exhibit remarkable optoelectronic characteristics including effective charge transfer, adjustable bandgaps, and high light absorption coefficients. The creation of adaptable and energy-efficient sensing technologies becomes possible due to these characteristics, which enable photodetection without the need for external power sources. Specifically, hybrid organic–inorganic perovskites, which benefit from straightforward fabrication procedures and substrate versatility, have demonstrated exceptional responsivity and quick response times in self-powered modes.[55,56] Additionally, recent developments that combine perovskites with layered heterostructures and ferroelectric materials have greatly improved the stability and detection performance of devices in real-world scenarios.[55,57] These developments position perovskite-based SPPDs at the forefront of next-generation applications, such as high-resolution imaging, optical communication, and wearable electronics.

2.7. Janus materials

Recent discoveries have also revealed that Janus materials offer enhanced freedom to optically respond anisotropically in monolayer 2D materials. These 2D Janus materials have asymmetrical surface characteristics with different functionalities on the two sides, such as MoSSe.[58] This unique structure exhibits outstanding optical characteristics, yielding strong light absorption, enhancing the nonlinear optical response, and featuring adjustable band gaps. These are exciting properties of Janus materials for photodetectors and optical systems. Additionally, their adjustable optical properties enable them to be developed into optical devices including modulators and sensors with specific designs tailored to certain purposes.[59]

3. Device structure and operation

vdW heterostructures have become a subject of current interest among researchers for the rapid rise of 2D materials for their applications in photodetectors.[34,60,61] Fabricating a unique variety of van der Waals heterostructures (vdWHs) enables the realization of many optoelectronic devices with highly desirable functionalities and performances by circumventing lattice mismatches.[62–65] The interlayer band alignment in 2D vdW heterojunctions can facilitate interlayer photoexcitation,[67,68] enhance charge separation,[69–73] and broaden the photoexcitation spectrum.[66–68] vdWHs enable the combination and enhancement of 2D materials, facilitating the development of innovative functionalities and performance augmentation in optoelectronic devices.[69–72] Recently, devices using vdW materials with variable polarities have drawn intensive attention. Changing polarity can improve many functions in specific devices including light-emitting diodes, memory transistors, and logic circuits.[73–77] Two-dimensional materials exhibit high responsivity and rapid response times, making them excellent light detectors.[78,79] However, to date, most 2D material-based photodetectors are designed to operate with an external power supply, which is utilized by photogenerated carriers to generate a photocurrent.[80,81] An interesting area of research for next-generation nanodevices is the development of self-powered optoelectronic devices that can operate autonomously, wirelessly, and sustainably.

Next-generation electrical devices require a special type of self-powered photodetector that does not use an external power source, is lightweight, and consumes very little power despite its small dimensions. This type of PD is currently being extensively researched. It will increase the flexibility of devices while reducing their dimensions and weight. On the

other hand, self-sustainable, junction-based nanotechnologies enable the development of extremely small, flexible, and energy-efficient nanosystems. SPPDs possess an inherent electric field at an intrinsic potential at the p–n junction, offering improved photodetection characteristics and auto-photo switching features. Generally, the materials used and the device's configuration play a significant role in determining its self-sustaining capability. Materials with tailored band gaps, as wide bandgap semiconductors, are the best because they can generate robust built-in electric fields, have a large surface area for efficient photon absorption, and collect charges effectively through wide separation at the interface. The detailed design includes material configuration and electrical connections to detect the weak optical signal. The performance of SPPDs can be evaluated by the ratio of photocurrent to dark current, detectivity, responsivity, and noise equivalent power. The prospect of utilizing SPPDs to remotely sense, monitor the environment, and use renewable energy systems is numerous. They are based on the photovoltaic effect of semiconductors, that is, the production of electron–hole pairs in them upon exposure to light. The 2D material-based SPPDs are highly efficient and versatile, and can be utilized in optoelectronic devices, photodetectors, and photodiodes. SPPDs work without external voltage, achieve low dark currents, and operate with self-powered light sensing. Additionally, they can rapidly separate electron–hole pairs, exhibit fast optical response, and possess good photoelectric conversion efficiency. Moreover, these properties decrease the required energy consumption and facilitate external circuit design, providing a promising foundation for the future use of photoelectrochemical (PEC)-type devices.[82,83] The evolution of SPPDs has followed material innovation, beginning with conventional silicon-based designs and progressing to graphene, which offered superior carrier mobility but lacked a bandgap. The limitations of graphene led to the adoption of TMDCs, which offer tunable band gaps and improved light absorption.[84] The need for enhanced conductivity and flexibility was introduced by MXenes,[93] while Janus structures addressed the need for intrinsic asymmetry to internal electric fields.[85] Hybrid systems, particularly those integrating perovskites and PEDOT:PSS, have further pushed device performance by combining the strengths of organic and inorganic systems,[86] as shown in Table 1. Over the past couple of years, several SPPDs utilising Janus materials have displayed outstanding photodetection devices, as shown in Table 2. The timeline in Fig. 1 illustrates the development of SPPDs from 2017 to 2025, highlighting various material advancements and heterostructure innovations.

This will serve as a systematic analysis of modern SPPDs and a brief evaluation of various photodetectors as a basis for innovative device designs in advanced quantum photonics. For instance, the review will classify SPPD technologies according to Schottky-based devices, individual 2D materials (including MXenes and p–n junctions in homojunction and hetero junction configurations), Janus materials, flexible substrates, and perovskites, and discuss each of the categories individually. It will also examine the influence of material interfaces and interlayer coupling on the performance metrics of SPPDs, particularly in terms of responsivity and response time. Special emphasis will be placed on the integration potential of these devices within existing photonic platforms. It will pursue the characterisation of performance and manufacturing procedures for each category.

4. Preparation and synthesis of self-powered photodetectors

The fabrication of SPPDs relies on material-specific synthesis techniques that guarantee superior crystal quality, pristine interfaces, and scalability of the devices. Multiple methods have been developed to create junctions that facilitate intrinsic electric fields for self-powered operation, dependent upon the dimensionality and chemical capabilities of the active layers, including 2D TMDCs, MXenes, Janus materials, or perovskites.

4.1 Mechanical exfoliation

Mechanical exfoliation stands out as a highly effective and commonly employed method for the preparation of 2D layered materials such as MoS_2, WSe_2, and graphenes. This technique involves the careful peeling of high-quality single or few-layer flakes from a bulk crystal using adhesive tape, followed by

Table 1 Comparison of emerging materials for self-powered photodetector applications

Material type	Key features	Advantages	Limitations	SPPD role
Graphene	High mobility, zero bandgap[96]	Fast carrier transport, flexibility[97]	High dark current, low absorption	Transparent electrodes, hybrid layers[98]
TMDCs (MoS_2, WSe_2)	Tunable bandgap, strong light absorption	Broad spectral response, good flexibility	Lower mobility than graphene	Active layer in SPPDs[99]
MXenes	High conductivity, tunable work function	Strong built-in field, hybrid-compatible	Sensitive to oxidation	Electrodes, light absorbers[100]
Janus materials	Asymmetrical structure, intrinsic field	Self-driven separation, polarization sensitivity	Synthesis complexity	Standalone or hybrid photoactive layer[101]
Perovskites	High absorption, solution-processable	High EQE, low cost	Poor long-term stability	Light-harvesting layer in hybrid SPPDs[102]
Flexible materials	Conductive polymer	Enhances hole transport, flexible	Low intrinsic mobility	Transport layer, flexibility enhancement[103,104]

Table 2 Assessment summary of various SPPDs

Category	Material	Performance					Bias [V]	Ref.
		Wavelength (nm)	Response time [τ_r/τ_d] [μs]	Responsivity [A W^{-1}]	D^* [Jones]	E [%]		
Graphene-based SPPD	Gr/WSe_2/$NbSe_2$	405–980	80/72	0.287	5.3×10^{11}	88	00	105
	TETA-Gr/WS_2/$LaVO_3$	300–850	/435		2.1×10^{10}		0	106
	WS_2/graphene/MoS_2	405	44/52	220	1.2×10^{13}	6.7×10^4	2.5	107
TMDC-based SPPD	GeSe/WS_2/MoS_2		2400/5200	0.014	7.3×10^8	4.1	0	108
	CuI/MoS_2	405–1010		0.386			0	109
	PVA-MoS_2/n-Si	365, 395, 590, 850		0.48	5.71×10^{12}	100.8	−2	110
	$MoSe_2$/n-GaN (NIR, 5 V)	Near infrared		1.6	1.26×10^8		5	84
	$NbOI_2$/$MoSe_2$			0.1013			0	111
	GeSn-Ge MQW HPT	1550	81.3/73.1	1.3	2.6×10^{10}		2	112
	$PtSe_2$/MoS_2 vdW	405–980	20 000	0.0334		1880	0	113
	MnS/MoS_2	Visible (532 nm)	20 000/30 000	1.31		316	0	114
	Au-MoS_2/WO_3	UV-visible-NIR	55 000/48 000	0.72		226	2	115
Mxene-based SPPD	Te/Mxene	368–1006	12 200/26 500	1.84	4.83×10^{12}		0	116
	$CsPbCl_3$@$Ti_3C_2T_x$	UV	1.47/1.52		1.71×10^{11}		0	117
	MXene/GaN	UV	31 000/29 000	0.081			0	118
	Nb_2CT_x/AlGaN	254	21 000/22 000	0.10185			0	50
	$BiVO_4$/MXene	447	8000/14 000	0.7902			0	119
	MXene/GaN	382		48.6	5.9×10^{12}	543	0	120
Homojunction PN	WS_2				5.8×10^{11}		0	121
junction-based SPPD	WSe_2	550–80		0.2167			0	121
	$MoTe_2$	660			3.87×10^{11}		0	122
Heterojunction PN	MoS_2/$PdSe_2$/WSe_2	405–1550	190/74	0.56	5.63×10^{11}		0	123
junction based SPPD	$NbSe_2$/$MoSe_2$	405–980	180/80	64.92 at 650 nm	2.39×10^{14}		0	93
	$TaSe_2$/WS_2/$TaSe_2$	488, 532, 633	43/54	0.292	2.43×10^{11}	57	0	94
	Bi_2Se_3/Ga_2O_3	254/1000	<50	0.175 mA W^{-1} at 365 nm	1.58×10^{10}		0	124
	In_2Se_3/WSe_2/ReS_2		250% faster than In_2Se_3/WSe_2	438			0	125
Janus-based SPPD	$PdSe_2$/2H-$MoTe_2$	532		7.3×10^3	8.5×10^{12}	56.73	0	126
	CrSBr	514		0.26	3.4×10^8		0	127
	WSe_2/Ta_2NiSe_5/WSe_2	400–1550	420/640			85.5		128
	GeSe/WS_2/MoS_2		2400/5200	14	7.3×10^8	4.1	0	108
Flexible substrate	GaN/SnS_2/SnSSe	365		314.96	2.0×10^{14}	10.7×10^4	0.3	129
-based SPPD	CdTe/MoS_2		44.8/134.2	270.3	5.84×10^{11}		0	130
	TFSA-doped Gr/WS_2	UV to visible		0.14	2.5×10^{15}	40	0	131
	a-Ga_2O_3/75 GSM paper	UV to visible	65 000/67 000	20.96	1.04×10^{10}	9.79	0	132
Schottky junction-	Pt-MoS_2	447–940	52 600 μs		2.09×10^{12}		0	133
based SPPD	$PtSe_2$/InP	940	4.35/5.66	0.718	4.37×10^{12}		0	134
	WSe_2	405, 808, 1064			6.35×10^{12}, 5.9×10^{11}, 1.4×10^9		0	135
Perovskite-based SPPD	Au-$Pb_2Nb_3O_{10}$-Ti	350	200/1200	2.8	1.1×10^{12}		0	136
	$(BDA_{0.7}(BA_2)_{0.3})$ $(EA)_2Pb_3Br_{10}$	360		>93	2.5×10^{15}	480	0	137
	PEA_2PbI_4			2.12				138

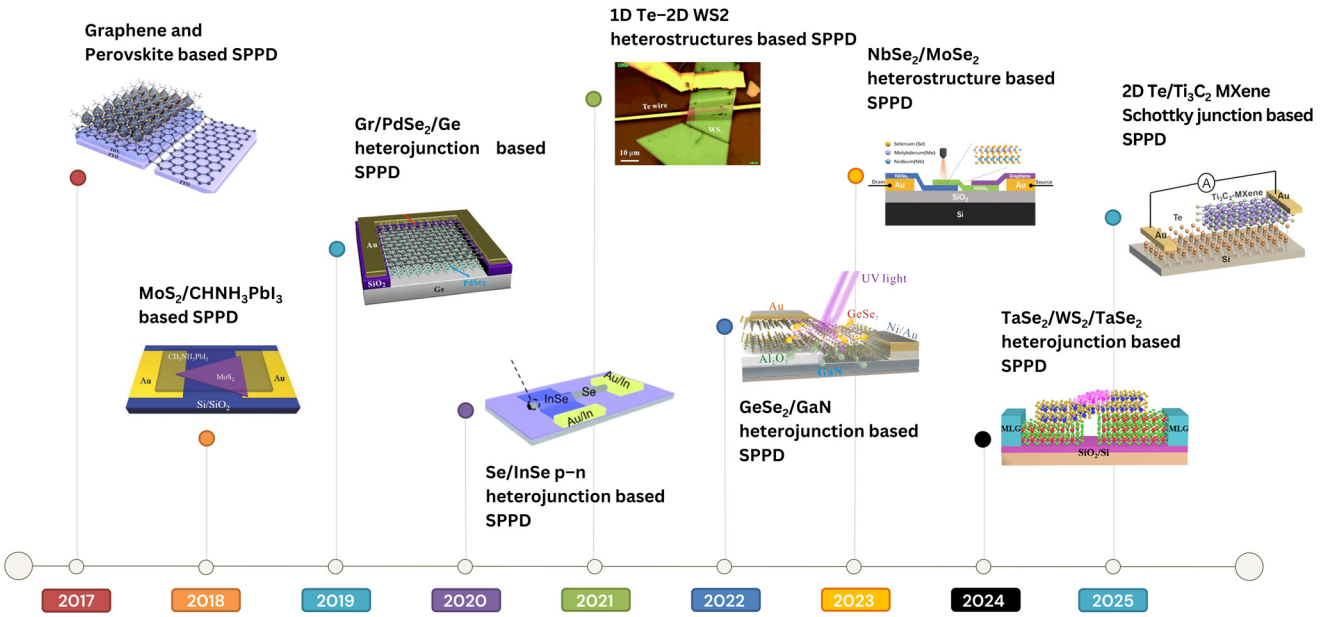

Fig. 1 Evolution of self-powered photodetectors. This figure has been reproduced from ref. 87–95 with permission from ACS Appl. Mater Interfaces, copyright 2017. Adv. Mater. Interfaces, copyright 2018. ACS Nano, copyright 2019. Nanoscale Horizons, copyright 2020. Nanoscale Advances, copyright 2021. Nano Energy, copyright 2022. Advanced Optical Materials, copyright 2023. Journal of Colloid and Interface Science, copyright 2024. Journal of Materials Chemistry C, copyright 2025.

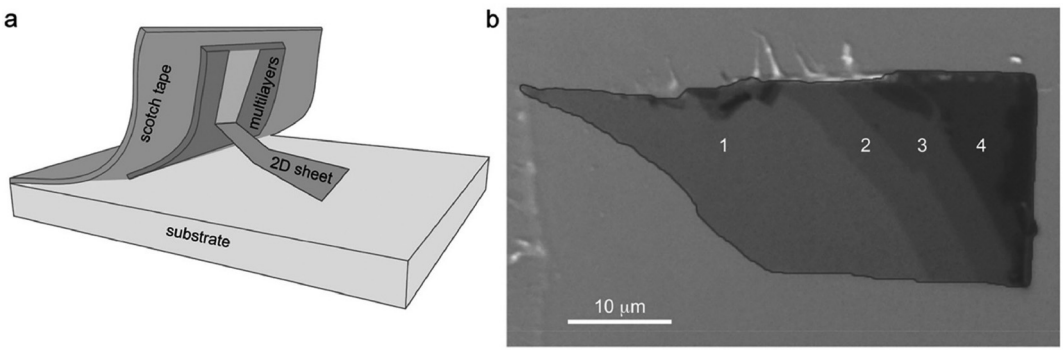

Fig. 2 (a) Schematic of the mechanical exfoliation process, where an adhesive substrate or tape applies a peeling force, causing the layered material to separate as sheets are detached during the peeling. (b) Optical image showing the exfoliated graphene, including both monolayer and multilayer regions, with the number of layers indicated numerically. This figure has been reproduced from ref. 139 with permission from the Journal of the Mechanics and Physics of Solids, copyright 2018.

their transfer onto substrates, commonly SiO_2/Si or PET, all conducted within controlled environments, as shown in Fig. 2. This technique provides exceptional material quality, few defects, and well-maintained electronic properties, making it perfect for fundamental research and proof-of-concept SPPDs.

4.2 Chemical vapor deposition (CVD)

CVD is extensively used for the scalable production of monolayer or few-layer TMDCs including MoS_2, WS_2, and Janus materials. This approach involves the vaporization of metal oxides (such as MoO_3 and WO_3) and chalcogen precursors (like Sulphur or selenium) at elevated temperatures, as shown in Fig. 3, leading to their reaction on substrates to produce uniform crystalline films. The use of CVD facilitates improved control over layer thickness, grain boundaries, and lateral dimensions, which is crucial for integrating SPPDs into broad or flexible platforms.

4.3 Solution processing and spin coating

Perovskite-based SPPDs typically depend on low-temperature solution processing because of the solubility of perovskite precursors in polar solvents such as DMF and DMSO. Thin films are produced through the process of spin-coating, which is subsequently followed by thermal annealing, as shown in Fig. 4, resulting in uniform and crystalline layers. This method facilitates the integration with adaptable substrates and

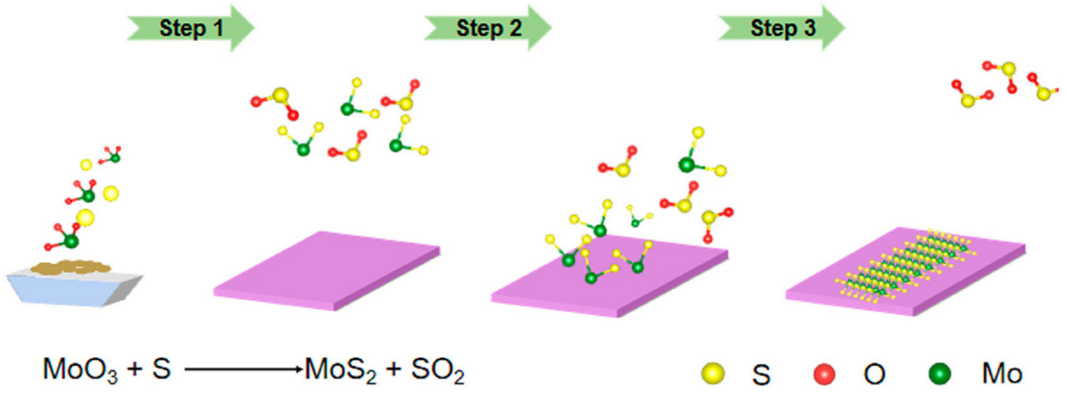

Fig. 3 CVD growth schematic for 2D materials. This figure has been reproduced from ref. 140 with permission from Chemistry of Materials, copyright 2020.

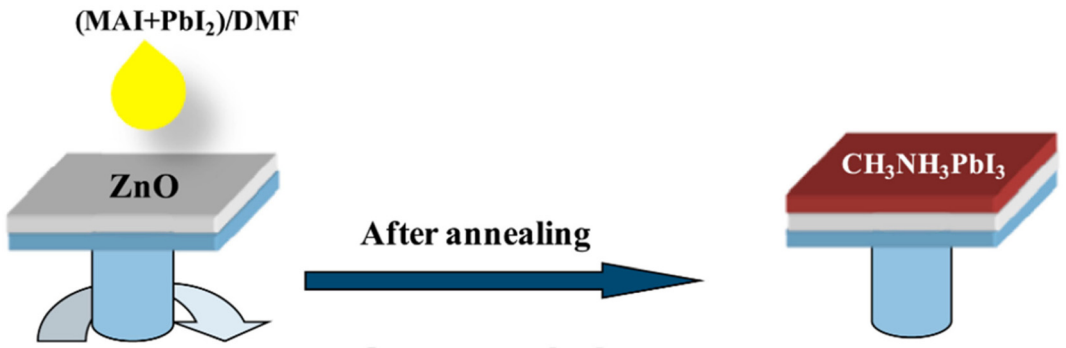

Fig. 4 Schematic of the one-step spin coating followed by thermal annealing. This figure has been reproduced from ref. 141 with permission from Materials Science in Semiconductor Processing, copyright 2020.

enables the formation of heterojunctions using TMDCs or metal oxides to enhance charge separation.

4.4 MXene synthesis and assembly

MXenes are generally produced through the selective etching of the "A" layer from MAX-phase precursors (for instance, Ti_3AlC_2) utilising hydrofluoric acid or LiF/HCl. This process yields 2D sheets containing terminal groups such as –F, –OH, and –O, as illustrated in the schematics in Fig. 5. The processing of these nanosheets involves techniques such as vacuum filtration, spray coating, or spin coating to create conductive films on semiconductors.

5. Performance metrics

Self-powered photodetectors (SPPDs) play a vital role in energy-efficient optoelectronics, providing numerous advantages, including the elimination of external power sources, reduced system size, and lower energy consumption. To evaluate the

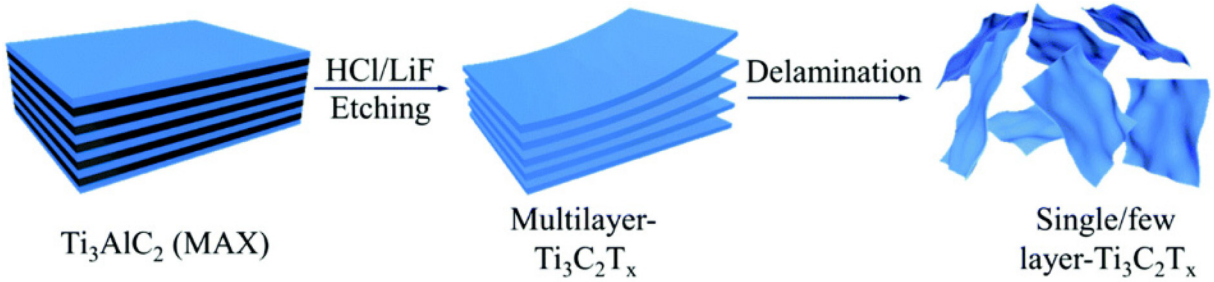

Fig. 5 Scheme of the fabrication procedure of MXenes. This figure has been reproduced from ref. 142 with permission from the Journal of Materials Chemistry C, copyright 2019.

effectiveness of these devices, several key performance metrics are used. These include responsivity, detectivity, rise and fall times, and quantum efficiency (QE), which are critical for understanding their capabilities in various applications such as optical communication, wearable electronics, and environmental monitoring.[143]

Recent advancements in materials science have enabled significant improvements in these metrics, particularly through the use of 2D materials, which have enhanced the overall performance of SPPDs.[144] The importance of each of these parameters becomes evident as we examine their individual contributions to the device's functionality and efficiency. By focusing on improving these performance metrics, researchers are working towards the development of next-generation SPPDs that can meet the demands of modern optoelectronic systems. As the field progresses, innovations in material selection, fabrication methods, and device architectures continue to push the boundaries of what is achievable.[145]

5.1 Responsivity

Responsivity (R) is a key metric used to evaluate how efficiently a photodetector converts optical power into electrical current. It measures the photocurrent generated per unit of incident light power over time in the active area of the photodetector. The formula for responsivity is given as follows:

$$R = \frac{I_{\text{light}} - I_{\text{dark}}}{P_{\text{light}} \cdot S}$$

where I_{light} represents the current generated by the light, I_{dark} is the current in the absence of light, P_{light} is the light intensity, and S is the area exposed to light. Responsivity is crucial for understanding how effectively a device converts light into electrical signals, and its units are typically WA^{-1}.[146]

R is typically dependent on the optical power intensity (P). At low power levels, self-powered photodetectors such as those based on MoS_2 or WSe_2 exhibit high responsivity due to efficient photon absorption and minimal recombination losses. As the optical power increases, the photocurrent generated by the photodetector increases as well. However, at higher optical powers, the responsivity decreases due to saturation effects and charge recombination. This is because, at higher illumination intensities, the minority carriers may recombine before contributing to the photocurrent, thereby reducing the photodetector's efficiency.

For example, a MoS_2-based photodetector may exhibit high responsivity at lower power densities (*e.g.*, around 431 mA W^{-1} at 38 mW cm^{-2}) but experience a reduction in responsivity as the optical power density increases beyond certain thresholds.[147] This non-linear relationship is crucial for understanding the limitations of photodetector performance in real-world applications where light intensity may vary. Therefore, optimizing the optical power range in which the photodetector operates is essential for maximizing performance, especially in low-power sensing applications.

5.2 Detectivity (D^*)

Detectivity (D^*) measures the ability of a photodetector to detect weak light signals. It is influenced by both the responsivity and the amount of noise in the system. Detectivity is defined as follows:

$$D^* = \frac{S}{(I_{\text{noise}}\Delta f)^{1/2}}$$

where S is the detector's effective area, I_{noise} is the total noise current, and Δf is the electrical bandwidth. A higher D^* value indicates a better ability to detect low-light signals. When dark current dominates, D^* is given as follows:

$$D^* = \frac{S \cdot R}{(\sqrt{2qI_{\text{dark}}})}$$

This formula highlights that D^* is directly related to responsivity and inversely related to dark current, making it essential to minimize the dark current for detecting weak light.[143]

5.3 External quantum efficiency (EQE)

The External Quantum Efficiency (EQE) quantifies the proportion of incident photons that are converted into charge carriers by the photodetector. This metric reflects how effectively the device uses incoming light to generate electrical output. Due to material limitations like recombination within the perovskite layer, not all incident photons contribute to the photocurrent. EQE is expressed as follows:

$$\text{EQE} = \frac{I_{\text{light}}}{Phv}$$

where e is the fundamental charge, h is Planck's constant, and ν represents the frequency of the light. The EQE values range from 0% to 100%, with some detectors exceeding 100% due to gain, which amplifies the current relative to the incident light intensity.[146]

5.4 Response time

The response time of a photodetector is the time it takes to react to changes in light intensity, which is essential for high-speed applications such as optical communication. The response time is characterized by the rise time (τ_r) and fall time (τ_f), which are defined by the time it takes for the photocurrent to change from 10% to 90% (rise) or from 90% to 10% (fall) of its maximum value. Shorter rise and fall times indicate a faster response, which is crucial for detecting rapidly changing light signals.[148]

Materials such as MoS_2 and WSe_2 with their direct band gaps in monolayer form exhibit fast charge transport, contributing to shorter rise and fall times. The direct bandgap enables efficient exciton generation and rapid carrier separation, resulting in low response times. For example, monolayer MoS_2 demonstrates rise and fall times in the millisecond range,[149] making it suitable for high-speed sensing and wearable devices. The performance of these devices is further enhanced by asymmetric Schottky junctions or van der Waals

(vdW) interfaces, which minimize recombination losses and facilitate faster charge separation and transport, ultimately leading to low rise and fall times.

6. Transferring techniques

The integration of two-dimensional (2D) materials onto substrates is a crucial step in fabricating self-powered photodetectors (SPPDs). The transfer process directly affects the performance, scalability, and functionality of the final device. Given the fragile nature of 2D materials and the precision required for their placement, the choice of transfer method is paramount to achieving high-quality and reproducible devices. Several techniques have been developed to transfer these delicate materials, each offering unique advantages while also posing certain challenges that need to be addressed.

The methods for transferring 2D materials can be generally divided into two categories: dry transfer and wet transfer. Dry transfer techniques typically involve the use of solid materials, such as polymers or adhesive tapes, to pick up and transfer the 2D material from its growth substrate to the target substrate. These methods are often favored for their simplicity and ability to handle fragile materials without the use of solvents or liquids. However, issues such as contamination and alignment still need to be managed.

However, wet transfer methods rely on liquids or chemical solutions to facilitate the transfer, often reducing contamination and potential damage to the 2D material. While these methods can offer superior material quality and scalability, they are often more complex and require careful handling to ensure material integrity.

6.1 Dry transfer methods

Dry transfer methods utilize solid materials such as polymers, adhesive tapes, or metal foils to transfer 2D material flakes onto target substrates. The techniques in Table 3 are relatively simple and do not require the use of solvents, making them ideal for transferring delicate 2D materials without compromising their properties. However, challenges such as uniformity, adhesion, and contamination still exist.

6.2 Wet transfer methods

Wet transfer methods involve the use of liquids or chemical solutions to facilitate the transfer of 2D materials onto substrates. These techniques offer distinct advantages, especially in terms of reducing contamination and minimizing damage to the delicate 2D material during the transfer process. Wet transfer can be particularly useful for transferring materials that are highly sensitive to physical handling or mechanical stress, as it mitigates the need for direct physical contact between the 2D material and the target substrate. Additionally, the wet transfer methods can provide better adhesion and uniformity than the dry transfer methods, which is essential for ensuring the consistency and performance of the final device.

While wet transfer methods are capable of producing high-quality 2D materials with minimal defects, they suffer from challenges such as the need for precise control over the solution's chemical composition, temperature, and pressure. The risk of material contamination or degradation also increases if these factors are not carefully managed. Nonetheless, wet transfer techniques have seen significant advancements in recent years, and their versatility makes them a valuable option for large-area and high-throughput production of 2D material-based devices. The primary wet transfer techniques commonly employed for transferring 2D materials are shown in Table 4.

7. Single TMDC-based SPPDs

TMDCs are layered materials with outstanding structural, electronic, and optical features. They are widely used in optoelectronics and photovoltaic systems, *e.g.*, SPPDs.[19,151] MoS_2 and WSe_2 represent the most studied TMDCs due to their remarkable characteristics.[133]

A fundamental characteristic of TMDCs is that they are affected by electronic property changes through several layers and external conditions, such as applied strain, electric field,

Table 3 Dry transfer techniques

Method	Description
PDMS-assisted transfer	A thin PDMS film is applied to the 2D material, which is then peeled off and transferred to the target substrate. This method is widely used due to its simplicity and effectiveness.
PC-assisted transfer	A polycarbonate film is used to pick up the 2D material from its growth substrate, which is then transferred to the target substrate. This method is advantageous for transferring materials onto flexible substrates.
Polymer-assisted transfer	Involves using a polymer layer to facilitate the transfer of 2D materials onto substrates. This method can be combined with other techniques to improve transfer efficiency.
Transfer *via* adhesive tapes	Utilizes adhesive tapes to lift 2D materials from their growth substrates and transfer them to target substrates. This method is simple but may introduce contamination.
Transfer *via* LCP films	LCP films are used to pick up and transfer 2D materials onto substrates. This method is particularly useful for transferring materials onto curved or flexible substrates.
Transfer *via* metal foils	Metal foils are used as carriers to transfer 2D materials onto substrates. This method is suitable for large-area transfer but may require additional steps to remove the metal foil.
Transfer *via* GO films	GO films are used to pick up and transfer 2D materials onto substrates. This method can be advantageous due to the strong interaction between GO and 2D materials.[150]

Table 4 Wet transfer techniques

Method	Description
Water-assisted transfer	Utilizes water to facilitate the transfer of 2D materials onto substrates. This method helps reduce contamination and damage to the material.
Chemical-assisted transfer	Involves the use of chemical solutions that assist in the transfer of 2D materials. This method can be customized for different material types and substrates.
Thermal-assisted transfer	Applies heat to the substrate and material to aid in the transfer process. This method can enhance adhesion, but it requires precise temperature control to prevent damage.
Electrostatic-assisted transfer	Uses electrostatic forces to transfer 2D materials onto substrates, often employed for aligning materials with high precision. However, it requires specialized equipment.
Capillary force-assisted transfer	Utilizes capillary forces to transfer 2D materials, beneficial for substrates with complex or irregular topographies, allowing for more uniform material deposition.[150]

or chemical doping, which alter their structure. MoS_2 and WSe_2 are semiconductors with direct band gaps of approximately 1.8 eV and 1.7 eV, respectively, in their monolayer form.[152] The designed assembly can effectively absorb and emit light, and this direct bandgap is useful for optoelectronic applications. However, the increasing layers alter the direct and indirect band gaps of these materials, and this change in band gap may also affect their performance. Furthermore, the charge carrier mobility of TMDCs depends upon the material and thickness of layers.[153] For example, monolayer MoS_2 has an electron mobility of up to 200 $cm^2 V^{-1} s^{-1}$, while WSe_2 exhibits comparable or even higher mobility.[154,155] These are essential properties for high-speed electronic devices and efficient photodetectors.

Moreover, the optical characteristics of TMDC are essential for utilizing the SPPDs. Strong photoluminescence is also observed in WSe_2 and MoS_2, consistent with their direct band gap nature.[156] They are promising candidate materials for photodetector applications, as they can efficiently absorb visible and near-infrared light. However, they can also supply a strong photocurrent in the presence of light and can be employed in self-powered systems. The optical response of TMDCs is as nonlinear as their excitons; therefore, the optical response of TMDCs in this respect is increased. Such tightly bound excitons are also observed, particularly in MoS_2 and WSe_2, which have been shown to provide tightly bound excitons and affect their photonic applications. The excitons in these materials have a binding energy of a few hundred millielectronvolts and a strong response to optical excitation.[157,158] In the work by Tang *et al.*,[159] a high-performance, flexible MoS_2-based SPPD was fabricated using a simple Au electrode configuration on a polyethylene terephthalate (PET) substrate, resulting in high responsivity and a fast response time.[159] Unlike conventional designs with heterojunctions or asymmetric metal contacts, the self-powered operation of this device stems from asymmetric Schottky barriers at the MoS_2/Au interfaces, resulting from the vdW gap difference between the two interfaces. Fig. 6(a) shows the optical image of the fabricated device with the MoS_2 flake on two Au electrodes, which are marked by two white arrows on the PET substrate. The PET substrate is flexible, which is favorable for wearable applications, as shown in Fig. 6(b). In Fig. 6(c) above, the *I–V* curves of the device under different illumination intensities (38 mW cm^{-2}, 96 mW cm^{-2}, and 439 mW cm^{-2}) are compared to the dark condition, illustrating that the electrical characteristics vary under different illumination intensities. Their nonlinear and asymmetric nature confirms the existence of the Schottky barriers at the MoS_2/Au junctions, which is essential for self-power operation. There is an increase in photocurrent at zero bias under illumination, indicating the high sensitivity of the device and its ability to operate without any external power source. Fig. 6(c) inset shows the magnified view of the low-voltage region for which a discernible photocurrent is applied at a minimal bias.

Fig. 6(d) shows the transient photoresponse of the MoS_2 photodetector under switched 450 nm lights with different power densities at 0 V. The photodetector could detect 450 nm light continuously at 0 V, indicating that it had excellent application prospects for future self-powered photodetectors. Upon illumination by 450 nm light with a power density of 439 mW cm^{-2}, the photocurrent of the photodetector is around 20 nA, two orders of magnitude higher than that of the dark current. At irradiation frequencies of 450 nm and 38 mW cm^{-2}, the photocurrent, responsivity, EQE, and detectivity of the photodetector at 0 V are up to 5 nA, 431 mA W^{-1}, 119% and 2.54×10^8 Jones, illustrating the consistency and stability of the device under exposure to periodical light with different intensities. The current remains stable in the dark and exhibits a steep rise and fall upon illumination, indicating a significant response and recovery time. The robust and repeatable switching behavior demonstrates that the asymmetric vdW gaps function as a built-in electric field to facilitate carrier transport.

The variation in responsivity with respect to the light power density at 0 V bias is shown in Fig. 6(e). In comparison, the curve represents the variation in detectivity with respect to light power density at 0 V bias. The saturation of trap states results in decreased responsivity with increased power density, which encourages charge recombination at higher illumination levels. However, the minority carrier concentration is still sufficiently high to ensure high detectivity, making the device even more suitable for low-power detection. The response speed depicted in Fig. 6(f) shows an ultra-fast response and recovery time of 40 ms, proving the photodetector's ability to work with high-speed optical signal detection. Moreover, the change in photocurrent without considerable delay confirms

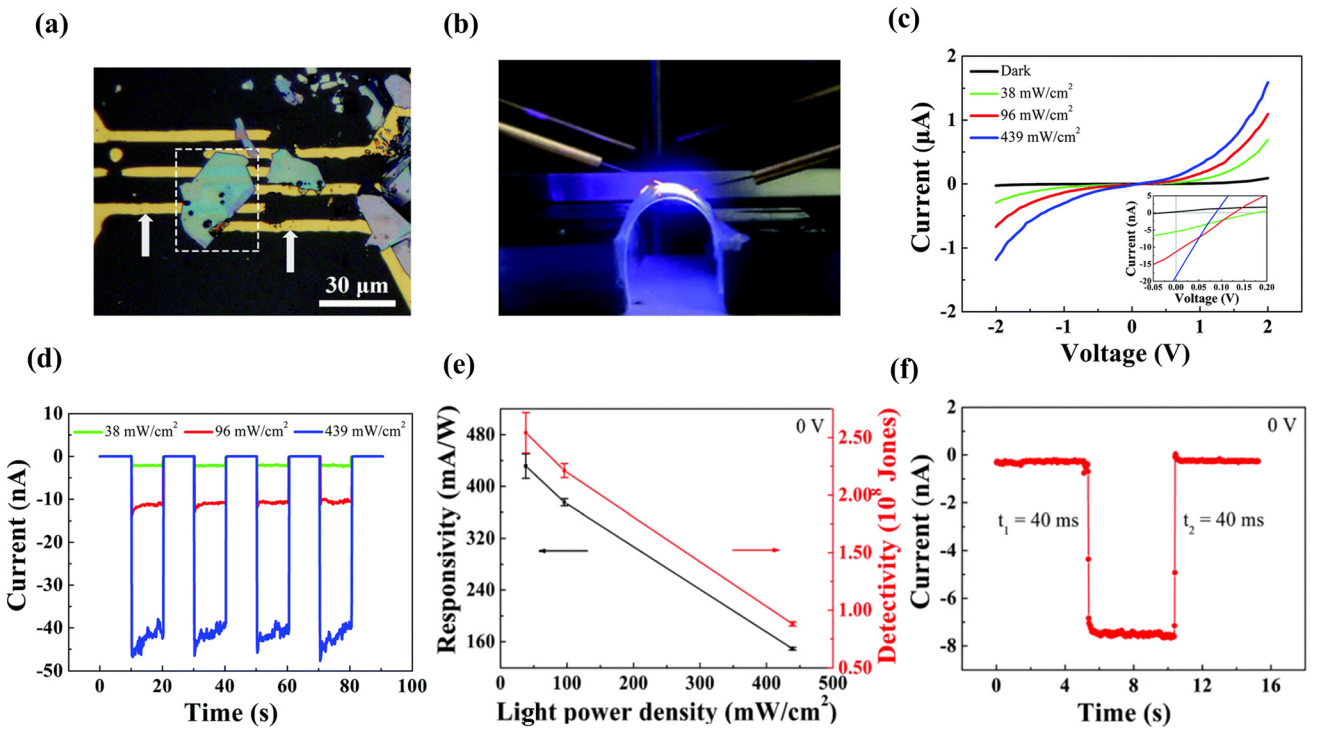

Fig. 6 (a) OM image of the MoS_2 photodetector. Two Au electrodes, marked by the left and right white arrows, are probed with a source meter to study the performance of this photodetector. (b) Photograph of the flexible self-powered MoS2 photodetector at a bending state. (c) *I*–*V* curves of the MoS_2 photodetector in dark and under the illumination of a 450 nm light with different power densities. The inset shows a partial magnification of the *I*–*V* curves. (d) Time-resolved current responses of the MoS_2 photodetector measured with different power density values at 0 V. (e) Responsivity and detectivity at different light power densities. (f) Response time and recovery time of the MoS_2 photodetector under a 450 nm light. This figure has been reproduced from ref. 147 with permission from Physical Chemistry Chemical Physics, copyright 2022.

the high-quality interface and efficient charge transport in the MoS2-based photodetector. This asymmetry induces a built-in electric field across the device, enabling efficient charge separation and transport without the need for an external bias, which is crucial for self-powered operation. Additionally, the direct bandgap and strong light absorption of monolayer MoS_2 enhance exciton generation and photocurrent, while the high-quality interface reduces recombination, resulting in fast, stable, and sensitive photoresponses. The MoS_2-based photodetector operates through asymmetric Schottky junctions, which create a built-in electric field that facilitates the separation and transport of photoexcited charge carriers without the need for an external bias. The direct bandgap of MoS_2 enhances exciton generation and light absorption, enabling efficient photocurrent generation. The two-dimensional nature of MoS_2 allows for fast charge transport and high responsivity, making the device ideal for self-powered and low-power applications. The combination of these mechanisms ensures a fast, stable, and energy-efficient photodetector suitable for next-generation optoelectronic and wearable devices.

Unlike typical bulk materials, WSe_2 is a material that undergoes a direct-to-indirect bandgap transition as its thickness increases, which affects its absorption spectra.[160] This property places WSe_2 in an excellent position for photodetectors and, above all, self-powered devices that operate without an applied bias voltage.[161] The differences in work functions at the WSe_2-metal interface and the asymmetrical contact structure are key to producing an intrinsic electric field, which assists in efficient charge separation and transfer. C. J. Zhou *et al.*[161] prepared a WSe_2-based metal–semiconductor-metal (MSM) photodetector with asymmetric contacts, as shown in Fig. 7(a). The optical microscope picture clearly shows the WSe_2 flake placed between two metal electrodes of different contact lengths, which is the principle for achieving self-driven operation. The schematics of the device can be seen in Fig. 7(b). This asymmetry results in different Schottky barrier heights at the two metal–semiconductor interfaces, enabling charge separation under illumination without the need for an external bias. The visible color contrast of the WSe_2 flake indicates that it is a multilayer, which leads to the formation of an indirect bandgap, and it facilitates efficient photogeneration of carriers.

The transfer curve of the device was measured over a gate voltage range of −60 to 60 V to understand its behavior, as shown in Fig. 7(c). The WSe_2-based MSM photodetector shows n-type prefer ambipolar transport characteristics with an electron mobility of 26.3 $cm^2\ V^{-1}\ s^{-1}$, much higher than the hole mobility of 7.4 $cm^2\ V^{-1}\ s^{-1}$. The on/off ratio of the n-type side is 5.82×10^4, while that of the p-type side is 4.87×10^3, indicating more substantial electron conduction. The $\log I_{ds}$ curve

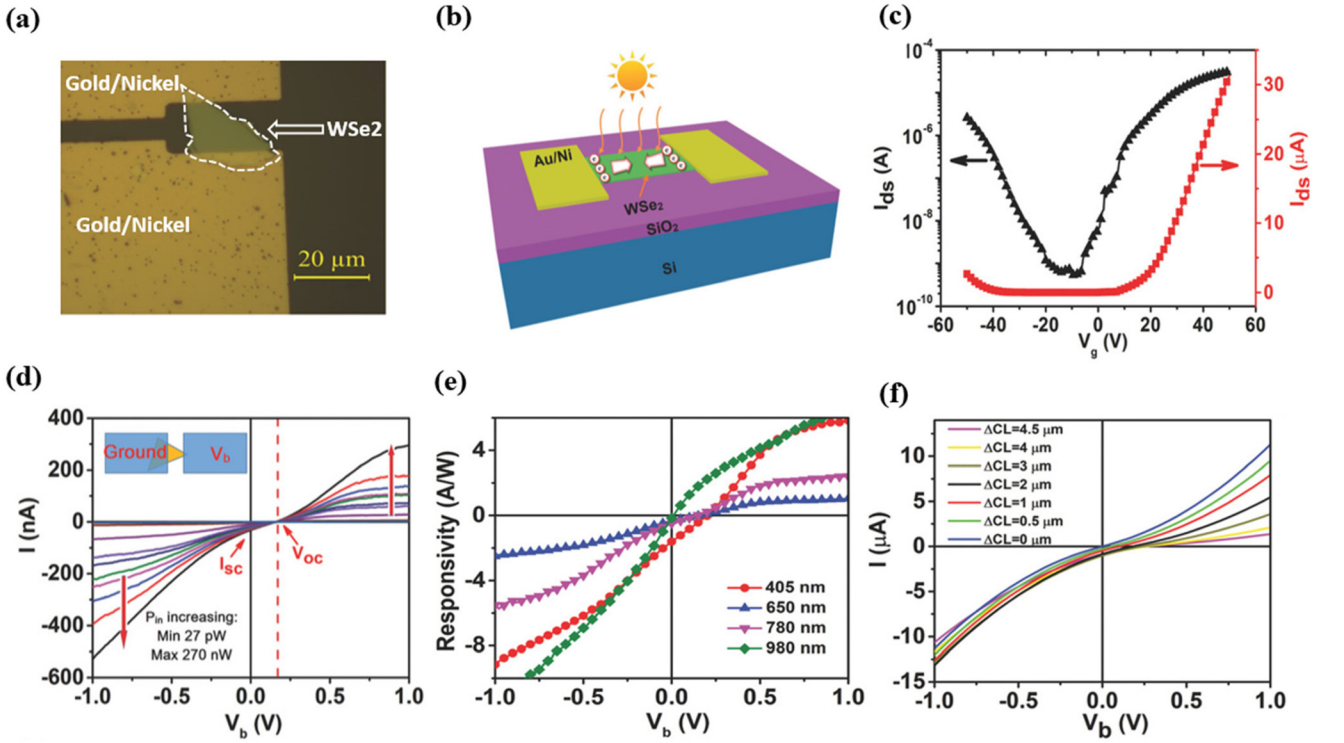

Fig. 7 Schematic device structure of metal-WSe_2-metal (MSM) photodetectors: (a) Optical image of the fabricated MSM device with asymmetric interface architectures. (b) Schematic of the device. (c) Transfer curve of the fabricated WSe_2 device. (d) *I*–*V* curves of the MSM photodetector for different input powers of 27 pW to 270 nW. The light wavelength is 650 nm. The inset depicts the measurement arrangement. (e) Calculated responsivity of the MSM photodetector. (f) *I*–*V* curves of the asymmetric MSM photodetector with different contact lengths. The contact surface between 0.5 and 5 μm is the smallest among two contact lengths. This figure has been reproduced from ref. 163 with permission from Advanced Functional Materials, copyright 2018.

indicates the presence of a Schottky barrier at the metal-WSe2 interface; charge injection is suppressed at lower gate voltages, while at higher gate voltages, carrier accumulation increases conduction.[162] The self-driven photodetection operation is schematically illustrated in Fig. 7(d), where the current–voltage (*I*–*V*) characteristics of the MSM photodetector are shown under illumination. The device was tested at 650 nm from a light-emitting diode (LED) source with a full power density of 5.41 mW mm^{-2}, meaning a total incident power of 270 nW. A non-zero short-circuit current (I_{sc}) of −31.1 nA and an open-circuit voltage (V_{oc}) of 0.16 V are observed at zero bias due to the internal electric field induced by the contact length, enabling self-powered operation. Rising illumination power (from 27 pW to 270 nW) results in the exact scaling of photocurrent, which validates the device's high sensitivity. The nonlinear *I*–*V* behavior implies that the carrier transport is due to a combined effect of photogenerated carriers and Schottky barrier modulation. This photovoltaic effect, which has been observed in one-sided Schottky junctions or PN junctions, is related here to the asymmetry of the electrodes, contrary to what occurs in symmetric MSM photodetectors, where I_{sc} and V_{oc} are equal to 0 under similar conditions.

The device efficiency is demonstrated in Fig. 7(e), showing the responsivity at different wavelengths and bias voltages. The highest responsivity of 11.2 A W^{-1} is obtained at a bias of −1 V under low illumination, and a responsivity greater than 2 AW^{-1} is independently observed at the same bias for all wavelengths tested (405 nm, 650 nm, 780 nm, and 980 nm). The device still possesses appreciable responsivity at the zero bias, reaching 1.62 A W^{-1} at 405 nm, indicating high light absorption and efficient carrier separation. The increased responsivity under a negative bias suggests that the direction of the built-in electric field assists in charge transport, enhancing photodetection performance. Fig. 7(f) plots the influence of contact length asymmetry (ΔCL) on the *I*–*V* characteristics of the device. The various curves represent devices with increasing asymmetries (ΔCL = 0 to 4.5 μm) where one contact length is changed and the other is fixed at 5 μm. As the ΔCL increases, varying from −0.6 pA to approximately −1 μA, it is evident that a more pronounced contact asymmetry generates a stronger built-in electric field, enabling stronger photocurrents. This indicates that contact geometry substantially influences the self-powered performance of WSe_2-based MSM photodetectors. By incorporating asymmetric contact geometries, the proposed MSM WSe_2 photodetector can realize self-driven, bias-free operation. The device exhibits high responsivity (2.31 A W^{-1} at 0 V), ultra-low dark current (~1 fA), and excellent detectivity (9.16×10^{11} Jones). This behavior is primarily attributed to the asymmetric contact lengths, which induce different Schottky barrier heights at the metal–WSe_2

interfaces, generating a built-in electric field that effectively drives charge separation. The multilayer structure of WSe_2, which transitions from a direct to an indirect bandgap as the layers increase, enables improved light absorption and more efficient carrier generation. The varying contact lengths at the electrodes enhance this electric field, thereby improving charge transport and expanding the device's sensitivity. This setup enables the photodetector to operate self-powered, with efficient charge separation and a quick response to light. The deliberate contact geometry further strengthens the internal field, contributing to the device's high responsivity and reliable self-powered operation.

7.1 Graphenes and TMDC heterostructures

vdW heterostructures, which consist of vertically stacking 2D materials, have been exploited to create photodetectors. These heterostructures combine the unique electronic and optical properties of their single components to fully optimise charge separation and broaden responsivity.[164,165] With the exceptional electrical conductivity, high carrier mobility, and broadband optical absorption, graphene is an ideal transparent conductive electrode in these heterostructures.[125,166,167]

A heterostructure of graphene with TMDCs develops a built-in electric field at their junction, allowing efficient charge transfer and self-powered operation. The WS_2-based heterojunctions exhibit enhanced optoelectronic functionality by strongly coupling light with matter, while offering flexible options for doping n- or p-type materials. The heterojunction shown in Fig. 8(a) utilizes graphene/WS_2/$LaVO_3$ to create self-powered, high-speed, broadband photodetection devices for various photodetection applications. The incorporation of $LaVO_3$ perovskite structures with graphene/TMDC heterostructures facilitates better photocarrier generation and separation.[168–170] Triethylenetetramine (TETA) doped graphene with a transparent conductive electrode (TCE) that combined high conductance capability with visible light transmission through its TETA doping process. Such geometric arrangements of different materials within heterojunctions increased the responsivity, detectivity, and operational efficiency.[170,171]

The TETA-Gr/WS_2/$LaVO_3$ nanoparticle heterojunction exhibits its optoelectronic characteristics through the measurements in Fig. 8(b), as shown in the current density–voltage (*J*–*V*) characteristics. The built-in potential at the WS_2/$LaVO_3$ interface is crucial for carrier separation, as it enables rectifying behavior. The device produces a distinctive photocurrent under illumination at 600 μW cm^{-2} using 600 nm light due to its effective light absorption and charge transport behavior. The maximum photocurrent response was observed at a $LaVO_3$ thickness of 200 nm, since this value represents an optimal balance between the device optical absorption and charge

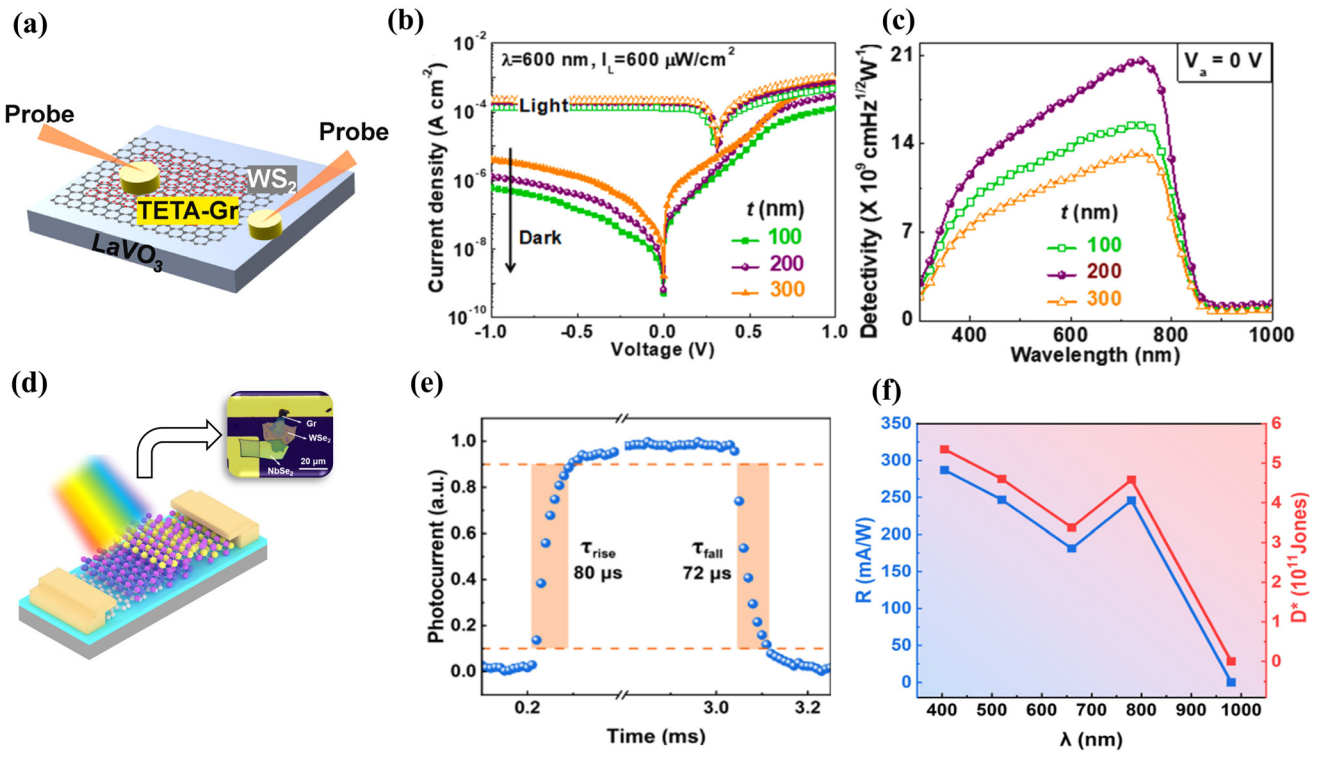

Fig. 8 (a) Schematic device structure. (b) *J*–*V* behaviors of TETA-Gr/WS_2/$LaVO_3$ PD as a function of thickness (t) under darkness and illumination. (c) Detectivity (*D**) evaluation performed on different *t*-dependent PD structures under zero-bias conditions. (d) Schematic structure of the device. (e) Photoresponse speed of the Gr/WSe_2/$NbSe_2$ vdWH photodetector at V_{ds} = 0 V. (f) Wavelength dependence of *R* and *D**. This figure has been reproduced from ref. 105 and 106 with permission from the Journal of Materials Science & Technology, copyright 2025. Current Applied Physics, copyright 2025.

transport abilities. The photocurrent reaches saturation levels for device thicknesses beyond 200 nm because transfer resistance and recombination losses increase. The efficiency improvement of self-powered broadband photodetectors depends on optimising heterojunction structures and material thicknesses when using 2D/3D material interfaces. The TETA-Gr/WS_2/$LaVO_3$ heterojunction exhibits the detectivity (D^*) spectrum, which is shown in Fig. 8(c) as the $LaVO_3$ thickness varies. The designed device exhibits detectivity capabilities spanning from 300 nm to 850 nm wavelengths, with a peak sensitivity of 2.1×10^{10} Jones at a $LaVO_3$ thickness of 200 nm. The device achieves maximum light absorption efficiency at this specific thickness and preserves efficient charge transfer to minimise recombination losses. The detectivity reaches a long-term balance when measuring beyond 200 nm due to resistance issues that prevent further improvement in photocurrent generation. The crucial effects of controlling the thickness emerge as essential factors to maximise photodetector operational performance.

Research on this heterojunction emphasizes how interface development, combined with material modification, enables the fabrication of self-powered broadband photodetectors. The built-in electric field at the WS_2/$LaVO_3$ interface facilitates efficient carrier separation, eliminating the need for external power, while TETA-doped graphene enhances conductivity and light transmission. Optimizing the $LaVO_3$ thickness allows maximum light absorption and efficient charge transport, reducing recombination losses. The graphene/TMDC/$LaVO_3$ heterojunction operates through a built-in electric field at the interface between WS_2 and graphene, enabling efficient charge separation and self-powered operation. The inclusion of the $LaVO_3$ perovskite enhances photocurrent generation and charge transport, while TETA-doped graphene improves conductivity and light transmission. The optimal $LaVO_3$ thickness of 200 nm strikes a balance between light absorption and charge transport, thereby minimizing recombination losses and maximizing detectivity. This structural optimization allows the device to efficiently detect wavelengths from 300 nm to 850 nm, making it ideal for high-speed, energy-efficient photodetection in emerging optoelectronic applications.

Li *et al.*[93] demonstrated that integrating $NbSe_2$ with TMDCs significantly enhances charge transport and photodetection efficiency in SPPDs. $NbSe_2$ is a suitable contact material for various applications due to its superconducting properties and high work function (~5.52 eV).[172] These heterostructures, made with WSe_2 and MoS_2, along with $NbSe_2$, create effective carrier separation channels due to the electric fields that develop across their junction region.[173] Band structure engineering in $NbSe_2$ produces contact surfaces free of dangling bonds, while preventing Fermi-level pinning and enhancing charge injection and extraction due to its flattened interface. He *et al.*[105] demonstrated an SPPD offering low power consumption and high integration density. The photodetector built with Gr/WSe_2/$NbSe_2$ heterojunctions is shown in Fig. 8(d). The device includes Gr electrodes and $NbSe_2$ electrodes, with WSe_2 as the channel between them. A difference in Schottky barrier heights occurs when asymmetric material contacts form at the interfaces between Gr/WSe_2 and $NbSe_2$/WSe_2, resulting in the generation of a built-in electric field.

A time-based assessment of the Gr/WSe_2/$NbSe_2$ heterojunction photoresponse of the photodetector occurs at zero bias while illuminating 405 nm light, according to Fig. 8(e). The ultrafast photoresponse speed of this device occurs over 80 μs for the rise time and 72 μs for the decay time. The photodetection characteristics of the Gr/WSe_2/$NbSe_2$ photodetector are displayed in Fig. 8(f), according to the wavelength. The device shows a variation in R and D^* values throughout wavelength measurements from 405 nm to 980 nm. The collected data demonstrates the excellent photodetection functionality of the device throughout a wide wavelength range, with deteriorating performance observed at higher wavelengths. This normal phenomenon occurs in photodetectors because extended wavelengths reduce the absorption capabilities of the detector. The heterostructure excels due to asymmetric contacts, which create a built-in electric field for efficient charge separation without the need for an external bias. $NbSe_2$ provides a clean, low-resistance interface that improves charge transport. Ultrafast response and broad spectral sensitivity, with a peak at 708 nm, set it apart from typical TMDC photodetectors. This combination of speed, wide wavelength range, and high-quality contacts makes it ideal for advanced low-power, high-speed optoelectronic applications.

8. MXene-based self-powered photodetectors

MXenes demonstrate remarkable appeal as 2D materials due to their combination of electrically conductive properties with strong structural integrity and adjustable surface characteristics, which enable their use in various optoelectronic systems, especially SPPDs.[174,175] The manufacture of MXenes involves an etching process that removes "A" elements from MAX phases to produce material structures with functional surface attachments, including –OH, –F, and –O groups that enable interface tuning and surface modification.[176] Mxene significantly improves the performance of photodetectors because these materials offer efficient carrier transport properties alongside UV spectrum transparency and high conductivity in SPPDs.[177–179] Furthermore, MXenes function as transparent electrodes and form van der Waals (vdW) heterojunctions with semiconductors like GaN, thereby enhancing the device photocurrent and responsivity.[120,180] Yu Ding *et al.*[181] demonstrated the production of MXene/GaN van der Waals Schottky UV photodetectors, as shown in Fig. 9(a). A built-in electric field is generated when an MXene ($Ti_3C_2T_x$) film contacts GaN to form a Schottky junction, facilitating the separation of photogenerated electron–hole pairs. This device controls the flow of electricity through asymmetric electrodes that combine MXene with fundamental Ti/Al/Ni/Au alloy contacts, thereby achieving self-powered functionality. The MXene–GaN Schottky contact enables photocurrent generation from an

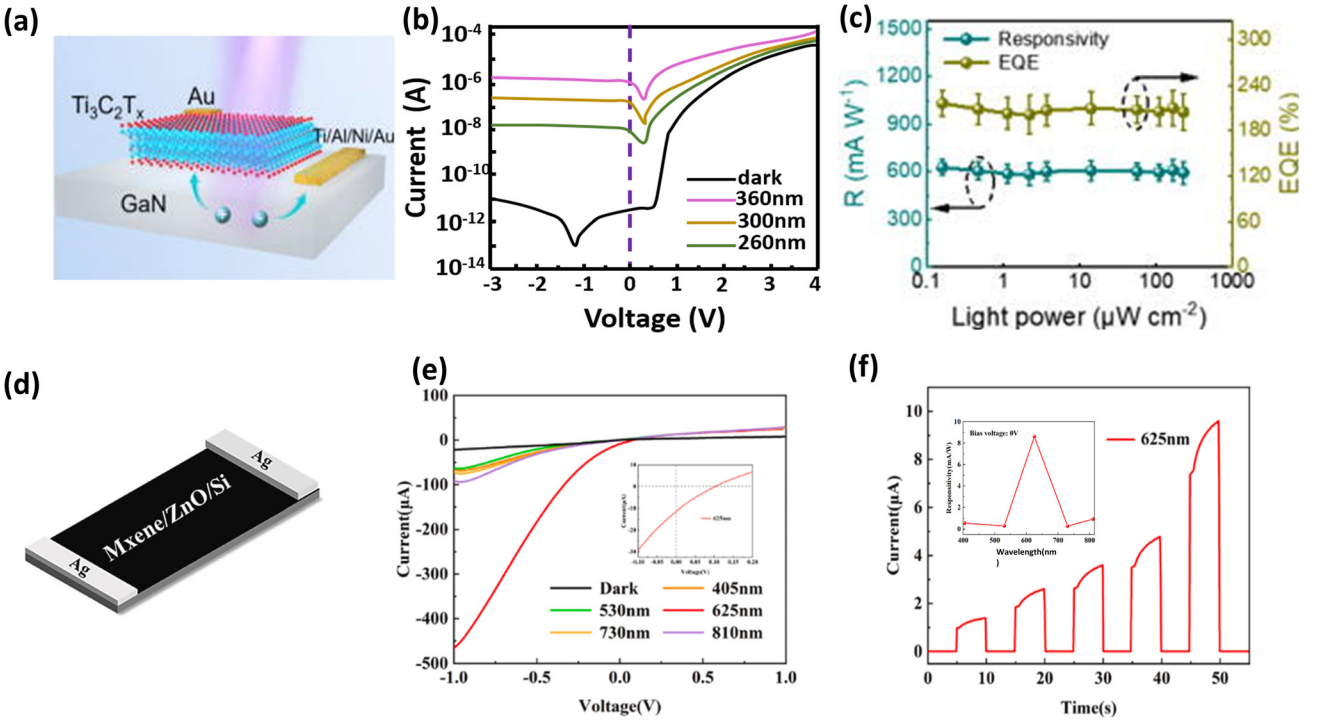

Fig. 9 Device design and material characterization: (a) structural diagram of MXene/GaN vdW UV photodetector. (b) *I*–*V* transfer curves of the MXene/GaN photodetector operating on a logarithmic scale under dark conditions and illumination at 260, 300, and 360 nm. The three applied UV lights have the powers of 0.08 μW, 0.28 μW, and 1.08 μW. (c) Responsivity and EQE of the self-powered mode at different light power densities. The figure contains five detector devices whose average values represent each point. (d) Schematic of the MXene/ZnO/Si device. (e) *I*–*V* curves of the MXene/ZnO/Si device under light at different wavelengths. (f) Corresponding *I*–*t* curves at 625 nm. The inset represents the response time plot of the MXene/ZnO/Si device. This figure has been reproduced from ref. 182 and 183 with permission from Ceramics International, copyright 2024. Applied Physics Reviews, copyright 2025.

intrinsic electric field at the junction, eliminating the need for an external bias voltage, and thereby, achieving high efficiency in detecting UV photons.

The *I*–*V* curve exhibits asymmetric rectification patterns, demonstrating Schottky junction behavior at the MXene and GaN interface, as shown in Fig. 9(b). At 0 V bias, the photodetector produced substantial light-induced currents, which are 7.5 nA, 108.9 nA, and 808.9 nA under 260 nm, 300 nm, and 360 nm UV illumination, respectively, demonstrating robust photoactivity. The recorded photocurrents (I_{light}) exceed all dark current values (I_{dark} = 3.7 pA) by multiple orders of magnitude. The photo-to-dark current ratio (I_{light}/I_{dark}) achieved approximately 2.4×10^5, thus indicating outstanding UV light sensitivity under dark conditions. The MXene/GaN photodetector achieved a significantly superior performance to Au/GaN Schottky photodetectors under equivalent conditions, due to its elevated photo-to-dark current ratio. Fig. 9(c) demonstrates the linear response of the MXene/GaN photodetector photocurrent in the self-powered mode. The obtained data indicate that photodetectors maintain high-performance consistency at different light intensities and provide an average responsivity of 610 mA W^{-1} combined with an EQE of 210% and a specific detectivity reaching 6.8×10^{13} Jones. The excellent performance of the MXene/GaN photodetector arises from the strong built-in electric field at the MXene/GaN Schottky junction, which efficiently separates photogenerated carriers without any external power. Intrinsic high electrical conductivity and tunable surface chemistry of MXenes enhance the charge transport and reduce recombination losses, improving the sensitivity of the device. Unlike conventional metal contacts, MXenes form a more effective interface with GaN, resulting in significantly higher photocurrent and stability. The MXene/GaN Schottky photodetector works by creating a Schottky junction between MXenes and GaN, generating a built-in electric field at the interface. This field efficiently separates photogenerated electron–hole pairs when exposed to UV light, enabling self-powered operation without the need for an external bias. The high conductivity and tunable surface chemistry of MXenes enhance charge transport and reduce recombination losses, thereby improving the device's sensitivity and performance. The van der Waals heterojunction between MXenes and GaN creates an effective interface for charge separation, resulting in superior photocurrent generation and stability, making it ideal for UV photodetection.

Another study conducted by Lingling Chu *et al.*[183] utilizes ZnO as the light-absorbing layer in combination with MXenes and Si. The device structure of the MXene/ZnO/Si pyramid photodetector is shown in Fig. 9(d). ZnO, a wide-bandgap semiconductor with excellent light absorption properties, is crucial in the development of high-performance photo-

detectors. ZnO has a wide range of applications in optoelectronics due to its robust UV photoresponse and high exciton binding energy.[173,174] The device comprises three key layers, arranged as follows: MXene on top, ZnO in the middle, and Si at the bottom. The Si at the bottom undergoes an etching treatment to create a pyramid arrangement that increases light scattering and absorption abilities. The functioning of the device relies on ZnO as an intermediate light absorber, and MXenes provide efficient charge transport through their high conductivity and mobility capabilities. This heterojunction structure enables self-powered operation through the automatic generation of an electric field to control charge separation without any external powering.

The *I–V* curves for the MXene/ZnO/Si pyramid photodetector exposed to different wavelengths are shown in Fig. 9(e). The photodetector device exhibits its photocurrent response for multiple wavelengths, ranging from 405 nm to 810 nm, including 530 nm, 625 nm, 730 nm, and 810 nm. The maximum photocurrent occurs strictly at a wavelength of 625 nm, indicating peak performance in terms of sensitivity and responsivity at this wavelength. Fig. 9(f) presents the current-time plots for the MXene/ZnO/Si pyramid photodetector when it receives 625 nm illumination at different light intensities. The device demonstrated its technical capability to capture weak light signals through its high on/off ratio, which reaches 10^4 even at reduced light intensity levels. As the light intensity increases, the photocurrent value exhibits a direct relationship, indicating superior photoresponsivity of the device. This photodetector achieves a photo detectivity of 6.77×10^{11} Jones, a responsivity of 8.6 mA W^{-1}, and an external quantum efficiency of 1.72% when illuminated at 625 nm with incident light without external biasing. The device exhibits response characteristics with a 77.6 ms rise time and a 77.1 ms fall time, owing to the high charge mobility of MXenes, efficient light absorption by ZnO, and the increased surface area provided by the Si pyramid structure. The built-in electric field at the heterojunction between MXenes, ZnO, and Si promotes efficient charge separation and reduces recombination, leading to faster switching behavior. The strong performance of the MXene/ZnO/Si pyramid photodetector is due to its carefully designed heterojunction structure, where ZnO serves as an efficient light absorber, MXene provides fast carrier transport, and the Si pyramid base enhances light scattering and absorption. Microstructured interfaces improve light absorption, while the carefully designed material heterostructure reduces carrier recombination and facilitates efficient charge extraction. This combination of structural and electronic optimization allows consistent performance under different lighting conditions, providing stable signals and rapid response times in a self-powered configuration.

MXene nanosheets enhance the spontaneous ferroelectric polarization of the material, thereby strengthening the built-in electric fields at heterojunctions.[184,185] $BaTiO_3$ (BTO), a ferroelectric material, is recognized for its exceptional spontaneous polarization and robust pyroelectric and piezoelectric properties, rendering it ideal for optoelectronic applications.[173] The joint application of these elements utilizes the ferro-pyro-phototronic effect to enhance the device more effectively at sensing low light intensities. The research by Shulin Sha *et al.*[186] fabricated a BTO@MXene/4H-SiC heterojunction, as illustrated in Fig. 10(a). This schematic represents the photodetector's structural design, showing $BaTiO_3$ nanocrystals (BTO) on which the MXene nanosheet coating is used as a core–shell material, while mounted on top of a 4H-SiC (silicon carbide) wafer. The 4H-SiC (silicon carbide) wafer serves as the hole-transporting layer, whereas the BTO@MXene core–shell composite remains attached to it. The BTO nanocrystal modification with MXene nanosheets yields improved spontaneous ferroelectric polarization, thereby reinforcing the built-in electric field at the BTO@MXene and 4H-SiC heterojunctions. The photodetector functions autonomously by utilizing enhanced polarization and strengthened internal electric fields, which facilitate efficient charge separation and light detection at the junction.

The *I–V* characteristic curves obtained with the BTO@MXene/4H-SiC device are presented in Fig. 10(b). Both measurement scales include logarithmic and linear plots. Research shows that BTO@MXene/4H-SiC heterojunction devices exhibit rectifying characteristics under dark conditions, with a rectification ratio exceeding 10^3 within the voltage range from −4 V to +4 V. A Schottky contact forms at the BTO@MXene composite interface with the 4H-SiC semiconductor. While under 310 nm illumination, the BTO@MXene/4H-SiC photodetector exhibits measurable responsivity and detectivity, as depicted in Fig. 6(c) and (d), respectively. These results demonstrate that the device can effectively convert UV lights to electric signals with high efficiency and sensitivity. The BTO@MXene/4H-SiC heterostructure outperforms the undoped BTO/4H-SiC device, as its responsivity and detectivity increase until reaching saturation at elevated light power levels. The optimized BTO@MXene/4H-SiC photodetector reaches a maximum responsivity of 187.74 mA W^{-1}, an external quantum efficiency of 75.07%, and a detectivity of 6.52×10^{13} Jones while surpassing earlier BTO-based self-powered photodetectors by at least two orders of magnitude, as shown in Fig. 10(c and d). The BTO@MXene/4H-SiC photodetector exhibits a photoresponse with a rise time of 74.3 μs and a fall time of 122.7 μs when illuminated by 310 nm light, as illustrated in Fig. 10(e). Fig. 10(f) represents the wavelength-dependent photocurrent response of the BTO@MXene/4H-SiC photodetector, demonstrating its remarkable spectral selectivity in the ultraviolet range. The device achieves an optimal photoresponse at 310 nm, exhibiting a UV-to-visible photocurrent ratio above 10^3, hence validating its exceptional sensitivity to ultraviolet light while minimizing responses to visible wavelengths. The enhanced UV selectivity is ascribed to the synergistic effects of ferroelectric polarization and hot-carrier multiplication enabled by the MXene nanosheets. The device exhibits outstanding operational stability with repetitive and steady performance throughout consecutive cycles. Operating at a high speed with exceptional efficiency, the BTO@MXene/4H-SiC photodetector offers an

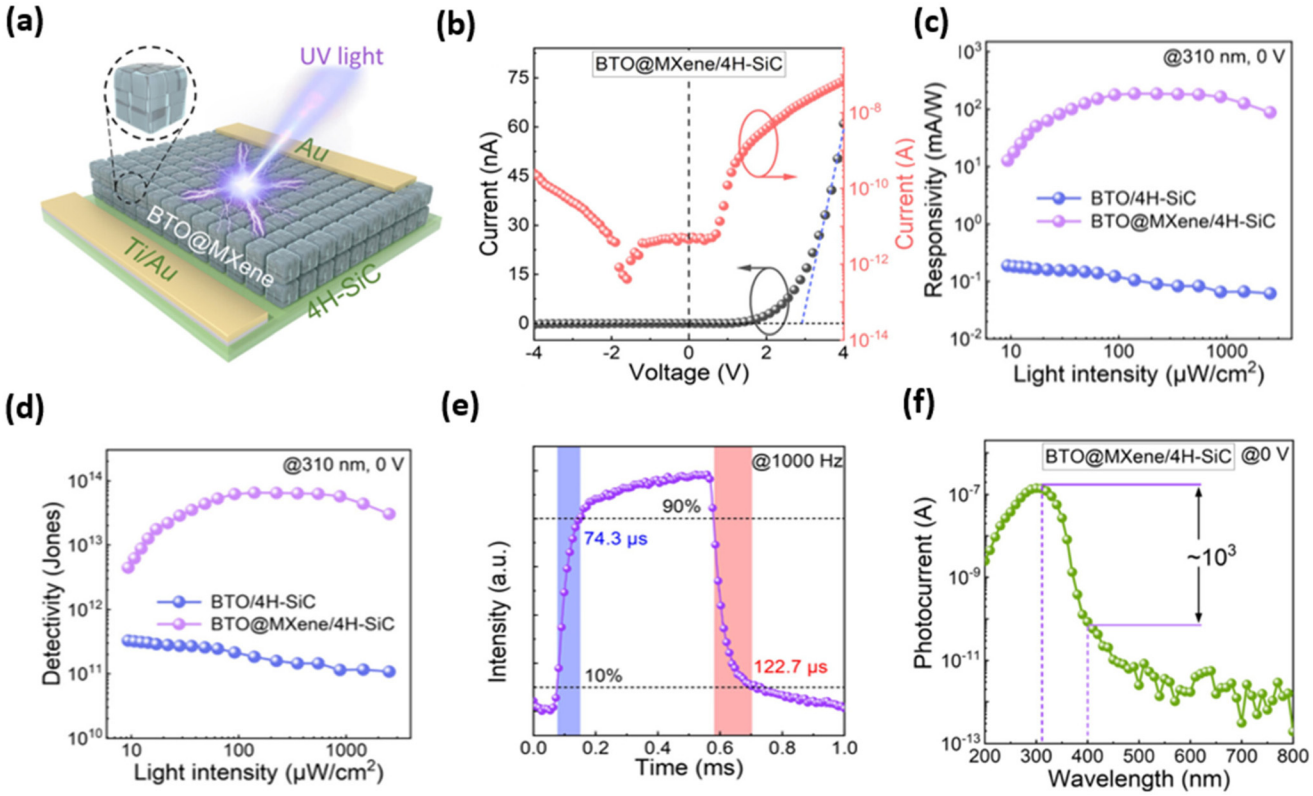

Fig. 10 (a) Schematic structure of the BTO@MXene/4H-SiC heterojunction device. (b) *I*–*V* measurements of BTO@MXene/4H-SiC heterojunction devices with both logarithmic and linear scales under dark condition. (c) *R* and (d) *D** as a function of incident light intensity at 0 V bias. (e) Transient photoresponse of the BTO@MXene/4H-SiC detector under a 310 nm LED illumination at 0 V bias (irradiance frequency of 1000 Hz). (f) Wavelength-dependent photoresponse of the BTO@MXene/4H-SiC device at 0 V bias. This figure has been reproduced from ref. 186 with permission from ACS Photonics, copyright 2024.

optimal solution for UV detection due to its extended operational stability, making it suitable for deployment in UV wireless communication systems.

The BTO@MXene/4H-SiC photodetector exhibits superior performance due to its high ferroelectric polarization and interface band engineering. The spontaneous polarization of the BTO is enhanced by the MXene nanosheets, thereby intensifying the internal electric field of the heterojunction, lowering the potential barrier, and accelerating the separation of the photo-excited carriers. The ferro-pyro-phototronic effect encompasses electric, thermal, and optical feedback, enabling the device to capture low-intensity UV luminescence with high sensitivity. Through self-powered rapid operation, the novel design, which utilizes charge–dipole interactions and intrinsic Schottky junctions, exhibits high responsivity and detectivity, distinguishing it from conventional photodetectors.

9. PN junction-based self-powered photodetectors

SPPDs built upon PN junctions operate autonomously since they utilize PN junction characteristics to convert photon impacts into electric signals without requiring external power sources. The interface of p-type and n-type semiconductors results in carrier diffusion across borderlines caused by the concentration gradient at the contact zone. A space charge region forms after carrier diffusion, allowing the p-side to become negatively charged while the n-side becomes positively charged to create a built-in electric field extending across the complete n-region to p-region.[187] These devices function through self-power because photon interaction with the junction produces charge carriers (electrons and holes) that perform as the power source. The photogenerated carriers are efficiently separated through the built-in electric field, facilitating rapid current generation. The spectral response of PN junction-based SPPDs extends from visible to infrared wavelengths, serving different types of optical applications. These devices offer exceptional noise characteristics, compact physical dimensions, and outstanding energy efficiency, making them suitable for use in various applications, including general scientific research, telecommunication systems, industrial operations, and outdoor environments. These photodetectors exist in two structural types: heterojunction and homojunction devices.[188]

9.1 Homojunction-based self-powered photodetectors

The unique electrical characteristics of 2D semiconductor homojunctions make them essential for SPPD applications

due to their distinctive structural properties. Self-generated p-type and n-type regions develop inside one material due to carrier concentration modifications through 2.[121] The quick charge propagation enabled by 2D semiconductors results from their thin nature, thereby reducing recombination losses, which enhances the device efficiency.[189] The built-in electric field in the photodetector enables self-powered operation, as it propels photogenerated carriers without requiring any external power source. This wide spectral sensitivity range, extending from UV to visible to infrared light, enhances the versatility of these materials for use in optoelectronic applications. These applications are enabled by the superior carrier mobility of 2D semiconductors, combined with their adjustable bandgap features and exceptional mechanical properties.[190,191] This work investigates WS2 homojunction-based SPPDs by assessing the distinctive properties of WS2 that enable high-performance photodetection.[121] This TMDC stands out because its monolayer form demonstrates direct bandgap properties that optimize light absorption. Due to its 2D structure, WS2 exhibits superior carrier mobility and flexibility, making it ideal for next-generation optoelectronic devices.[192,193] Jian *et al.*[121] fabricated a p–n WS_2 homojunction. Fig. 11(a) shows the optical device image exhibiting two marked regions using red dotted boxes to display WS_2, while white boxes show the h-BN encapsulation area. A dual-field-effect-transistor (FET) structure forms the homojunction within the device when the p-area of WS_2 connects to electrodes E1 and E2, with the n-area connecting to electrodes E2 and E3. The power density graph in Fig. 11(b) presents the decisive information about responsivity (R) and detectivity (D^*) for a self-powered homojunction photodetector. The resistivity exhibits stable behavior across all power densities, as indicated by the black curve data points in the figure, and detectivity maintains a steady state throughout the entire power density range. The device demonstrates its ability to detect weak light signals simultaneously with high sensitivity, regardless of changes in light intensity. The device can switch states because its light-on/off ratio reaches 8×10^4. The device photocurrent shown in Fig. 11(b) demonstrates logarithmic power density dependence, having an exponent (α) of 0.94 approaching the perfect value of 1, thus achieving high photo-capture efficiency.

The homojunction self-powered photodetector exhibits a rise time (τ_r) of 17.9 ms and a decay time (τ_d) of 15.9 ms, as shown in Fig. 11(c). The fast-switching capability of this photodetector is evident in its rise time, which measures the device response speed to light, and its decay time, which tracks the recovery to dark conditions. The performance of the device demonstrates its superior capabilities in operations that

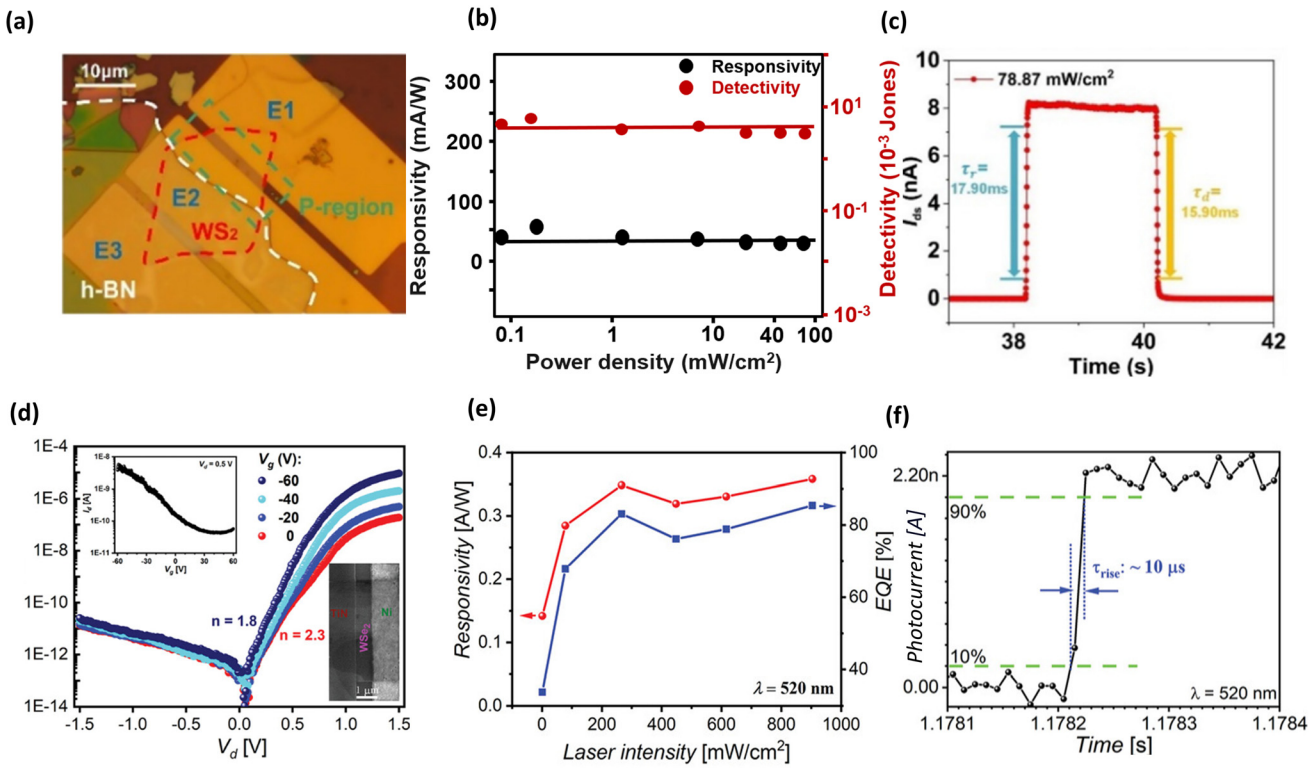

Fig. 11 (a) Optical image of the WS_2 p–n homojunction. (b) Change in R and D^* depending on the light power density at zero bias when using a 635 nm illumination. (c) Response speed of the device at a power density of 78.87 mW cm^{-2}. The WSe_2 homojunction photodetector schematic depicts TiN and Ni electrodes that provide doping to the metal contacts. (d) I_d–V_d curves of a TiN-WSe_2-Ni device under different gate biasing conditions. The insets shows the SEM image and I_d–V_g plot of the device. (e) R/EQE plots of the device at 520 nm. (f) Time-resolved photocurrent of the TWN diode with the laser on. This figure has been reproduced from ref. 121 and 194 with permission from Applied Physics Letters, copyright 2024. Advanced Functional Materials, copyright 2023.

require swift reactions due to its rapid response times. The device demonstrates dependable performance because its fast light and dark-state transitions operate within an extensive linear dynamic range. The photodetector demonstrates effectiveness in applications requiring simultaneous speed and high sensitivity due to its rapid response and signal detection capabilities.

Another researcher demonstrated that metal doping enables effective hole and electron injection for WSe_2 lateral homojunctions grown by CVD, as illustrated in Fig. 11(d) using TiN/Ni contact metals. Li *et al.*[194] employed the IR-heating chemical vapor deposition (CVD) method, which enabled the rapid growth of WSe_2 thin films in two dimensions. The maximum V_{oc} of 620 mV indicates that the device has an extensive built-in electric field that effectively separates generated charge carriers. The device demonstrates high efficiency in converting light exposure into electricity, achieving a power conversion efficiency (PCE) threshold of 15%. The device is an outstanding self-powered photodetector that detects illumination ranging from visible light to near-infrared wavelengths. The material exhibits outstanding photoresponsivity above 0.5 A W^{-1}, which is complemented by its rapid photoresponse of 10 μs under 520 nm illumination, as shown in Fig. 11(e). The photodiode shows an immediate response to a 520 nm laser, as shown in Fig. 11(f). The TiN-WSe_2-Ni (TWN) photodiode exhibits superior performance due to its enhanced photoresponsivity, rapid photoresponse time, and high efficiency in converting light into electric current signals. The device exhibits exceptional temporal performance and high-speed photodetection capability, making it suitable for various optoelectronic applications.

The high performance of the device is significantly benefited by the asymmetric Schottky barriers of the Ni and TiN contacts, which generate strong internal fields for expedited carrier separation. The metal doping and WSe_2 homojunctions grown by CVD yield clean interfaces and expedite the transport of charges. Efficient high photoresponse and high open-circuit voltage result from optimally aligned bands and minimized recombination, enabling broad-spectrum, high-speed, self-powered detection with high efficiency, surpassing conventional photodetectors in both spectral and time-domain performances.

9.2 Heterojunction-based self-powered photodetectors

Heterojunctions are integrated in SPPDs because these devices utilize built-in electric fields to create efficient electron–hole pair separation, leading to enhanced photoresponsivity and rapid detection at zero applied voltage. The performance outcomes of the optoelectronic devices have been improved through various material and technological combinations.[195–198] Due to their capacity to detect UV, as well as visible and infrared radiation, the optoelectronic applications of these materials become more versatile. The superior mechanical properties, adjustable bandgap ranges, and high carrier mobility of 2D semiconductors enable their utilization in various applications including wearable devices and enhanced photodetectors.[199,200] In the study by Wang *et al.*,[201] a heterojunction between PN MoS_2/Sb_2Te_3 structures for high-performance detection operations was fabricated. Fig. 12(a) shows the optical image of the final Sb_2Te_3/MoS_2 heterostructure-based device structure. The vdW heterojunction shows the stacking of a blue-colored monolayer MoS_2 flake above a purple Sb_2Te_3 layer. The device uses gold (yellow regions) as source and drain electrodes to connect the heterostructure for charging operations and photocurrent generation. The combination of MoS_2 and Sb_2Te_3 generates a built-in electric field at their interface when integrated, as both materials possess distinct electronic properties, being a TMDC and a topological insulator (TIs), respectively. The interfacial layer between MoS_2 and Sb_2Te_3 plays a key role in separating electrical charges, enabling successful self-powered photo-detection operation. The heterojunction works effectively for broadband high-sensitivity photodetection because MoS_2 exhibits strong light absorption and high carrier mobility of Sb_2Te_3.

The responsivity measurement of the Sb_2Te_3/MoS_2 vdW heterojunction photodetector at 700 nm occurs under different optical power conditions, as shown in Fig. 12(b). The inset shows the PN junction formation at the interface, which shows the *I–V* characteristics of the device. The heterojunction detects dark current at 2.38 pA with the zero bias and 1.16 nA with 1 V applied bias because it effectively blocks leakage currents. By measuring the *I–V* characteristics while illuminating at 500 nm, 700 nm, and 900 nm, the PV effect strengthens due to a built-in electric field that enables self-powered photodetection. The results show a direct relationship between the optical power input and the generated photocurrent, which proves the carrier separation mechanism. A positive bias application in the device enables efficient charge collection, increasing responsivity from 1.5 to 3 times higher. The broad-spectrum light detection capability of the device becomes apparent in the significant broadband photocurrent response shown in Fig. 12(c), thus making it ideal for diverse optoelectronic applications. At a wavelength of 660 nm, the device exhibits a maximum zero-bias responsivity of 170 mA W^{-1}, according to the normalized data on a shared scale. The photodetector obtains maximal efficiency for transforming light energy to electrical current at this specific wavelength. The high responsivity of the PD in the 600–700 nm range is primarily due to strong optical absorption by monolayer MoS_2 near its excitonic peak around 600 nm, where it efficiently generates electron–hole pairs. Additionally, the built-in electric field at the Sb_2Te_3/MoS_2 heterojunction enhances carrier separation and transport, resulting in greater photocurrent and improved responsivity at these wavelengths. Unlike conventional photodetectors, this device offers broadband detection, high zero-bias responsivity, and ultra-low dark current. Its integration of TMDC and TI materials delivers fast, efficient, and low-power photodetection, making it ideal for advanced optoelectronic applications.

In general, heterojunction-based SPPDs achieve a self-powered functionality through the interfacial potential difference that naturally arises when two materials with distinct band structures are joined. This potential gradient drives

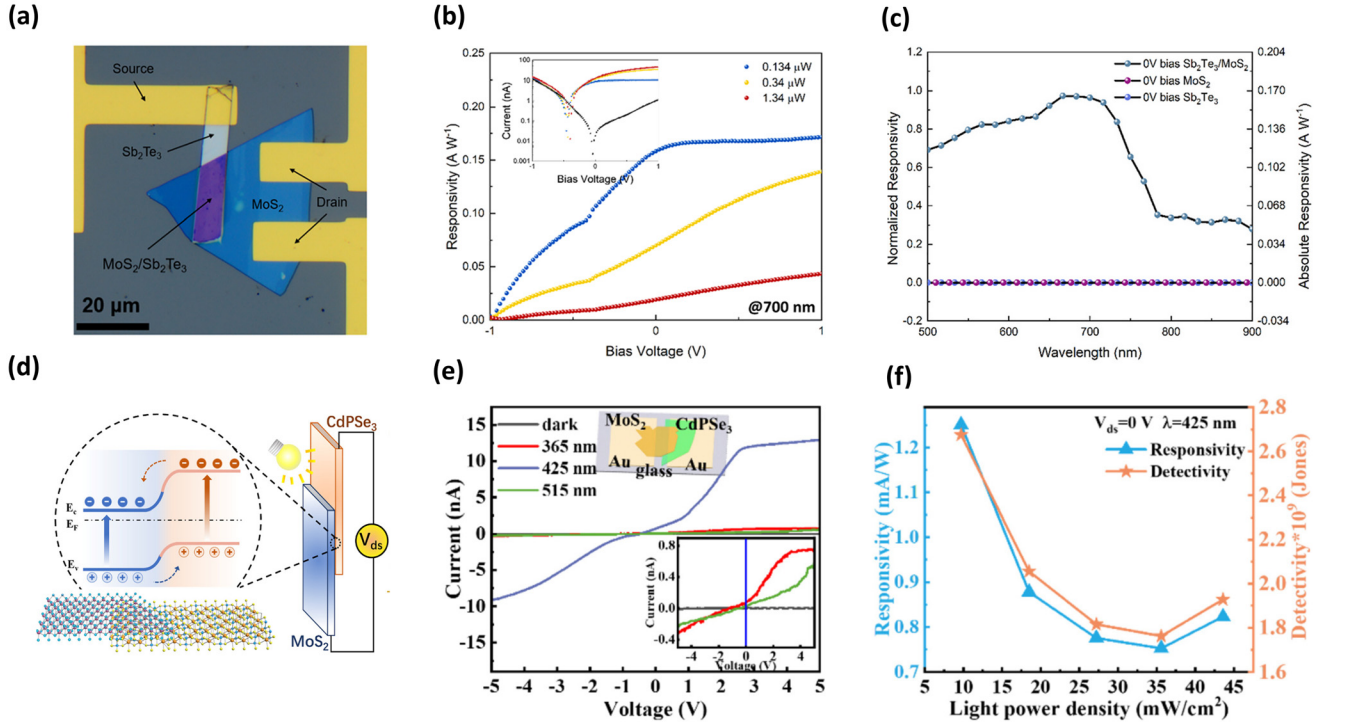

Fig. 12 (a) Optical microscopic image of the PN junction device. (b) Measured photoresponsivity at 700 nm wavelength under −1 to 1 V bias voltage. When the device is operated at zero bias, the photoresponsivity responded clearly to the optical power using a linear pattern. (c) Normalized responsivity reveals a wide wavelength response under 0-bias conditions by sweeping from 500 to 900 nm with 10 nm steps. (d) Device layout, presenting the heterojunction structure of $CdPSe_3/MoS_2$, while the photoelectric response measurement of the $CdPSe_3$ photodetector (CPS) occurs under applied bias conditions (e) Photoelectric response test of the CM device. *I*–*V* curves of CM under 365, 425, and 515 nm illumination. The insets shows a schematic diagram of the CM device and zoomed-in *I*–*V* curves. (f) Calculated *R* and *D** values at 0 V bias voltage illuminated by different light intensities of the 425 nm laser diode. This figure has been reproduced from ref. 201 and 202 with permission from Nanophotonics, copyright 2022. ACS Applied Materials & Interfaces, copyright 2024.

photoexcited carriers in opposite directions, producing a photocurrent even in the absence of an external supply. Such a mechanism not only reduces energy consumption but also enhances device stability, since the detection process relies on internal fields rather than the applied bias. By carefully selecting material pairs with complementary optoelectronic properties, heterojunction designs can therefore be tailored to deliver efficient and sustainable self-powered photodetection.

Building on the advancements in van der Waals heterostructures, Yang *et al.*[202] designed a photodetector containing a Type-II heterostructure of $CdPSe_3$/MoS2 heterojunction to enhance the light response capabilities while maintaining exceptionally low dark current. The photodetector device employs a Type-II heterojunction vdW heterostructure that integrates $CdPSe_3$ with MoS_2. The built-in electric field at the interface emerges because p-type $CdPSe_3$ joins n-type MoS_2 semiconductors. Type-II heterostructures are preferred due to their excellent carrier mobility, tunable bandgap features, and efficient charge separation capabilities.[203] Under illumination, photoexcited electrons and holes separate due to the internal electric field, which results in higher responsivity and lower recombination losses. A built-in mechanism provides these materials with independent energy capabilities, requiring no external power source, which enables their use in low-energy optoelectronic systems. Fig. 12(d) demonstrates the $CdPSe_3/MoS_2$ heterojunction structure and explains the charge transfer mechanism. Light exposure causes the production of electron–hole pairs that occur at the interface. The built-in electric field causes electrons to flow toward MoS_2 and simultaneously drives holes to $CdPSe_3$, resulting in effective charge separation.

The device was tested under different light wavelengths, including 365 nm, 425 nm, and 515 nm, as well as under dark conditions, as presented in Fig. 12(e). Under 425 nm illumination conditions, the device generates a substantial photocurrent, demonstrating its highest light sensitivity in this wavelength range. The device structure is presented in the inset image. The heterostructure exhibits performance enhancement because the built-in electric field enables efficient carrier separation, while the single-material $CdPSe_3$ device lacks this feature. The results in Fig. 12(f) demonstrate a direct relationship between the applied 425 nm light power density and photocurrent response. The $CdPSe_3/MoS_2$ heterostructure photodetector reached its peak response of 91.12 mA W^{-1} combined with 1.74 × 10^{11} Jones detectivity while operated at 5 V bias under 425 nm illumination. Due to its low dark current operating within the pA range, the device maintained excellent

signal-to-noise capability. The distinct electronic structures of p-type $CdPSe_3$ and n-type MoS_2 result in staggered energy bands that facilitate charge transfer and extraction. The intense light absorption arises from the complementary band gaps of the two materials, enabling excitation of electron–hole pairs over a broad spectral range. Additionally, the low intrinsic defect density reduces trap-assisted recombination, further enhancing charge carrier lifetime and device sensitivity.

The $CdPSe_3/MoS_2$ heterostructure illustrates how Type-II band alignment facilitates directional charge flow, where electrons and holes are naturally directed to different layers. This built-in separation minimizes recombination and supports high detectivity without relying on the external bias. Such interfacial design strategies illustrate the potential of vdW heterostructures for efficient and energy-saving self-powered photodetection.

10. Janus and their heterostructure-based self-powered photodetectors

Photodetectors based on self-powered Janus materials utilize their built-in asymmetry between surfaces to transform light into electrical signals, functioning independently of external power sources. The different atomic structures on the top and bottom sides of Janus materials automatically break inversion symmetry, resulting in an internal electric field. The built-in field enables efficient charge separation along with transportation, thus allowing autonomous photodetection functions without any external power supply.

Janus-based SPPDs operate in a self-powered mode, where light absorption leads to the generation of photogenerated charge carriers. Due to the asymmetry-induced internal polarization field separating photo-generated electron–hole pairs, attracting electrons toward one layer and directing holes toward the opposite layer become possible. When separated, charge carriers automatically generate a photocurrent, leading to highly efficient light detection. The devices demonstrate widespread spectral sensitivity combining visible and near-infrared wavelengths, thus enabling their use across polarization-sensitive imaging, optoelectronic sensing, and quantum optical communication.

10.1 Intrinsic Janus-based SPPDs

In Janus materials, there also exist compounds that naturally have intrinsic asymmetry without heterostructure engineering, capable of being self-standing active SPPD layers. Intrinsic Janus monolayers exhibit a straightforward yet extremely efficient self-powered photodetection platform, resulting from spontaneous internal polarization fields and distinctive optoelectronic features.

CrSBr stands out among these materials because it demonstrates layered vdW semiconductor qualities, including structural anisotropy, air stability, and polarization-sensitive behavior. The unique combination of characteristics present in Janus-based CrSBr devices produces exceptional functionality for position-sensitive and polarization-resolved self-powered binary photodetection.[204]

Panda *et al.*[127] constructed single Janus-based CrSBr (SPPD) by fabricating a Schottky junction that uses asymmetric Au–CrSBr–Au interfaces. The electrical charge separation mechanism at metal–semiconductor interfaces generates a built-in potential, enabling photodetection independently of external power sources. Fig. 13(a) displays the structure of the CrSBr photodetector, including Schottky junctions that develop between gold (Au) electrodes on the CrSBr surfaces. The device operates without any external power *via* built-in electric fields at Au–CrSBr junctions on a SiO_2/Si substrate.

The nonlinear diode behavior in the device *I–V* characteristics demonstrates Schottky junction formation at the Au–CrSBr interface, as shown in Fig. 13(b). The asymmetric curve confirms that the device contains an internal electric field, enabling self-powered operation in the photodetector. The inset image shows an optical image of the fabricated device, which shows transparent electrodes combined with a proper CrSBr flake arrangement to facilitate efficient charge movement. High responsivity and detectivity can be achieved using the Schottky junction configuration to efficiently separate photo-generated carriers. The photodetector data in Fig. 13(c) reveal that the photodetector reaches a steady state in 52 ms while decaying in the following 38 ms, indicating its high-speed photodetection through fast carrier dynamics. The photodetector requires a quick response time for carrying out real-time optical sensing as well as imaging and communication applications. Under 514 nm excitation at ambient conditions, the photodetector exhibits high photoresponsivity, reaching ~0.26 mA W^{-1} with detectivity of 3.4×10^8 Jones. The asymmetry induces an internal polarization field, further enhancing the charge separation efficiency. The material's air stability ensures durability, while its mixed chalcogen-halide composition facilitates strong light absorption in the visible range. Together, these properties enable CrSBr photodetectors to operate with high responsivity, rapid response speed, and excellent polarization sensitivity, making them highly suitable for next-generation optoelectronic applications.

The key advantage of Janus-based SPPDs lies in their intrinsic polarity, which creates a natural driving force for carrier separation without complex device engineering. This built-in asymmetry ensures efficient photodetection while maintaining structural simplicity, allowing devices like CrSBr photodetectors to combine stability, rapid response, and polarization sensitivity within a single self-powered platform.

Following the advancements with CrSBr, Xiong *et al.*[205] fabricated a self-powered broadband photodetector using continuous $WS_{0.9}Se_{1.1}$ films that achieved excellent performance throughout the UV-Vis-NIR spectral region. The device design with Ag/$WS_{0.9}Se_{1.1}$/Ag layers produced a photodetector with high responsivity, fast response time, and excellent detectivity. The constructed device deposits silver (Ag) electrode layers on a $WS_{0.9}Se_{1.1}$ film, on a SiO_2/Si substrate, as depicted in Fig. 13(d). This device design enables effective light absorption as well as efficient charge separation.

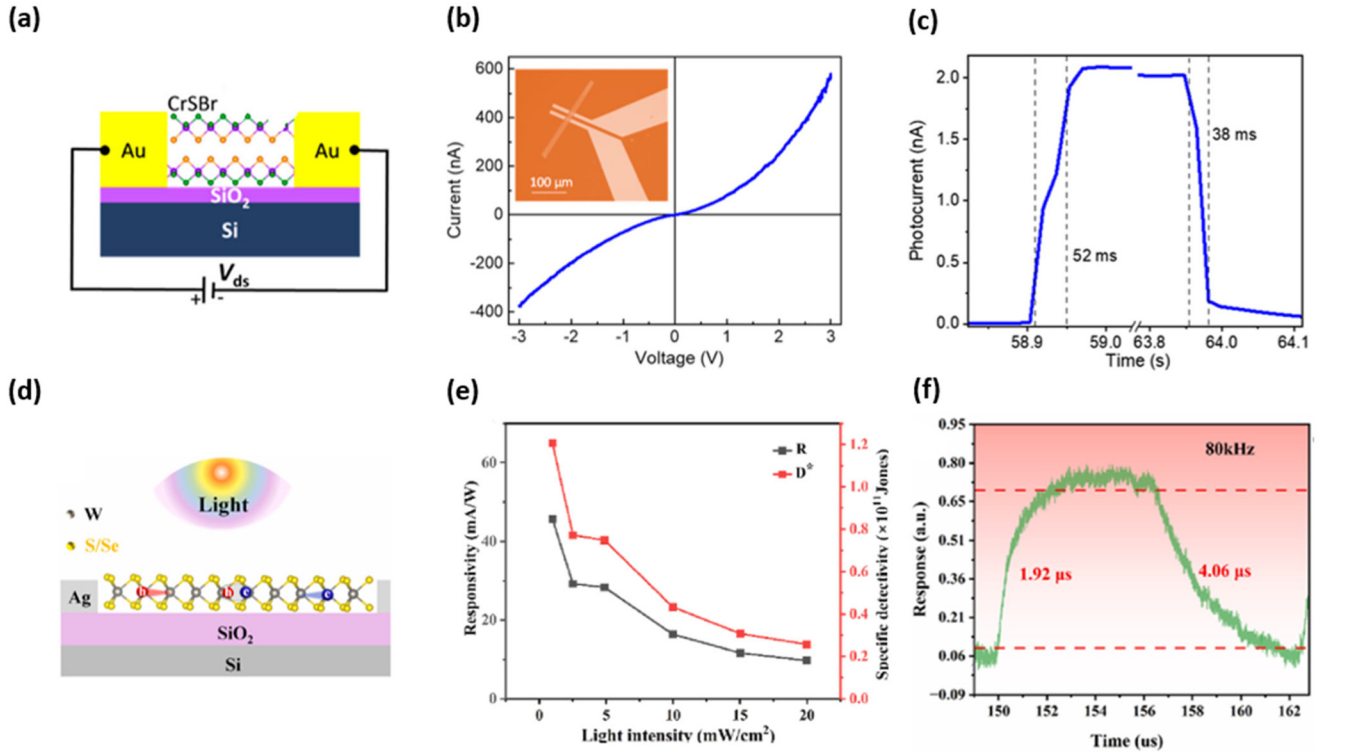

Fig. 13 (a) Measurement setup design and (b) self-biased optoelectronic properties of an 82 nm CrSBr flake. *I*–*V* characteristics of the device under dark condition. The inset contains an optical image of the device. (c) Photoresponse time and recovery time of the CrSBr device. (d) Cross-section of the photodetector Ag/$WS_{0.9}Se_{1.1}$/Ag. (e) Photocurrent responsiveness of the devices and the relationship between specific detectivity and light intensity. (f) Response time at 80 kHz. This figure has been reproduced from ref. 205 and 206 with permission from Optical Materials, copyright 2023. ACS Applied Materials & Interfaces, copyright 2023.

An advantage of the $WS_{0.9}Se_{1.1}$ photodetector over conventional materials includes its ability to detect a wide range of wavelengths while conducting self-powered operation at fast speeds with high sensitivity. The bandgap tunability of this material makes it suitable for detecting light waves between UV and NIR wavelengths. At 365 nm, the device achieves a high level of responsivity, reaching 1.5 A W^{-1}, with a specific detectivity measurement of 1.20×10^{11} Jones, indicating high sensitivity to faint light signals. The device operates independently of external power, utilizing its built-in electric field to separate charges. The photocurrent increases proportionally with light intensity, as shown in the *I*–*V* curves. The device operates as a self-powered system because its *I*–*V* characteristics produce different asymmetries depending on the illumination intensity. The responsivity value decreases as the light intensity increases due to saturation effects at high power densities, as shown in Fig. 13(e). Response time measurements demonstrate that the device rapidly generates and decays photocurrent, indicating its high-speed operation capability. The photodetector exhibits fast response times of 1.92 μs for rising signals at 80 kHz, while the fall time reaches 4.06 μs, as shown in Fig. 13(f). The device uses bandgap tunability and internal polarization from the Janus asymmetry to achieve enhanced light–matter interaction and broad-spectrum absorption. The device offers stable broadband detection capabilities, enabling applications across various optoelectronic systems for imaging, sensing, and communication technologies.

The broadband efficiency of the $WS_{0.9}Se_{1.1}$ photodetector arises from the combined effects of bandgap tunability and intrinsic asymmetry, which establish strong internal fields for carrier separation. These features enable the device to maintain high responsivity across a wide spectral range while ensuring rapid response times, underscoring the advantages of Janus-based films for versatile, self-powered photodetection.

10.2 Janus heterostructure-based SPPDs

Janus-based heterostructures produce powerful SPPDs through their asymmetric structure, which generates built-in electric fields that assist charge separation and minimize charge recombination.[128] The engineering process of bandgap allows researchers to extend the device range from UV to near-infrared light absorption.[207] The strong connection between heterostructures improves carrier transport while increasing the responsivity and detectivity levels of the device.[208] The vdW interactions in these heterostructures decrease dark current levels and enhance device stability for suitable use in future low-power sensitive optoelectronic applications.[209] A self-powered photodetector, GaN/SnS_2/SnSSe heterostructure, with photodetection capabilities covering the ultraviolet spectrum, was fabricated by Maity *et al.*[207] The device configuration in

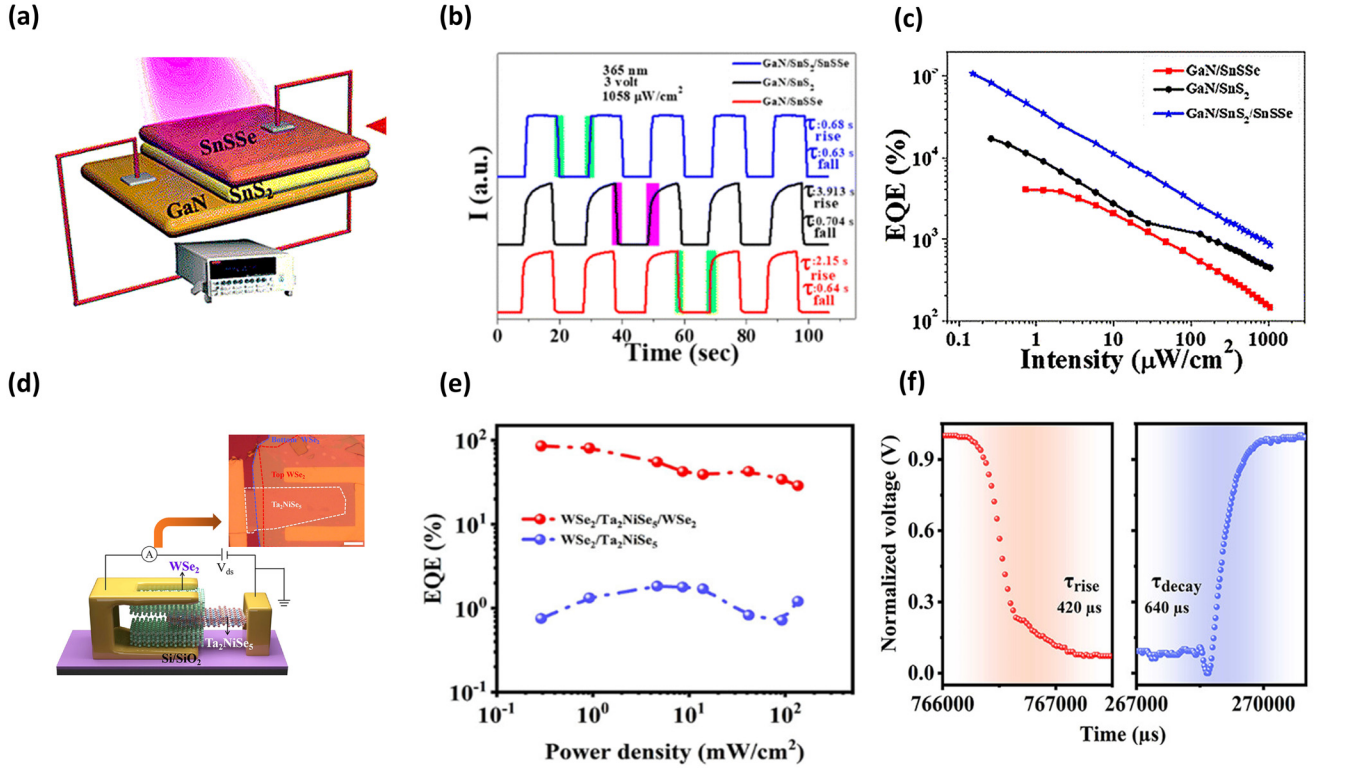

Fig. 14 (a) Schematic of the final device under UV radiation. (b) Intensity-dependent photo-switching occurring when the device is operated at 3-volt fixed bias. (c) Intensity-dependent EQE for different device configurations. (d) Schematic of the $WSe_2/Ta_2NiSe_5/WSe_2$ vdW DHJ device (e) Comparison of the photoelectric performance of the DHJ device with an SHJ device photodetector. EQE as a function of light power density under a 635 nm illumination at 0 V in DHJ and SHJ devices. (f) Rise and decay times at 635 nm wavelength (24 mW) when operating in the self-powered mode. This figure has been reproduced from ref. 128 and 207 with permission from ACS Applied Materials & Interfaces, copyright 2023. Nanoscale Horizons, copyright 2024.

Fig. 14(a) demonstrates a vertically arranged heterojunction between SnS_2/SnSSe layers on a GaN base, creating a vdW interface for efficient carrier separation and charge transport.

Various measurements show the performance of this photodetector during electrical and optical examinations. The device exhibits stable and rapid photoresponsive characteristics in response to multiple UV light pulses, as illustrated in Fig. 14(b), demonstrating its excellent detection capabilities and consistent behavior. The fast detection capabilities of this device are shown by its quick switching time, with a rise time of 2.15 seconds and a fall time of 3.913 seconds. The GaN/SnS_2/SnSSe heterostructure shows a better external quantum efficiency (EQE) than that of other configurations because it maintains a high EQE value at low light intensity levels. The heterostructure exhibits exceptional photon-to-electron conversion capability under 365 nm illumination at an intensity of 150 nW cm^{-2}, achieving an external quantum efficiency upon biasing at 3 V, as shown in Fig. 14(c). The exposure of the device to 365 nm illumination enables an outstanding responsivity of 314.96 A W^{-1}, along with a specific detectivity of 2.0×10^{14} Jones. Using SnSSe as a material allows researchers to expand the photodetection range alongside improved responsivity and detectivity performances. This heterostructure consistently enhances light absorption and charge transport, making it a promising candidate for future bias-free optoelectronic systems. This intrinsic mechanism supports high responsivity and low dark current while extending detection across a broad spectral range, underscoring the promise of Janus heterostructures for next-generation self-powered optoelectronic devices.

In another study conducted by Zheng *et al.*,[128] a high-efficiency self-powered photodetector was fabricated using a $WSe_2/Ta_2NiSe_5/WSe_2$ vdW dual heterojunction (DHJ). Light absorption and charge separation occur within the sandwich-like structure shown in Fig. 14(d) due to opposing built-in electric fields between heterojunction interfaces. The spectral response of the DHJ photodetector extends from 400 to 1550 nm, making it practicable for multi-wavelength detection applications. The device performance was exceptional under 635 nm illumination because it obtained an ultrahigh EQE of 85.5% accompanied by a power conversion efficiency (PCE) of 1.9%, as shown in Fig. 14(e), which surpassed the performance of the single heterojunction device. The response times for both the rise time (420 μs) and the decay time (640 μs) were recorded using the DHJ photodetector, as shown in Fig. 14(f), demonstrating its high-speed optical detection capability.

The $WSe_2/Ta_2NiSe_5/WSe_2$ DHJ offers exciting prospects as a potential future optoelectronic and imaging technology solu-

tion because of its high efficiency, broadband operation, and polarization-sensitive properties. Its superior performance originates from the dual built-in fields formed at the two heterointerfaces, which reinforce carrier separation and suppress recombination. This synergistic mechanism, together with the anisotropic characteristics of Ta_2NiSe_5, enables broadband sensitivity, polarization-dependent detection, and stable self-powered operation across multiple wavelengths.

11. Flexible substrate-based SPPDs and heterostructures

SPPDs fabricated on flexible substrates are gaining attention due to their lightweight, mechanical durability, and suitability for integration into deformable wearable electronic systems.[131] High-performance photodetection functions thrive in devices built on polyethylene terephthalate (PET) or polydimethylsiloxane (PDMS) polymeric substrates due to their stretchable and curved capabilities.[210] These flexible substrates offer significant benefits for next-generation technologies due to their inherent flexibility, which enables their application in bio-integrated sensors, foldable electronics, and conformal imaging systems.[211,212]

Nguyen *et al.*[143] demonstrated the fabrication of a flexible SPPD with optical signal encryption capabilities using a $Ti_3C_2T_x$ MXene-based platform. A heterostructure composed of $Ti_3C_2T_x/Al_2O_3/ZnO/Ti_3C_2T_x$/ITO/PET serves as a device that leverages MXene's superior charge transport capabilities and transparency properties. Fig. 15(a) illustrates a layered structure that utilizes an MXene film as a Schottky barrier and a charge-transporting layer.

The photodetector exhibits a rapid photoresponse behavior with a rise time of 8 μs and a fall time of 30 μs, as illustrated in Fig. 15(b). The MXene layer and distinctive binding between Al_2O_3 and ZnO layers enable efficient charge transport, thus leading to fast response times. The device utilizes two photodetection effects simultaneously through photoconductivity and pyroelectricity, as demonstrated in Fig. 15(c). The device becomes more effective at detecting weak optical signals due to fluctuations in light intensity, because of the pyroelectric contribution. The superior detection sensitivity of this device stems from responsivity and detectivity values of 0.34 A W^{-1} and 1.4 × 10^{13} Jones, respectively. The performance of the device is defined by its flexibility and high optical transparency, exceeding 68%. The device performs exceptionally well in wearable and optoelectronic communication systems due to its transparency and mechanical flexibility. The structural stability of the device was tested through repeated bending to demonstrate its durability when applied to flexible devices. MXenes exhibit high surface conductivity and rich functional

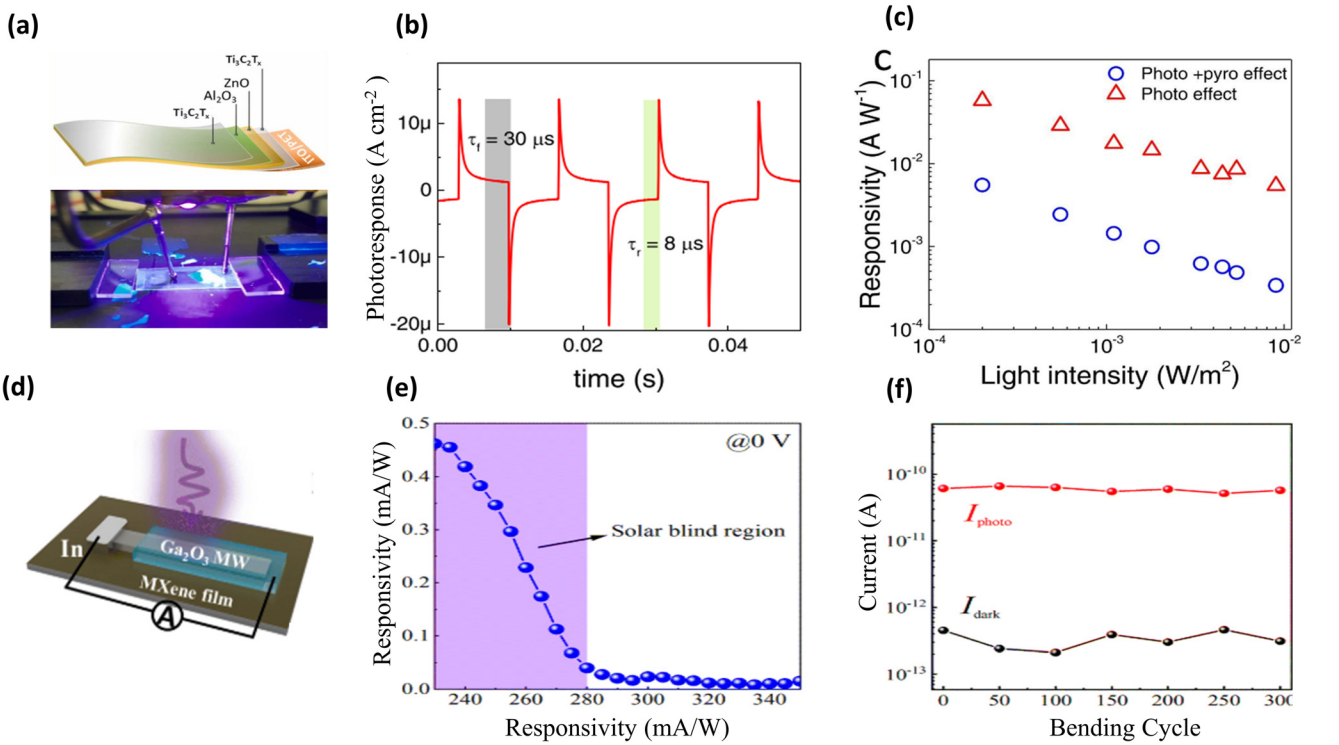

Fig. 15 (a) Schematic of the device with E-$Ti_3C_2T_x$, and a digital image of the measurement setup, where a light wavelength of 365 nm is used, (b) Performance of the $Ti_3C_2T_x/Al_2O_3/ZnO/Ti_3C_2T_x$/ITO/PET TPD including photo-response speed (c) and responsivity. (d) Schematic of the Ga_2O_3 MW/MXene photodetector. (e) Photoelectric characteristics and energy band diagram of the Ga_2O_3 MW/MXene photodetector. Spectral responsivity obtained at zero bias (f) I_{photo} and I_{dark} of the device at different bending cycles (bending angles = 60°). This figure has been reproduced from ref. 215 and 216 with permission from Nano Energy, copyright 2023. CrystEngComm, copyright 2023.

terminations (–OH, –F, –O), which facilitate efficient charge transport and strong interfacial bonding with oxide layers, such as Al_2O_3 and ZnO, thereby minimizing trap states and enhancing carrier mobility. Moreover, the layered structure enables smooth charge flow and allows for transparent light entry, while the flexible PET substrate ensures mechanical durability under bending. The simultaneous use of photoconductive and pyroelectric effects, enabled by the polar crystal structure of ZnO, enhances the device's sensitivity to weak and fluctuating light signals, distinguishing it from conventional SPPDs. This performance stems from the coupling of polarization-induced internal fields with interfacial charge transport, where MXene's surface terminations facilitate efficient carrier mobility while minimizing trap states at oxide interfaces. These synergistic effects ensure the rapid and stable generation of photocurrents. When integrated on PET substrates, they preserve self-powered functionality under bending, establishing a reliable pathway toward flexible and wearable optoelectronics.

Furthermore, Tang *et al.*[159] fabricated a flexible self-powered solar-blind photodetector that utilizes Ga_2O_3 microwires (MW) connected to MXenes. The schematic (Fig. 15(d)) of the device shows its configuration with a Ga_2O_3 MW/MXene junction that efficiently separates charges due to the strength of its built-in electric field at the contact point. The device design enables high-sensitivity detection of solar-blind UV light. The photodetector achieved a powerful responsivity of 0.25 mA W^{-1}, with a detectivity reaching 4×10^9 Jones under 254 nm UV irradiation, as shown in Fig. 15(e). The photodetector demonstrates efficient operation within the solar-blind spectrum because conventional detectors fail due to interference from visible light.

The photodetector demonstrated reliability based on cyclic bending tests, which reached 300 cycles without showing any significant changes in photocurrent or dark current levels, as presented in Fig. 15(f). Repeated mechanical bending does not affect this material's photoresponse, indicating its excellent potential to work in flexible electronic applications. The ultra-wide bandgap of Ga_2O_3 (~4.9 eV) enables it to absorb only deep-UV photons, blocking visible light and allowing for high spectral selectivity. Meanwhile, the MXene contact forms a low-barrier junction, promoting rapid carrier extraction due to its high conductivity and work function alignment. Moreover, the built-in electric field at the Ga_2O_3/MXene interface efficiently separates photogenerated carriers, and the microwire geometry ensures localized, directed charge transport with minimal recombination.

The Ga_2O_3 MW/MXene photodetector derives its performance from the synergy between Ga_2O_3's ultra-wide bandgap, which ensures deep-UV selectivity, and the built-in electric field at the heterojunction that drives efficient carrier separation. The MXene contact provides a low-barrier pathway for rapid extraction, while the microwire geometry suppresses recombination through directed transport. These combined mechanisms enable solar-blind detection with high spectral selectivity and mechanical durability under repeated bending, outperforming conventional rigid detectors.[214]

11.1 Heterostructures on flexible substrates

Research on 2D heterostructures combined with flexible materials has led to the fabrication of efficient self-powered photodetectors (SPPDs).[217] These layered materials, built from van der Waals (vdW) components, including MoS_2, WS_2, graphenes, and h-BN, enable wearability and elasticity through their adjustable band edges and strong light-interaction characteristics.[213,218] The optoelectronic properties of these materials change in response to strain applications, leading to performance improvements that include faster response times, improved mechanical stability, and higher responsivity. Self-powered photodetection becomes feasible through a combination of built-in electric fields or asymmetric Schottky junctions, eliminating the need for external power. Next-generation soft electronics, bio-integrated sensors, and intelligent imaging systems will use 2D heterostructures as fundamental materials.[219]

Jang and Choi *et al.*[131] developed an SPPD device that utilizes a trifluoromethanesulfonyl-amide (TFSA)-GR/WS_2 vertical heterostructure as a semitransparent, flexible photodetector device. The device in Fig. 16(a) combines fast charge carriers of graphene with intense light–matter coupling of WS_2 to create a powerful van der Waals heterostructure. Doping graphene with trifluoromethanesulfonyl-amide (TFSA) helps control the built-in electric field in the device, enabling it to operate without requiring an external power source. This enables efficient self-powered performance by enhancing the charge separation and transport within the device.

The photoresponse characteristics of the TFSA-GR/WS_2 photodetector reveal impressive performance across a broad ultraviolet-to-visible (UV-Vis) spectrum. The responsivity (R) achieves 0.14 A W^{-1} together with an EQE of 40% and a detectivity (D^*) of 2.5×10^9 Jones at 400 nm, as shown in Fig. 16(b). The heterostructure exhibits exceptional light absorption capabilities, serving as a key performance indicator. The device has an extended absorption range, allowing it to detect a wide bandwidth during photodetection operations. The device's resistance to mechanical bending was examined through repeated tests, as shown in Fig. 16(c). Twice-daily bending of the heterostructure through 3000 cycles demonstrated that the photodetector output retained 88% of its original detection capabilities, indicating excellent long-term durability for wearable electronics applications. The excellent performance of the device stems from TFSA doping, which enhances the built-in electric field of graphene for efficient charge separation, combined with the strong light absorption of WS_2 across the UV-Vis spectrum.

The TFSA-GR/WS_2 heterostructure highlights how doping-induced modulation of graphene's built-in field, combined with the intense light–matter interaction of WS_2, enables efficient charge separation and broadband absorption without any external bias. The vdW interface ensures rapid carrier transport with minimal recombination, while the flexible platform sustains high performance under extensive bending. Together, these mechanisms establish a durable, self-powered,

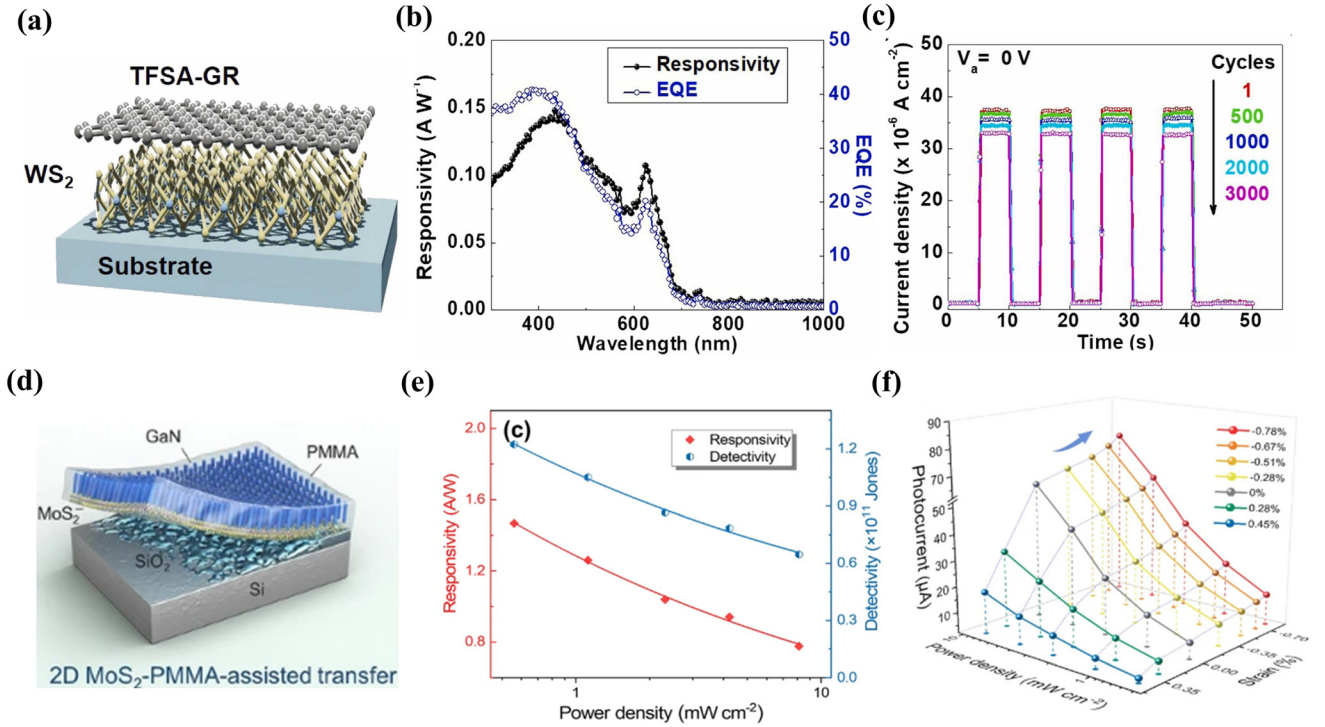

Fig. 16 (a) Schematic of the TFSA-GR/WS_2 photodetector. Band diagrams of the PD (b) spectral responsivity and EQE at zero bias. (c) Repeated on/off switching behaviors of current density at zero bias for various light powers. (d) Schematic of vertical heterostructures for flexible photodetector arrays. (e) Variations in photocurrent for different power densities and strain values. (f) Photocurrent for different strained photodetectors under increasing illumination power densities. This figure has been reproduced from ref. 131 and 221 with permission from the Journal of Alloys and Compounds, copyright 2022. Nano-Micro Letters, copyright 2025.

and spectrally versatile photodetector ideally suited for next-generation wearable and conformal optoelectronics.

Tang *et al.*[220] reported a flexible photodetector based on a vertical heterostructure composed of GaN nanorod arrays (NRAs), MoS_2, and PEDOT:PSS. The 1D GaN NRAs constructed on 2D MoS_2 increase light absorption and carrier separation, as depicted in Fig. 16(d). The PEDOT:PSS layer functions as a hole transport layer because this structure enhances the extraction of charges. The device functions autonomously, with a UV illumination responsivity of 1.47 A W^{-1} and a detectivity of 1.2 × 10^{11} Jones, and has response times of 54/71 μs. The response and detection abilities decrease progressively as the power density increases due to recombination effects, as shown in Fig. 16(e). The application of a compressive strain of −0.78% induces piezo-polarization charges, improving both device responsivity to 2.47 A W^{-1} and detectivity to 2.6 × 10^{11} Jones.

Fig. 16(f) shows that the device maintains a stable photocurrent after undergoing 300 bending cycles, indicating its strong mechanical durability. The device exhibits a strain-dependent response, verifying the phenomenon known as piezophototronics, which enhances charge separation performance under compressive strain conditions. The photodetector offers real-time UV sensing and imaging capabilities, making it suitable for wearable UV monitoring and flexible imaging applications. The superior performance of the device arises from GaN nanorods enhancing light absorption and charge separation with MoS_2, while PEDOT:PSS aids efficient hole transport. Compressive strain induces piezoelectric polarization in GaN, enhancing the built-in electric field and improving responsivity and detectivity. Its strain-tunable photoresponse and mechanical durability after bending cycles make it ideal for flexible, wearable UV sensing, outperforming traditional rigid photodetectors.

12. Schottky junction-based SPPDs and their heterostructures

SPPDs that use Schottky junctions extract power from metal–semiconductor built-in electric fields to split charges based on the metal–semiconductor interface.[222] The Schottky barrier established between a semiconductor and a metal drives photogenerated carrier movement through the device, leading to efficient operation and high-speed response in addition to very low dark current.[222] The combination of heterostructure Schottky SPPDs with 2D materials, such as MoS_2, WS_2, and graphenes, alongside bulk semiconductors or metals, yields devices that offer superior photoresponsivity and broadband detection capabilities, as well as adjustable band alignments.[223,224] Thanks to their strong light–matter inter-

actions combined with rapid carrier transport, these heterostructures perform exceptionally well in optoelectronic devices, wearable systems, and transparent sensors. Recent breakthroughs in SPPDs have emerged through band engineering, doping methods, and the implementation of flexible substrates, making efficient large-scale SPPD designs possible.

Tong *et al.*[225] fabricated a photodetector composed of asymmetric van der Waals (vdW) contacts connected through graphene/WSe_2/graphene (Gr/WSe_2/Gr), as shown in Fig. 17(a). A dry-transfer integration process couples different thickness graphene electrodes with monolayer WSe_2 while minimizing defects and suppressing Fermi-level pinning at interfaces. The charge-carrier separation and collection improved because the asymmetric Schottky barriers formed by the graphene electrodes function in the device.

The photodetector achieves superior performance characteristics through its 20.31 mA W^{-1} responsivity, along with an open-circuit voltage of 0.37 V and a light-to-dark ratio of 10^6, as shown in Fig. 17(b). The device responds strongly to visible wavelengths following illumination at 488 nm, 532 nm, and 633 nm and performs better at shorter wavelengths. The observed pattern proves that the device can detect broadband light signals with adjustable response behaviors. The device exhibits rapid photodetection, with a rise time of 42.9 μs and a decay time of 56.0 μs, as shown in Fig. 17(c). Repeated switching tests verify that the Gr/WSe_2/Gr photodetector exhibits dependable operation properties for practical implementation. The results showed that graphene-based heterostructures offer excellent prospects for developing next-generation optoelectronic equipment, such as wearable sensors, imaging systems, and optical communication technologies. Repeated switching tests confirm the reliable performance of the Gr/WSe_2/Gr photodetector for practical applications. The strong van der Waals bonding between graphene and WSe_2 creates clean, defect-free interfaces that facilitate efficient charge transfer. In contrast, the high carrier mobility of graphene ensures rapid response and low recombination losses. These factors, when combined, result in stable and consistent operation. This combination of excellent interface quality and fast carrier dynamics makes graphene-based heterostructures especially promising for advanced optoelectronic devices such as wearable sensors, imaging systems, and optical communication systems, which outperform many conventional rigid devices with slower response times and less mechanical flexibility.

Building on advancements in Janus and 2D material-based photodetectors, Ghanbari *et al.*[226] fabricated a geometrically asymmetric p-type 2D molybdenum diselenide (GA-$MoSe_2$)

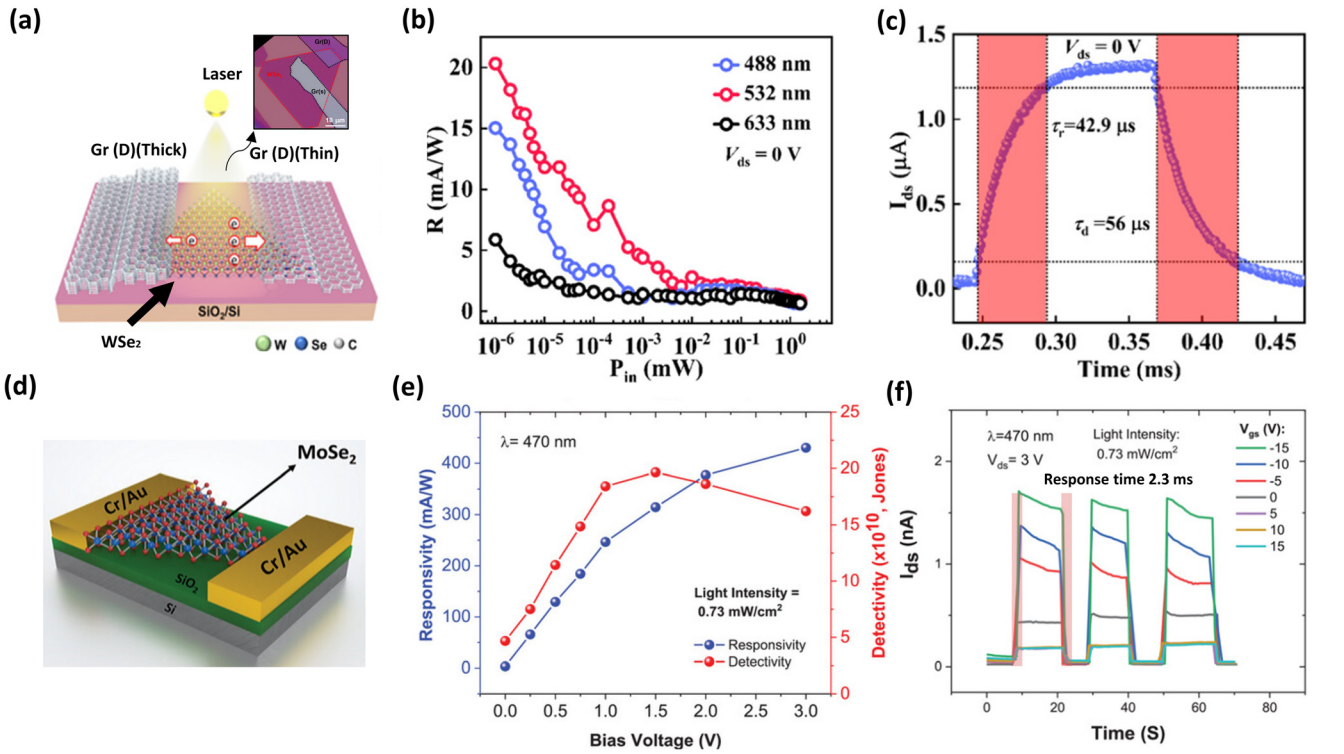

Fig. 17 (a) Schematic of the Gr/WSe2/Gr photodetector. Inset shows the OM image of the Gr/WSe_2/Gr photodetector (red dotted lines and black dotted lines show multilayer WSe_2 and Gr, respectively). (b) *R* under three laser wavelengths (488, 532, and 633 nm) at V_{ds} = 0 V. (c) τ_r and τ_d of the photodetector. (d) Schematic of the GA-$MoSe_2$ photodetector device with drain–source voltage (V_{ds}) and gate–source voltage (V_{gs}). (e) Responsivity (*R*) and detectivity (*D**) of the photodetector at several bias voltages with the same light intensity of 0.73 mW cm^{-2}. (f) *I*–*t* characteristics of the GA-$MoSe_2$ device at a light intensity of 0.73 mW cm^{-2}, V_{ds} = 3 V, and different gate biases of V_{gs} = −15–15 V. This figure has been reproduced from ref. 226 and 227 with permission from Advanced Optical Materials, copyright 2024. ACS Applied Materials & Interfaces, copyright 2023.

photodiode with Cr/Au asymmetric electrodes, as shown in Fig. 17(d). The asymmetric interfaces between $MoSe_2$ and metal layers establish built-in Schottky barriers, improving charge separation and rectification responses. A high rectification ratio of around 10^4 allows this device to perform diode functions while detecting light signals through self-powered photodetection. The photodetector achieved its highest responsivity level at 430 mA W^{-1}, while displaying a detectivity value of 1.96×10^{11} Jones at a bias of 3 V, as illustrated in Fig. 17(e). The application of gate bias resulted in an electrostatic doping effect, which increased the responsivity to 1615 mA W^{-1}. The measured response time reached 2.3 ms, indicating suitability in high-speed optoelectronic applications.

The response of the photocurrent over time occurs under different gate voltages, V_{gs}, for 470 nm illumination, as shown in Fig. 17(f), demonstrating the performance stability of the photodetector across various electrical excitation conditions. The quick response time of 2.3 ms proves its suitability in high-speed optoelectronics applications. The simple fabrication process, high rectification ratio, and strong photoresponse position GA-$MoSe_2$ photodiodes as promising candidates for next-generation self-powered and flexible photodetectors. The built-in electric field at asymmetric Schottky junctions drives effective separation of photogenerated electron–hole pairs, minimizing recombination losses. Moreover, the layered structure of $MoSe_2$, with its intense light absorption and tunable electronic properties, contributes to high sensitivity and stability.

13. Perovskites and their heterostructures for self-powered photodetectors

Perovskite materials and related heterostructures have garnered considerable interest in self-powered photodetection due to their high absorption coefficients, long carrier diffusion lengths, and adjustable bandgaps.[228] Due to their combination of these characteristics, perovskites are suitable for broadband, low-power photodetection.[229,230] By combining perovskites with substances such as metal oxides or 2D TMDCs, heterostructure-based self-powered perovskite photodetectors can enhance carrier separation and reduce recombination loss.[231]

The device exhibits high responsivity, detectivity, and speedy response times, and has been further improved through advances in band engineering and interface optimization. In addition, flexible perovskite-based SPPDs have been developed for wearable and transparent electronics, exhibiting good mechanical strain resistance and a long lifetime under environmental exposure. Perovskite heterostructures are promising next-generation energy-efficient optoelectronic devices built upon these advancements.

13.1 Perovskite-based self-powered photodetectors

Zhao *et al.*[136] developed a self-powered 2D perovskite $Pb_2Nb_3O_{10}$ photodetector with a layered structure, enabling effective charge transport and light absorption. Fig. 18(a) shows the device that consists of a thin $Pb_2Nb_3O_{10}$ flake with strong optical absorption and high carrier mobility. Self-powered operation is possible without any external bias, which is achieved through the rapid separation of charges due to the intrinsic built-in electric field within the material. The transient photoresponse at different wavelengths is shown in Fig. 18(b), exhibiting a rise time of 0.2 ms and a decay time of 1.2 ms, making the device suitable for high-speed optoelectronic applications. Furthermore, Fig. 18(c) shows that the photodetector's responsivity reaches up to 2.8 A W^{-1}, and its detectivity is 1.2×10^{12} Jones. Its broadband detection in the range of 300 to 500 nm is confirmed by the spectral response curve that demonstrates the strong absorption of the device in the range of ultraviolet to visible.

The $Pb_2Nb_3O_{10}$ photodetector is also stable with repeated illumination cycles and durability. Together, high responsivity, rapid response time, and self-powered operation make this device a promising candidate for next-generation UV photodetection, environmental sensing, and optical communication applications. Guo *et al.*[232] fabricated a self-powered UV photodetector based on a 2D perovskite ferroelectric layer for charge separation using its intrinsic electric field. Fig. 18(d) shows the layered perovskite integrated device with an ITO electrode, guaranteeing the strong light absorption and efficient charge transport. Ferroelectric polarization enhances the internal electric field, leading to self-powered operation without any external bias. Strong UV detection at 360 nm, as shown in Fig. 18(e), suggests that efficient carrier separation is observed. As shown in Fig. 18(f), it achieves an ultrahigh responsivity of 891.7 A W^{-1} and a detectivity of 10^{12} Jones, exceeding all other reported wideband photodetectors in terms of sensitivity. The responsivity and detectivity variations over the power density also show that it performs well under various light conditions. This photodetector offers high responsivity, fast response times, and excellent stability by combining the ferroelectric properties and the perovskite structure. The operation of perovskite-based SPPDs fundamentally relies on their intrinsic polarization fields and long carrier diffusion lengths, which enable efficient charge separation without any external bias. In layered perovskites, such as $Pb_2Nb_3O_{10}$, strong absorption and high mobility enhance broadband responsivity. In contrast, ferroelectric perovskites utilize spontaneous polarization to amplify the built-in field, achieving ultrahigh sensitivity. These synergistic mechanisms, coupled with the structural tunability of perovskites, establish them as versatile platforms for scalable, self-powered photodetection across UV-visible ranges with potential for integration into flexible and wearable electronics.

13.2 Perovskite heterostructure-based self-powered photodetectors

SPPDs based on perovskite heterostructures exhibit unique properties including high light absorption, long carrier diffusion lengths, and tunable band gaps. Integration with organic materials, 2D materials, and metal oxides further

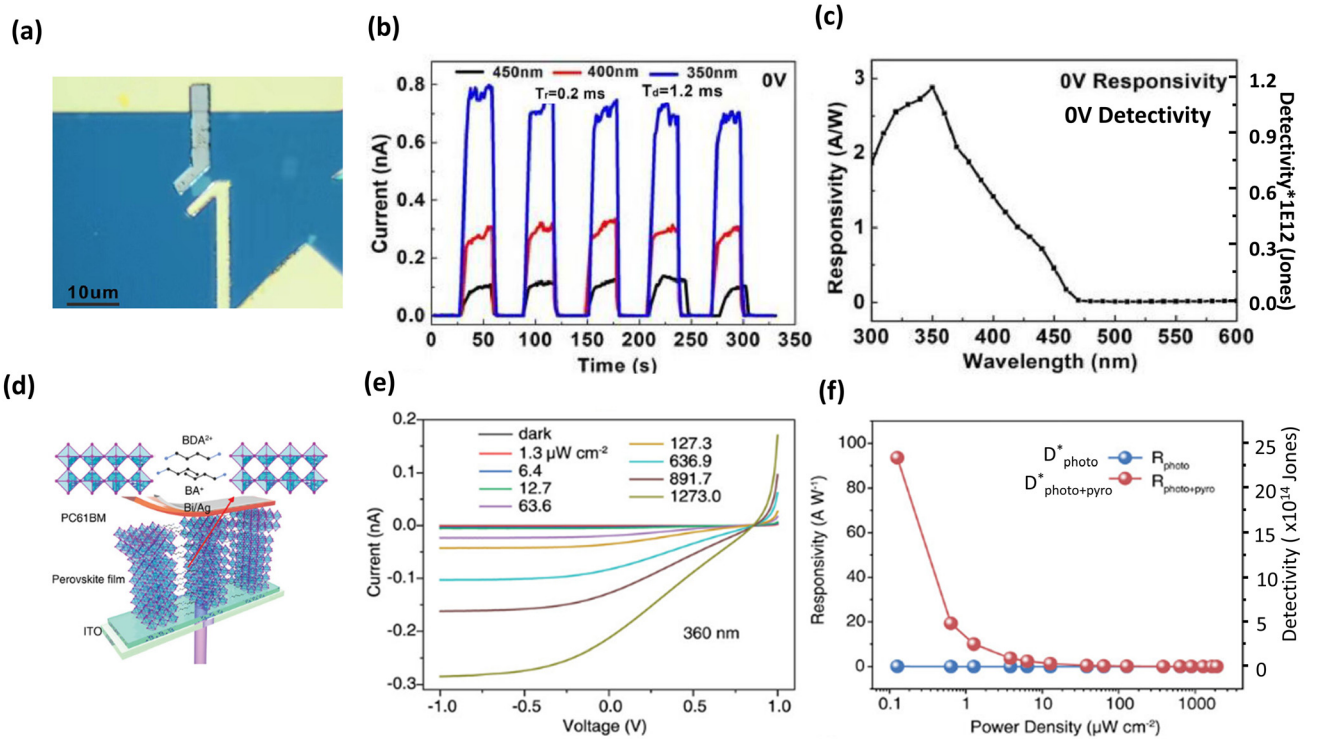

Fig. 18 Photodetection performance of the Au-PNO-Ti device. (a) Optical microscopic photograph of the Au-PNO-Ti device. (b) Photodetection performance of the Au-PNO-Ti device at 350 nm under 0 V. *I*–*t* curves for the device under different light illumination conditions. (c) Responsivity and detectivity for the Au-PNO-Ti device. (d) Schematic showing the device structure. Inset: chemical structure of BA^+ and $BDA2^+$. (e) *I*–*V* characteristics under a 360 nm laser with different power densities ranging from 0 to 1273 μW cm^{-2}. (f) Corresponding detectivities and responsivities of the PD as a function of the power density. This figure has been reproduced from ref. 136 and 232 with permission from the Journal of Materials Science & Technology, copyright 2023. Advanced Materials, copyright 2023.

enhances the carrier separation efficiency by suppressing recombination losses and improving detection sensitivity.[228] Yan *et al.*[233] then reported a large area 2D perovskite oxide/organic heterojunction in a study to realise a self-powered UV photodetector of improved sensitivity and stability. The vertical heterojunction structure was formed by combining the $Ca_2Nb_{2.5}Ta_{0.5}O_{10}$ (CNTO) perovskite oxide nanosheets and PC71BM organic semiconductors, as shown in Fig. 19(a).

Fig. 19(b) illustrates the device, which features a fast rise time of 0.97 ms and a decay time of 8.5 ms. Furthermore, a responsivity of 60 mA W^{-1} at zero bias under 290 nm illumination is also shown for the photodetector in Fig. 19(c). It signifies efficient charge transport through the built-in electric field in the heterojunction. By incorporating the organic layer into the perovskite film, the organic layer filled the pinholes in the perovskite film, suppressing the dark current by 100 000 times and simultaneously improving the charge carrier mobility, resulting in excellent photodetection efficiency. Additionally, this work demonstrates the promise of hybrid perovskite oxide/organic heterojunctions for high-performance, self-powered UV photodetectors in wearable optoelectronics, UV communication, and next-generation sensor devices.

In another study, Gedda *et al.*[138] developed a high-speed, self-powered 2D perovskite photodetector with excellent ambient stability, utilizing planar nanocavity engineering to enhance light absorption and carrier extraction. As depicted in Fig. 19(d), the device featured a multi-layer architecture comprising an ITO electrode, a Ag/Mg interlayer, and a perovskite active layer. The nanocavity structure, which dramatically enhances light confinement, significantly improved the high responsivity and photodetection performance.

Under different conditions, the device's performance was evaluated by measuring the responsivity (*R*) and detectivity (*D**). Due to its higher optical absorption, the photodetector with a cavity structure in Fig. 19(e) exhibits a significantly higher responsivity than that of the device without a cavity structure, particularly in the visible region (~450 nm). An experimental setup image is shown in the inset of the figure for the real-time evaluation of the device's response. It suggests that the photon utilization efficiency can be increased by using a nanocavity integrated into the device structure.

Additionally, Fig. 19(f) displays the time-resolved photocurrent measurements, which feature a fast response time of 30 ns, essential for high-speed photodetection. The spectral response analysis also confirms that the nanocavity design is versatile for increasing responsivity and maintaining consistent responsivity over a wide spectral range. These studies highlight how perovskite heterostructures achieve efficient self-powered photodetection by combining intrinsic material pro-

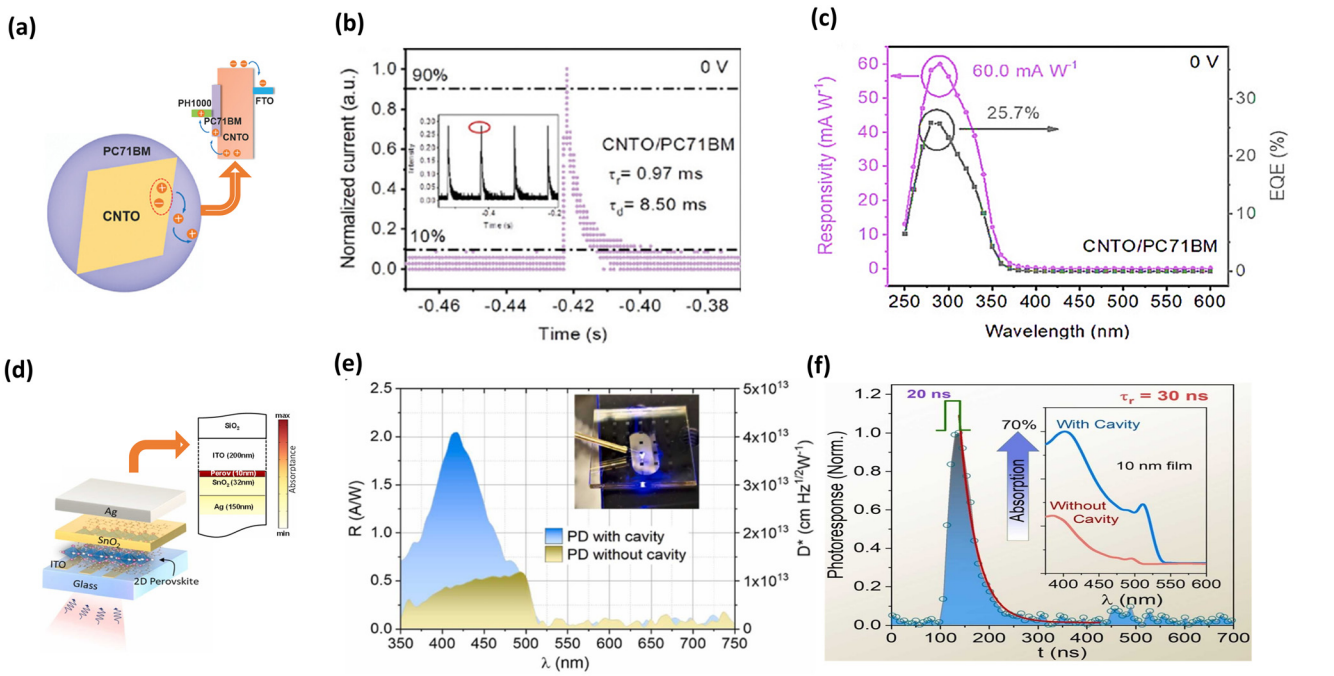

Fig. 19 (a) Schematic of the photodetector charge separation and transportation process based on CNTO/PC71BM. (b) Device's response time at 0 V. (c) Responsivity and EQE of the device at 0 V. The device has the CNTO/PC71BM hybrid as the photosensitive layer. (d) Schematic of the device with the inset showing the absorption distribution of a 10 nm perovskite film with an SnO_2 spacer. (e) Spectral responsivity and specific detectivity of the PD, comparing results with and without the cavity structure. The inset shows the digital photograph of the PD under operation. (f) Time-resolved photoresponse of the 2D perovskite photodetector exhibits a response time of 30 ns. The inset highlights a 70% absorption enhancement with the nanocavity structure. This figure has been reproduced from ref. 86 and 233 with permission from Materials Science and Engineering: R: Reports, copyright 2025. Advanced Functional Materials, copyright 2024.

perties with structural engineering. In CNTO/PC71BM devices, the built-in electric field at the oxide–organic interface promotes charge separation while the organic layer suppresses dark current and enhances mobility. In nanocavity-engineered perovskites, light confinement maximizes photon absorption and accelerates carrier extraction, enabling ultrafast response. Together, these mechanisms demonstrate that hybrid and engineered perovskite heterostructures can couple high sensitivity with speed and stability, positioning them as leading candidates for next-generation self-powered optoelectronics.

14. Challenges, solutions, and future perspectives

SPPDs offer significant advantages in optoelectronics, primarily due to their energy efficiency, adaptability, and capability for integration into low-power applications such as wearable electronics and optical communication systems. Nonetheless, numerous significant challenges hinder the wide-ranging applications of these devices. A key concern is the stability of materials used in perovskite-based and flexible photodetectors. Perovskite materials exhibit great potential due to their high absorption coefficients and adjustable band gaps; however, they are highly susceptible to environmental conditions such as moisture and oxygen, leading to degradation over time. Flexible SPPDs, commonly used in wearable devices, encounter issues related to mechanical stability, as the materials employed must endure repeated deformation while maintaining performance integrity. To address these stability challenges, it is crucial to explore new encapsulation methods, develop more stable material formulations, and innovate in flexible electronics that ensure long-term reliability in practical applications.

Alongside material stability, the effectiveness of charge transport in SPPDs remains a challenge. Defects at material interfaces can considerably impair the performance of these devices, resulting in elevated dark currents and poor charge separation. To address this challenge, investigations have focused on the application of 2D materials such as graphenes, TMDCs, and MXenes, which offer high charge mobility and transparency, thereby facilitating more efficient photodetection. These materials have the potential to create heterostructures that facilitate charge separation, minimise recombination, and boost the overall performance of the device. Moreover, the incorporation of Janus materials, characterized by their asymmetric properties, has demonstrated potential in advancing self-powered devices that exhibit improved polarization sensitivity. Furthermore, the scalability of SPPDs continues to pose a significant challenge, as existing fabrication techniques for 2D materials are currently limited to small-area production. Innovations in scalable fabrication methods, such

as roll-to-roll processing, combined with hybrid strategies that integrate conventional semiconductor fabrication with new 2D materials, may offer a solution to this challenge.

In the future, SPPDs will be integrated into next-generation optoelectronic systems due to their advancements in device engineering, fabrication methods, and materials science. Utilizing machine learning (ML) and artificial intelligence (AI) holds great promise for accelerating the discovery of new materials and enhancing the device performance. The implementation of these technologies can enhance the design of innovative heterostructures, inform material choices, and improve fabrication methods, ultimately leading to more efficient and resilient SPPDs. Moreover, incorporating SPPDs into wireless sensor networks (WSNs) and the Internet of Things (IoT) presents novel opportunities for real-time sensing, environmental monitoring, and health diagnostics. Self-powered devices such as SPPDs have the potential to reduce dependence on external power sources, making them excellent candidates for use in remote sensing and portable systems.[234] The integration of flexible substrates, improved material characteristics, and self-sufficient functionality will allow SPPDs to play a crucial role in wearable electronics and biomedical devices, leading to advancements in sustainable and energy-efficient optoelectronic systems.

15. Conclusion

Self-powered photodetectors (SPPDs) hold the promise of transforming next-generation optoelectronics by providing energy-efficient, high-performance devices suitable for various applications including wearable electronics and optical communication. Despite considerable progress in materials and device engineering, challenges such as material stability, environmental degradation, fabrication scalability, and charge transport efficiency still need to be addressed to unlock their full potential. The incorporation of cutting-edge materials such as 2D materials, perovskites, MXenes, and Janus heterostructures demonstrates potential for improving the device performance; however, additional optimization is required to overcome current challenges related to response time and dark current. The ongoing advancement of scalable fabrication methods, along with breakthroughs in interface engineering and material design, will be crucial for the broad commercialization of SPPDs. Anticipating future developments, the integration of self-powered photodetectors into wireless sensor networks, IoT devices, and biomedical applications presents interesting opportunities for real-time sensing and energy harvesting systems, setting the stage for sustainable, next-generation optoelectronic devices.

Conflicts of interest

The authors declare that they have no known competing financial interests or personal relationships that could have appeared to influence the work reported in this paper.

Data availability

No new data were generated or analyzed in this study. All data referenced in this review are available from the cited literature.

Acknowledgements

The authors acknowledge the assistance provided by the Advanced Multiscale Materials for Key Enabling Technologies project, supported by the Ministry of Education, Youth, and Sports of the Czech Republic. Project No. CZ.02.01.01/00/22_008/0004558, co-funded by the European Union. Z.S. was supported by the project Advanced Functional Nanorobots (reg. No. CZ.02.1.01/0.0/0.0/15_003/0000444 financed by the EFRR). This work was supported by project LUAUS25268 from Ministry of Education Youth and Sports (MEYS).

References

1 L. Guo, J. Han and J. Wang, Recent advances in enhancing the photodetector performance of 2D materials by combining them with organic thin films, *J. Mater. Chem. C*, 2024, **12**(4), 1233–1267.
2 C. Zhang, *et al.*, Wavelength-tunable broadband lasers based on nanomaterials, *Nanotechnology*, 2023, **34**(49), 492001.
3 S. Watson, *et al.*, Resonant tunneling diode photodetectors for optical communications, *Microw. Opt. Technol. Lett.*, 2019, **61**(4), 1121–1125.
4 P. Grant, *et al.*, Terahertz free space communications demonstration with quantum cascade laser and quantum well photodetector, *Electron. Lett.*, 2009, **45**(18), 952–954.
5 Y. Zhou, *et al.*, Halide-exchanged perovskite photodetectors for wearable visible-blind ultraviolet monitoring, *Nano Energy*, 2022, **100**, 107516.
6 J. Zha, *et al.*, Infrared photodetectors based on 2D materials and nanophotonics, *Adv. Funct. Mater.*, 2022, **32**(15), 2111970.
7 P. Büchele, *et al.*, X-ray imaging with scintillator-sensitized hybrid organic photodetectors, *Nat. Photonics*, 2015, **9**(12), 843–848.
8 W. W. Moses, Photodetectors for nuclear medical imaging, *Nucl. Instrum. Methods Phys. Res., Sect. A*, 2009, **610**(1), 11–15.
9 B. Radisavljevic, *et al.*, Single-layer MoS2 transistors, *Nat. Nanotechnol.*, 2011, **6**(3), 147–150.
10 G. Haider, *et al.*, Electrical–polarization–induced ultrahigh responsivity photodetectors based on graphene and graphene quantum dots, *Adv. Funct. Mater.*, 2016, **26**(4), 620–628.
11 J. Wang, *et al.*, Highly polarized photoluminescence and photodetection from single indium phosphide nanowires, *Science*, 2001, **293**(5534), 1455–1457.
12 E. Zhang, *et al.*, Tunable ambipolar polarization-sensitive photodetectors based on high-anisotropy ReSe2 nanosheets, *ACS Nano*, 2016, **10**(8), 8067–8077.

13 Y. Dai, *et al.*, Self–powered Si/CdS flexible photodetector with broadband response from 325 to 1550 nm based on pyro–phototronic effect: an approach for photosensing below bandgap energy, *Adv. Mater.*, 2018, **30**(9), 1705893.
14 S. F. Leung, *et al.*, A self–powered and flexible organometallic halide perovskite photodetector with very high detectivity, *Adv. Mater.*, 2018, **30**(8), 1704611.
15 L. B. Luo, *et al.*, Near–infrared light photovoltaic detector based on GaAs nanocone array/monolayer graphene schottky junction, *Adv. Funct. Mater.*, 2014, **24**(19), 2794–2800.
16 P. Feng, *et al.*, A high-performance self-powered photodetector based on WSe 2–graphene–MoTe 2 van der Waals heterojunctions, *J. Mater. Chem. C*, 2022, **10**(24), 9401–9406.
17 J. Ajayan, *et al.*, A review of photovoltaic performance of organic/inorganic solar cells for future renewable and sustainable energy technologies, *Superlattices Microstruct.*, 2020, **143**, 106549.
18 F. Koppens, *et al.*, Photodetectors based on graphene, other two-dimensional materials and hybrid systems, *Nat. Nanotechnol.*, 2014, **9**(10), 780–793.
19 Q. H. Wang, *et al.*, Electronics and optoelectronics of two-dimensional transition metal dichalcogenides, *Nat. Nanotechnol.*, 2012, **7**(11), 699–712.
20 K. Shavanova, *et al.*, Application of 2D non-graphene materials and 2D oxide nanostructures for biosensing technology, *Sensors*, 2016, **16**(2), 223.
21 A. Gupta, T. Sakthivel and S. Seal, Recent development in 2D materials beyond graphene, *Prog. Mater. Sci.*, 2015, **73**, 44–126.
22 C. Ortiz-Cervantes, P. Carmona-Monroy and D. Solis-Ibarra, Two–dimensional halide perovskites in solar cells: 2D or not 2D?, *ChemSusChem*, 2019, **12**(8), 1560–1575.
23 Z. Zhou, *et al.*, Field–effect transistors based on 2D organic semiconductors developed by a hybrid deposition method, *Adv. Sci.*, 2019, **6**(19), 1900775.
24 G. P. Neupane, *et al.*, 2D organic semiconductors, the future of green nanotechnology, *Nano Mater. Sci.*, 2019, **1**(4), 246–259.
25 M. Abubakr, *et al.*, Innovations in self-powered nanophotonics of emerging and flexible two-dimensional materials, *Mater. Today Phys.*, 2023, **39**, 101285.
26 O. Lopez-Sanchez, *et al.*, Ultrasensitive photodetectors based on monolayer MoS2, *Nat. Nanotechnol.*, 2013, **8**(7), 497–501.
27 R. Kumar, *et al.*, Recent advances in the synthesis and modification of carbon-based 2D materials for application in energy conversion and storage, *Prog. Energy Combust. Sci.*, 2018, **67**, 115–157.
28 K. Chen, *et al.*, Graphene photonic crystal fibre with strong and tunable light–matter interaction, *Nat. Photonics*, 2019, **13**(11), 754–759.
29 K.-J. Tielrooij, *et al.*, Generation of photovoltage in graphene on a femtosecond timescale through efficient carrier heating, *Nat. Nanotechnol.*, 2015, **10**(5), 437–443.
30 H. Zeng, *et al.*, Valley polarization in MoS2 monolayers by optical pumping, *Nat. Nanotechnol.*, 2012, **7**(8), 490–493.
31 M. F. Khan, *et al.*, Electrical and photo-electrical properties of MoS2 nanosheets with and without an Al_2O_3 capping layer under various environmental conditions, *Sci. Technol. Adv. Mater.*, 2016, **17**(1), 166–176.
32 C. Qin, *et al.*, Atomic–layered MoS2 as a tunable optical platform, *Adv. Opt. Mater.*, 2016, **4**(10), 1429–1456.
33 Q. Yue, *et al.*, Mechanical and electronic properties of monolayer MoS2 under elastic strain, *Phys. Lett. A*, 2012, **376**(12–13), 1166–1170.
34 A. K. Geim and I. V. Grigorieva, van der Waals heterostructures, *Nature*, 2013, **499**(7459), 419–425.
35 P. Wu, *et al.*, Next-generation machine vision systems incorporating two-dimensional materials: Progress and perspectives, *InfoMat*, 2022, **4**(1), e12275.
36 F. Xia, *et al.*, Two-dimensional material nanophotonics, *Nat. Photonics*, 2014, **8**(12), 899–907.
37 F. Wang, *et al.*, 2D library beyond graphene and transition metal dichalcogenides: a focus on photodetection, *Chem. Soc. Rev.*, 2018, **47**(16), 6296–6341.
38 X. Wang, *et al.*, Ultrasensitive and broadband MoS2 photodetector driven by ferroelectrics, *Adv. Mater.*, 2015, **27**(42), 6575–6581.
39 X. Li, *et al.*, Graphene and related two-dimensional materials: Structure-property relationships for electronics and optoelectronics, *Appl. Phys. Rev.*, 2017, **4**(2), 021306-2–021306-25.
40 A. Splendiani, *et al.*, Emerging photoluminescence in monolayer MoS2, *Nano Lett.*, 2010, **10**(4), 1271–1275.
41 D. Xiao, *et al.*, Coupled spin and valley physics in monolayers of MoS2 and other group-VI dichalcogenides, *Phys. Rev. Lett.*, 2012, **108**(19), 196802.
42 Y. Wang, *et al.*, Electrochemical control of photoluminescence in two-dimensional MoS2 nanoflakes, *ACS Nano*, 2013, **7**(11), 10083–10093.
43 S. Gopalan, *et al.*, Theoretical study of electronic transport in two-dimensional transition metal dichalcogenides: Effects of the dielectric environment, *Phys. Rev. Appl.*, 2022, **18**(5), 054062.
44 K. F. Mak, *et al.*, Atomically thin MoS 2: a new direct-gap semiconductor, *Phys. Rev. Lett.*, 2010, **105**(13), 136805.
45 R. Coehoorn, C. Haas and R. De Groot, Electronic structure of MoSe2, MoS2, and WSe 2. II. The nature of the optical band gaps, *Phys. Rev. B:Condens. Matter Mater. Phys.*, 1987, **35**(12), 6203.
46 A. Beal and H. Hughes, Kramers-Kronig analysis of the reflectivity spectra of 2H-MoS2, 2H-MoSe2 and 2H-MoTe2, *J. Phys. C:Solid State Phys.*, 1979, **12**(5), 881.
47 P. J. Ko, *et al.*, High-performance near-infrared photodetector based on nano-layered MoSe2, *Semicond. Sci. Technol.*, 2017, **32**(6), 065015.
48 G. Eda and S. A. Maier, Two-dimensional crystals: managing light for optoelectronics, *ACS Nano*, 2013, **7**(7), 5660–5665.
49 M. Bernardi, M. Palummo and J. C. Grossman, Extraordinary sunlight absorption and one nanometer

thick photovoltaics using two-dimensional monolayer materials, *Nano Lett.*, 2013, **13**(8), 3664–3670.
50 L. Li, *et al.*, MXene/AlGaN van der Waals heterojunction self-powered photodetectors for deep ultraviolet communication, *Appl. Phys. Lett.*, 2024, **124**(13), 132105-1–132105-7.
51 A. Morita, Semiconducting black phosphorus, *Appl. Phys. A*, 1986, **39**, 227–242.
52 M. Long, *et al.*, Broadband photovoltaic detectors based on an atomically thin heterostructure, *Nano Lett.*, 2016, **16**(4), 2254–2259.
53 W. Zhu, *et al.*, Flexible black phosphorus ambipolar transistors, circuits and AM demodulator, *Nano Lett.*, 2015, **15**(3), 1883–1890.
54 H. Yuan, *et al.*, Polarization-sensitive broadband photodetector using a black phosphorus vertical p–n junction, *Nat. Nanotechnol.*, 2015, **10**(8), 707–713.
55 J. Li, *et al.*, High-performance, self-powered photodetectors based on perovskite and graphene, *ACS Appl. Mater. Interfaces*, 2017, **9**(49), 42779–42787.
56 K. Lu, *et al.*, Solution-processed electronics for artificial synapses, *Mater. Horiz.*, 2021, **8**(2), 447–470.
57 R. Ding, *et al.*, Effective piezo–phototronic enhancement of flexible photodetectors based on 2D hybrid perovskite ferroelectric single–crystalline thin–films, *Adv. Mater.*, 2021, **33**(32), 2101263.
58 L. Zhang, *et al.*, Recent advances in emerging Janus two-dimensional materials: from fundamental physics to device applications, *J. Mater. Chem. A*, 2020, **8**(18), 8813–8830.
59 Z. Ma, *et al.*, Recent progress in group-III metal chalcogenide based Janus materials: from properties to potential applications, *J. Mater. Chem. C*, 2023, **11**(47), 16439–16451.
60 S. J. Liang, *et al.*, van der Waals heterostructures for high–performance device applications: challenges and opportunities, *Adv. Mater.*, 2020, **32**(27), 1903800.
61 Y. Liu, Y. Huang and X. Duan, van der Waals integration before and beyond two-dimensional materials, *Nature*, 2019, **567**(7748), 323–333.
62 D. Zhong, *et al.*, van der Waals engineering of ferromagnetic semiconductor heterostructures for spin and valleytronics, *Sci. Adv.*, 2017, **3**(5), e1603113.
63 D. Ballarini, *et al.*, All-optical polariton transistor, *Nat. Commun.*, 2013, **4**(1), 1778.
64 T. Qi, *et al.*, Interlayer transition in a vdW heterostructure toward ultrahigh detectivity shortwave infrared photodetectors, *Adv. Funct. Mater.*, 2020, **30**(3), 1905687.
65 Y. Tang, *et al.*, Distinctive interfacial charge behavior and versatile photoresponse performance in isotropic/anisotropic WS2/ReS2 heterojunctions, *ACS Appl. Mater. Interfaces*, 2020, **12**(47), 53475–53483.
66 C. Choi, *et al.*, Enhanced interlayer neutral excitons and trions in trilayer van der Waals heterostructures, *npj 2D Mater. Appl.*, 2018, **2**(1), 30.
67 C. Du, *et al.*, High responsivity and broadband polarized photodetectors based on InSe/ReSe2 van der Waals heterostructures, *J. Alloys Compd.*, 2022, **919**, 165586.
68 J. Qiao, *et al.*, Ultrasensitive and broadband all–optically controlled THz modulator based on MoTe2/Si van der Waals heterostructure, *Adv. Opt. Mater.*, 2020, **8**(17), 2000160.
69 J. Chen, *et al.*, Recent progress of heterojunction ultraviolet photodetectors: materials, integrations, and applications, *Adv. Funct. Mater.*, 2020, **30**(16), 1909909.
70 T. Tan, *et al.*, 2D material optoelectronics for information functional device applications: status and challenges, *Adv. Sci.*, 2020, **7**(11), 2000058.
71 Z. Zhang, *et al.*, Graphene–based mixed–dimensional van der Waals heterostructures for advanced optoelectronics, *Adv. Mater.*, 2019, **31**(37), 1806411.
72 Z. Yang and J. Hao, Recent progress in 2D layered III–VI semiconductors and their heterostructures for optoelectronic device applications, *Adv. Mater. Technol.*, 2019, **4**(8), 1900108.
73 X. Duan, *et al.*, Two-dimensional transition metal dichalcogenides as atomically thin semiconductors: opportunities and challenges, *Chem. Soc. Rev.*, 2015, **44**(24), 8859–8876.
74 V. K. Sangwan and M. C. Hersam, Neuromorphic nanoelectronic materials, *Nat. Nanotechnol.*, 2020, **15**(7), 517–528.
75 D. Jariwala, *et al.*, Emerging device applications for semiconducting two-dimensional transition metal dichalcogenides, *ACS Nano*, 2014, **8**(2), 1102–1120.
76 X. T. Liu, *et al.*, Building functional memories and logic circuits with 2D boron nitride, *Adv. Funct. Mater.*, 2021, **31**(4), 2004733.
77 J. Miao, *et al.*, 2D heterostructures for advanced logic and memory devices, in 2D Materials for Electronics, in *Sensors and Devices*, Elsevier, 2023, pp. 141–167.
78 T. Zhai, *et al.*, One-dimensional inorganic nanostructures: synthesis, field-emission and photodetection, *Chem. Soc. Rev.*, 2011, **40**(5), 2986–3004.
79 K. Deng and L. Li, CdS nanoscale photodetectors, *Adv. Mater.*, 2014, **26**(17), 2619–2635.
80 U. Otuonye, H. W. Kim and W. D. Lu, Ge nanowire photodetector with high photoconductive gain epitaxially integrated on Si substrate, *Appl. Phys. Lett.*, 2017, **110**(17), 173104-1–173104-5.
81 Q. Wang, *et al.*, Oriented Growth of Pb1-x Snx Te Nanowire Arrays for Integration of Flexible Infrared Detectors, *Adv. Mater.*, 2016, **28**(18), 3596–3601.
82 W. Huang, *et al.*, Enhanced photodetection properties of tellurium@ selenium roll–to–roll nanotube heterojunctions, *Small*, 2019, **15**(23), 1900902.
83 Y. Zi, *et al.*, Recent progress in interface engineering of nanostructures for photoelectrochemical energy harvesting applications, *Small*, 2023, **19**(19), 2208274.
84 R. Kumar, *et al.*, Self-powered broadband ultraviolet photodetector based on MoSe2/n-GaN heterojunction, *J. Alloys Compd.*, 2025, **1014**, 178813.
85 S. Soleimani-Amiri, S. G. Rudi and N. Ghobadi, Janus MoXYCl (X= S, Se, Te; Y= N, P, As) monolayers: a promising family of 2D materials for high-performance p–i–n

photodetectors and spintronic applications, *Nanoscale*, 2025, **17**, 16748–16766.
86 M. Gedda, *et al.*, High-speed, self-powered 2D-perovskite photodetectors with exceptional ambient stability enabled by planar nanocavity engineering, *Mater. Sci. Eng., R*, 2025, **162**, 100885.
87 J. Li, *et al.*, High-Performance, Self-Powered Photodetectors Based on Perovskite and Graphene, *ACS Appl. Mater. Interfaces*, 2017, **9**(49), 42779–42787.
88 F. Bai, *et al.*, A High-Performance Self-Powered Photodetector Based on Monolayer MoS2/Perovskite Heterostructures, *Adv. Mater. Interfaces*, 2018, **5**(6), 1701275.
89 D. Wu, *et al.*, Highly Polarization-Sensitive, Broadband, Self-Powered Photodetector Based on Graphene/PdSe2/Germanium Heterojunction, *ACS Nano*, 2019, **13**(9), 9907–9917.
90 H. Shang, *et al.*, A mixed-dimensional 1D Se–2D InSe van der Waals heterojunction for high responsivity self-powered photodetectors, *Nanoscale Horiz.*, 2020, **5**(3), 564–572.
91 L. Han, *et al.*, A high performance self-powered photodetector based on a 1D Te–2D WS 2 mixed-dimensional heterostructure, *Nanoscale Adv.*, 2021, **3**(9), 2657–2665.
92 D. Wu, *et al.*, Wafer-scale synthesis of wide bandgap 2D GeSe2 layers for self-powered ultrasensitive UV photodetection and imaging, *Nano Energy*, 2022, **104**, 107972.
93 C. Li, *et al.*, Self–powered photodetector with high performance based on all–2D NbSe2/MoSe2 van der Waals heterostructure, *Adv. Opt. Mater.*, 2023, **11**(22), 2300905.
94 X. Wang, *et al.*, Air-stable self-powered photodetector based on TaSe2/WS2/TaSe2 asymmetric heterojunction with surface self-passivation, *J. Colloid Interface Sci.*, 2024, **657**, 529–537.
95 P. Yu, *et al.*, A 2D Te/Mxene Schottky junction for a self-powered broadband photodetector with high polarization-sensitive imaging, *J. Mater. Chem. C*, 2025, **13**(9), 4642–4650.
96 F. Withers, *et al.*, All-graphene photodetectors, *ACS Nano*, 2013, **7**(6), 5052–5057.
97 C.-H. Liu, *et al.*, Graphene photodetectors with ultra-broadband and high responsivity at room temperature, *Nat. Nanotechnol.*, 2014, **9**(4), 273–278.
98 B. H. Lee, *et al.*, Graphene-Conducting Polymer Hybrid Transparent Electrodes for Efficient Organic Optoelectronic Devices, *Adv. Funct. Mater.*, 2014, **24**(13), 1847–1856.
99 Y. Beckmann, *et al.*, Self-Powered Photodetectors Based on Scalable MOCVD-Grown WS2−MoS2 Heterostructures, *ACS Photonics*, 2024, **11**(6), 2228–2235.
100 S. Ahn, *et al.*, A 2D Titanium Carbide MXene Flexible Electrode for High-Efficiency Light-Emitting Diodes, *Adv. Mater.*, 2020, **32**(23), e2000919.
101 C. Liu, *et al.*, Anomalous photovoltaics in Janus MoSSe monolayers, *Nat. Commun.*, 2025, **16**(1), 544.
102 R. A. Afre and D. Pugliese, Perovskite Solar Cells: A Review of the Latest Advances in Materials, Fabrication Techniques, and Stability Enhancement Strategies, *Micromachines*, 2024, **15**(2), 192.
103 X. Fan, *et al.*, PEDOT:PSS materials for optoelectronics, thermoelectrics, and flexible and stretchable electronics, *J. Mater. Chem. A*, 2023, **11**(35), 18561–18591.
104 Y. Zhao, *et al.*, Improvement of the Optoelectrical Properties of a Transparent Conductive Polymer via a Simple Mechanical Pressure Treatment, *ACS Omega*, 2020, **5**(13), 7545–7554.
105 S. He, *et al.*, All-2D asymmetric self-powered photodetectors with ultra-fast photoresponse based on Gr/WSe2/NbSe2 van der Waals heterostructure, *J. Mater. Sci. Technol.*, 2025, **219**, 205–212.
106 D. H. Shin and H. Lee, Graphene/WS2/LaVO3 heterojunction for self-powered, high-speed, and broadband photodetectors, *Curr. Appl. Phys.*, 2025, **70**, 69–75.
107 Y. Zhang and X. He, WS2/Graphene/MoS2 Sandwich van der Waals Heterojunction for Fast-Response Photodetectors, *ACS Appl. Mater. Interfaces*, 2025, **17**(1), 1826–1833.
108 Y. Zhang and X. He, Self-powered photodetector with GeSe/WS2/MoS2 van der Waals heterojunction, *Sens. Actuators, A*, 2025, **381**, 116080.
109 D. Yang, *et al.*, Vis-infrared wide-band and self-powered photodetectors base on CuI/MoS2 van der Waals heterostructure, *J. Mol. Struct.*, 2025, **1323**, 140773.
110 H. F. Rouhi, *et al.*, Highly Air-Stable and Sensitive Self-Powered Broadband Photodetector Based on a PVA–MoS2 Fibers/n-Si Heterojunction, *ACS Appl. Electron. Mater.*, 2025, **7**(2), 757–765.
111 X. Huang, *et al.*, In-Plane Bulk Photovoltaic Effect in a MoSe2/NbOI2 Heterojunction for Efficient Polarization-Sensitive Self-Powered Photodetection, *Nano Lett.*, 2025, **25**(4), 1495–1503.
112 R. Wang, *et al.*, High performance n-MoSe2/p-Ge-GeSn MQW/n-Ge heterojunction phototransistor for extended short-wave infrared photodetection, *J. Phys. D: Appl. Phys.*, 2025, **58**(10), 105107.
113 H. Li and Z. Yang, Highly Responsive and Self-Powered Photodetector Based on PtSe2/MoS2 Heterostructure, *Molecules*, 2024, **29**(11), 2553.
114 K. Li, *et al.*, High-Performance Self-Powered Photodetectors Based on the MnS/MoS2 Heterojunction with Smooth Interfacial Band Bending, *J. Phys. Chem. C*, 2024, **128**(51), 21730–21738.
115 A. Yadav, *et al.*, Plasmonics Stimulated Enhanced Performance MoS2/WO3 Heterojunction Based Broadband Self-Powered Photodetector, *ACS Appl. Opt. Mater.*, 2024, **2**(5), 784–794.
116 P. Yu, *et al.*, 2D Te/Mxene Schottky Junction for Self-Powered Broadband Photodetector With High Polarization-Sensitive Imaging, *J. Mater. Chem. C*, 2025, **13**, 4642–4650.
117 M. Mao, *et al.*, Dual strategy of interface and absorber modifications via Ti3C2Tx MXene for high-performance self-powered CsPbCl3 UV photodetectors, *J. Alloys Compd.*, 2025, **1010**, 178092.

118 H. Ma, *et al.*, Transmittance contrast–induced photocurrent: A general strategy for self–powered photodetectors based on MXene electrodes, *InfoMat*, 2024, **6**(5), e12540.
119 S. Zhou, *et al.*, High–Performance Self–Powered PEC Photodetectors Based on 2D BiVO4/MXene Schottky Junction, *Adv. Funct. Mater.*, 2025, **35**, 2416922.
120 L. Luo, *et al.*, MXene-GaN van der Waals metal-semiconductor junctions for high performance multiple quantum well photodetectors, *Light: Sci. Appl.*, 2021, **10**(1), 177.
121 L. Jian, *et al.*, WS2 lateral p–n homojunction toward a sensitive self-driven photodetector by water treatment, *Appl. Phys. Lett.*, 2024, **124**(9), 093506-1–093506-6.
122 Y. Wang and P. Hou, Ferroelectric polarization-modulated two-dimensional homojunctions for enhanced nonvolatile multistate memory with self-powered optical readout capacity, *J. Mater. Chem. C*, 2025, **13**, 3430–3438.
123 C. Zhang, *et al.*, Broadband self-powered MoS2/PdSe2/WSe2 PSN heterojunction photodetector for high-performance optical imaging and communication, *Opt. Express*, 2024, **32**(22), 38136–38146.
124 Y. Han, *et al.*, Vertical heterojunction photodetector with self-powered broadband response and high performance, *Chem. Eng. J.*, 2023, **477**, 147060.
125 C. Yan, *et al.*, High performance self-powered photodetector based on van der Waals heterojunction, *Nanotechnology*, 2023, **35**(3), 035203.
126 M. Che, *et al.*, PdSe2/2H–MoTe2 Heterojunction Self-Powered Photodetector: Broadband Photodetection and Linear/Circular Polarization Capability, *ACS Nano*, 2024, **18**(44), 30884–30895.
127 J. Panda, *et al.*, Polarization-Resolved Position-Sensitive Self-Powered Binary Photodetection in Multilayer Janus CrSBr, *ACS Appl. Mater. Interfaces*, 2023, **16**(1), 1033–1043.
128 T. Zheng, *et al.*, Self-powered photodetector with high efficiency and polarization sensitivity enabled by WSe2/Ta2NiSe5/WSe2 van der Waals dual heterojunction, *ACS Appl. Mater. Interfaces*, 2023, **15**(24), 29363–29374.
129 S. Maity and P. Kumar, A synergistic heterojunction of SnS2/SnSSe nanosheets on GaN for advanced self-powered photodetectors, *Nanoscale Horiz.*, 2024, **9**(8), 1318–1329.
130 S. Yang, *et al.*, High-performance flexible photodetectors based on CdTe/MoS2 heterojunction, *Nanoscale*, 2024, **16**(29), 13932–13937.
131 C. W. Jang and S.-H. Choi, Self-powered semitransparent/flexible doped-graphene/WS2 vertical-heterostructure photodetectors, *J. Alloys Compd.*, 2022, **901**, 163685.
132 U. Varshney, *et al.*, Revealing the photo-sensing capabilities of a super-flexible, paper-based wearable a-Ga2O3 self-driven ultra-high-performance solar-blind photodetector, *Chem. Eng. J.*, 2024, **496**, 153910.
133 M. Dai, *et al.*, High Performance Self-Driven Photodetectors Based on MoS2 Schottky Barrier Diode, *Adv. Opt. Mater.*, 2024, **12**(9), 2301900.
134 J. Wang, *et al.*, PtSe2/InP Mixed-Dimensional Schottky Junction for High-Performance Self-Powered Near-Infrared Photodetection, *Adv. Opt. Mater.*, 2024, **12**(29), 2401035.
135 X. Zhang, D. Qiu and P. Hou, Enhanced self-powered metal–semiconductor–metal WSe2 photodetectors with asymmetric Schottky contacts through tailored electrode thickness and positioning, *Appl. Phys. Lett.*, 2024, **124**(22), 222105-1–222105-7.
136 Y. Zhang, *et al.*, Two-dimensional perovskite Pb2Nb3O10 photodetectors, *J. Mater. Sci. Technol.*, 2023, **164**, 95–101.
137 L. Guo, *et al.*, A Self-Powered UV Photodetector With Ultrahigh Responsivity Based on 2D Perovskite Ferroelectric Films With Mixed Spacer Cations, *Adv. Mater.*, 2023, **35**(47), 2301705.
138 M. Gedda, *et al.*, High-speed, self-powered 2D-perovskite photodetectors with exceptional ambient stability enabled by planar nanocavity engineering, *Mater. Sci. Eng., R*, 2025, **162**, 100885.
139 E. Gao, *et al.*, Mechanical exfoliation of two-dimensional materials, *J. Mech. Phys. Solids*, 2018, **115**, 248–262.
140 B. Qin, *et al.*, Substrates in the Synthesis of Two-Dimensional Materials via Chemical Vapor Deposition, *Chem. Mater.*, 2020, **32**(24), 10321–10347.
141 S. Chaudhary, S. K. Gupta and C. M. Singh Negi, Enhanced performance of perovskite photodetectors fabricated by two-step spin coating approach, *Mater. Sci. Semicond. Process.*, 2020, **109**, 104916.
142 R. Bian, *et al.*, Ultralight MXene-based aerogels with high electromagnetic interference shielding performance, *J. Mater. Chem. C*, 2019, **7**(3), 474–478.
143 T. M. H. Nguyen, *et al.*, Recent advances in self-powered and flexible UVC photodetectors, *Exploration*, 2022, **2**(5), 20210078.
144 P. Zhang, *et al.*, Progress in 2D Material-Based Infrared Photodetectors for Intelligent Vision Applications, *Adv. Funct. Mater.*, 2025, **35**, 2502072.
145 J. Xu, *et al.*, Recent Progress of Self-Powered Optoelectronic Devices Based on 2D Materials, *Processes*, 2024, **12**(8), 1728.
146 G. Li, *et al.*, Research Progress of High-Sensitivity Perovskite Photodetectors: A Review of Photodetectors: Noise, Structure, and Materials, *ACS Appl. Electron. Mater.*, 2022, **4**(4), 1485–1505.
147 X. Tang, *et al.*, High-performance, self-powered flexible MoS2 photodetectors with asymmetric van der Waals gaps, *Phys. Chem. Chem. Phys.*, 2022, **24**(12), 7323–7330.
148 A. Kumar, *et al.*, Self-Powered Broadband Photodetectors Based on WS2-Anchored MoS2 with Enhanced Responsivity and Detectivity, *Small*, 2025, **21**(20), 2502900.
149 Y. Li, *et al.*, Highly Sensitive Photodetectors Based on Monolayer MoS2 Field-Effect Transistors, *ACS Omega*, 2022, **7**(16), 13615–13621.
150 W. Dong, *et al.*, Toward Clean 2D Materials and Devices: Recent Progress in Transfer and Cleaning Methods, *Adv. Mater.*, 2024, **36**(22), 2303014.

151 M. Chhowalla, *et al.*, The chemistry of two-dimensional layered transition metal dichalcogenide nanosheets, *Nat. Chem.*, 2013, **5**(4), 263–275.
152 M. Zhao, *et al.*, Advances in two-dimensional materials for optoelectronics applications, *Crystals*, 2022, **12**(8), 1087.
153 L. Jiao, *et al.*, Layer-dependent photoresponse of 2D MoS 2 films prepared by pulsed laser deposition, *J. Mater. Chem. C*, 2019, **7**(9), 2522–2529.
154 H. Fang, *et al.*, High-Performance Single Layered WSe2 p-FETs with Chemically Doped Contacts, *Nano Lett.*, 2012, **12**(7), 3788–3792.
155 A. Allain, *et al.*, Electrical contacts to two-dimensional semiconductors, *Nat. Mater.*, 2015, **14**(12), 1195–1205.
156 W. Shi, *et al.*, Raman and photoluminescence spectra of two-dimensional nanocrystallites of monolayer WS2 and WSe2, *2D Mater.*, 2016, **3**(2), 025016.
157 T. C. Berkelbach, M. S. Hybertsen and D. R. Reichman, Theory of neutral and charged excitons in monolayer transition metal dichalcogenides, *Phys. Rev. B:Condens. Matter Mater. Phys.*, 2013, **88**(4), 045318.
158 I. A. Al-Ani, *et al.*, Enhanced strong coupling of TMDC monolayers by bound state in the continuum, *Laser Photonics Rev.*, 2021, **15**(12), 2100240.
159 X. Tang, *et al.*, High-performance, self-powered flexible MoS 2 photodetectors with asymmetric van der Waals gaps, *Phys. Chem. Chem. Phys.*, 2022, **24**(12), 7323–7330.
160 Y. Ma, *et al.*, High-performance flexible WSe2 flake photodetector with broadband detection capability, *AIP Adv.*, 2020, **10**(12), 125027-1–125027-7.
161 C. Zhou, *et al.*, Self–driven metal–semiconductor–metal WSe2 photodetector with asymmetric contact geometries, *Adv. Funct. Mater.*, 2018, **28**(45), 1802954.
162 C. Yan, *et al.*, Highly Efficient Utilization of High–Energy Excitons in Multilayer WSe2 for Self–Powered Ultraviolet Photodetector With Near–Unity External Quantum Efficiency, *Laser Photonics Rev.*, 2024, **18**(12), 2400951.
163 C. Zhou, *et al.*, Self-Driven Metal–Semiconductor–Metal WSe2 Photodetector with Asymmetric Contact Geometries, *Adv. Funct. Mater.*, 2018, **28**(45), 1802954.
164 M. Long, *et al.*, Progress, challenges, and opportunities for 2D material based photodetectors, *Adv. Funct. Mater.*, 2019, **29**(19), 1803807.
165 H. Zhou, *et al.*, van der Waals MoS2/two-dimensional perovskite heterostructure for sensitive and ultrafast subband-gap photodetection, *ACS Appl. Mater. Interfaces*, 2022, **14**(2), 3356–3362.
166 G. Wang, *et al.*, Exploring a high-carrier-mobility black phosphorus/MoSe2 heterostructure for high-efficiency thin film solar cells, *Sol. Energy*, 2022, **236**, 576–585.
167 A. Chaves, *et al.*, Bandgap engineering of two-dimensional semiconductor materials, *npj 2D Mater. Appl.*, 2020, **4**(1), 29.
168 D. H. Jung, *et al.*, High-performance and high-stability LaVO3/Si solar cells through employing thickness-controlled LaVO3 and a titanium oxide passivation layer, *J. Alloys Compd.*, 2022, **904**, 163818.
169 M. Jellite, *et al.*, Investigation of LaVO3 based compounds as a photovoltaic absorber, *Sol. Energy*, 2018, **162**, 1–7.
170 L. Wang, *et al.*, Device performance of the mott insulator LaVO 3 as a photovoltaic material, *Phys. Rev. Appl.*, 2015, **3**(6), 064015.
171 S. J. Gharetape, *et al.*, Effect of vanadium deficiency on properties of polycrystalline LaVO3, *Appl. Phys. Lett.*, 2011, **98**(5), 052509-1–052509-3.
172 J. Li, *et al.*, High performance of room-temperature NbSe2 terahertz photoelectric detector, *ACS Appl. Mater. Interfaces*, 2022, **14**(12), 14331–14341.
173 J. Jang, *et al.*, Fermi–Level Pinning–Free WSe2 Transistors via 2D van der Waals Metal Contacts and Their Circuits, *Adv. Mater.*, 2022, **34**(19), 2109899.
174 H. Kim, Z. Wang and H. N. Alshareef, MXetronics: Electronic and photonic applications of MXenes, *Nano Energy*, 2019, **60**, 179–197.
175 K. Hantanasirisakul and Y. Gogotsi, Electronic and optical properties of 2D transition metal carbides and nitrides (MXenes), *Adv. Mater.*, 2018, **30**(52), 1804779.
176 K. R. G. Lim, *et al.*, Fundamentals of MXene synthesis, *Nat. Synth.*, 2022, **1**(8), 601–614.
177 K. Hantanasirisakul, *et al.*, Fabrication of Ti3C2Tx MXene transparent thin films with tunable optoelectronic properties, *Adv. Electron. Mater.*, 2016, **2**(6), 1600050.
178 X. Xu, *et al.*, Status and prospects of MXene-based nanoelectronic devices, *Matter*, 2023, **6**(3), 800–837.
179 Y. Liu, H. Xiao and W. A. Goddard III, Schottky-barrier-free contacts with two-dimensional semiconductors by surface-engineered MXenes, *J. Am. Chem. Soc.*, 2016, **138**(49), 15853–15856.
180 W. Song, *et al.*, Self–powered MXene/GaN van der Waals heterojunction ultraviolet photodiodes with superhigh efficiency and stable current outputs, *Adv. Mater.*, 2021, **33**(27), 2101059.
181 Y. Ding, *et al.*, Self-powered MXene/GaN van der Waals Schottky ultraviolet photodetectors with exceptional responsivity and stability, *Appl. Phys. Rev.*, 2024, **11**(4), 041413-1–041413-13.
182 Y. Ding, *et al.*, Self-powered MXene/GaN van der Waals Schottky ultraviolet photodetectors with exceptional responsivity and stability, *Appl. Phys. Rev.*, 2024, **11**(4), 041413.
183 L. Chu, *et al.*, Enhanced performance in self-powered photodetectors enabled by MXene/ZnO/Si pyramid structure, *Ceram. Int.*, 2025, **51**(7), 9030–9038.
184 M. Tian, *et al.*, Harnessing the Power of Nano–Ferroelectrics: BaTiO3/MXene (Ti3C2Tx) Composites for Enhanced Lithium Storage, *Adv. Energy Mater.*, 2024, **14**(43), 2401988.
185 Y. Feng, *et al.*, High dielectric and breakdown properties achieved in ternary BaTiO3/MXene/PVDF nanocomposites with low-concentration fillers from enhanced interface polarization, *Ceram. Int.*, 2019, **45**(6), 7923–7930.
186 S. Sha, *et al.*, Ferro-Pyro-Phototronic Effect Enhanced Self-Powered UV Photodetectors Based on BaTiO3@ MXene/

4H-SiC Heterojunction, *ACS Photonics*, 2024, **11**(10), 4472–4485.

187 H. Qiao, *et al.*, Self–powered photodetectors based on 2D materials, *Adv. Opt. Mater.*, 2020, **8**(1), 1900765.

188 D. Guo, *et al.*, Self-powered ultraviolet photodetector with superhigh photoresponsivity (3.05 A/W) based on the GaN/Sn: Ga2O3 pn junction, *ACS Nano*, 2018, **12**(12), 12827–12835.

189 S. Sha, *et al.*, High-performance, low-power, and flexible ultraviolet photodetector based on crossed ZnO microwires pn homojunction, *Photonics Res.*, 2024, **12**(4), 648–662.

190 C. Tan, *et al.*, A self-powered photovoltaic photodetector based on a lateral WSe2-WSe2 homojunction, *ACS Appl. Mater. Interfaces*, 2020, **12**(40), 44934–44942.

191 Y. Xu, *et al.*, High performance near infrared photodetector based on in-plane black phosphorus pn homojunction, *Nano Energy*, 2020, **70**, 104518.

192 Q. Cao, *et al.*, Realizing stable p-type transporting in two-dimensional WS2 films, *ACS Appl. Mater. Interfaces*, 2017, **9**(21), 18215–18221.

193 F. Zhang, *et al.*, Carbon doping of WS2 monolayers: Bandgap reduction and p-type doping transport, *Sci. Adv.*, 2019, **5**(5), eaav5003.

194 Y. Li, *et al.*, Lateral WSe2 homojunction through metal contact doping: Excellent self–powered photovoltaic photodetector, *Adv. Funct. Mater.*, 2023, **33**(17), 2213385.

195 W. Huang, *et al.*, Recent advances in semiconducting monoelemental selenium nanostructures for device applications, *Adv. Funct. Mater.*, 2020, **30**(42), 2003301.

196 W. Huang, *et al.*, Recent advances in functional 2D MXene–based nanostructures for next–generation devices, *Adv. Funct. Mater.*, 2020, **30**(49), 2005223.

197 G. Zhang, *et al.*, Self-powered photodetector of GaN/Sc 2 CCl 2 heterojunction with high carrier mobility and polarization sensitivity, *Phys. Chem. Chem. Phys.*, 2025, 6875–6886.

198 W. Liu, *et al.*, High–Performance Infrared Self–Powered Photodetector Based on 2D van der Waals Heterostructures, *Adv. Funct. Mater.*, 2025, 2421525.

199 F. Larki, A. Dehzangi, A. Abedini, M. R. Buyong, H. Tavako, P. Kameli and H. Salamati, Two-Dimensional Material Based Photodetector for Near Infrared Detection, *arXiv*, 2025, preprint, arXiv:2502.10680, DOI: 10.48550/arXiv.2502.10680.

200 Y. Tian, *et al.*, Recent Developments of Advanced Broadband Photodetectors Based on 2D Materials, *Nanomaterials*, 2025, **15**(6), 431.

201 H. Wang, *et al.*, Self-powered broadband photodetector based on mos2/sb2te3 heterojunctions: a promising approach for highly sensitive detection, *Nanophotonics*, 2022, **11**(22), 5113–5119.

202 J. Yang, *et al.*, Visible-light self-powered photodetector with high sensitivity based on the Type-II Heterostructure of CdPSe3/MoS2, *ACS Appl. Mater. Interfaces*, 2024, **16**(25), 32334–32343.

203 W. S. Yun and J. Lee, Single-layer CdPSe3: A promising thermoelectric material persisting in high temperatures, *Appl. Phys. Lett.*, 2019, **115**(19), 193105-1–193105-5.

204 M. A. Khan, *et al.*, Photonic Synapse of CrSBr/PtS2 Transistor for Neuromorphic Computing and Light Decoding, *Adv. Funct. Mater.*, 2024, **34**(52), 2410974.

205 Y. Xiong, T. Chen and W. Feng, Broadband self-powered photodetector based on the large-area continuous WS0. 9Se1. 1 film, *Opt. Mater.*, 2023, **145**, 114412.

206 J. Panda, *et al.*, Polarization-resolved position-sensitive self-powered binary photodetection in multilayer janus CrSBr, *ACS Appl. Mater. Interfaces*, 2023, **16**(1), 1033–1043.

207 S. Maity and P. Kumar, A synergistic heterojunction of SnS 2/SnSSe nanosheets on GaN for advanced self-powered photodetectors, *Nanoscale Horiz.*, 2024, **9**(8), 1318–1329.

208 W. Wu, *et al.*, Self-powered photovoltaic photodetector established on lateral monolayer MoS2-WS2 heterostructures, *Nano Energy*, 2018, **51**, 45–53.

209 R. Zhuo, *et al.*, High-performance self-powered deep ultraviolet photodetector based on MoS 2/GaN p–n heterojunction, *J. Mater. Chem. C*, 2018, **6**(2), 299–303.

210 A. Qadir, *et al.*, Recent advancements in polymer-based photodetector: A comprehensive review, *Sens. Actuators, A*, 2024, 115267.

211 Z. Wang, *et al.*, Flexible near-infrared organic photodetectors for emergent wearable applications, *Wearable Electron.*, 2024, **1**, 53–77.

212 J. Chen, *et al.*, Self-powered flexible sensors: from fundamental mechanisms toward diverse applications, *Int. J. Extreme Manuf.*, 2024, **7**(1), 012011.

213 M. Peng, Z. Wen and X. Sun, Recent progress of flexible photodetectors based on low–dimensional II–VI semiconductors and their application in wearable electronics, *Adv. Funct. Mater.*, 2023, **33**(11), 2211548.

214 S. Aftab, *et al.*, Advancements in nanomaterials for solar energy harvesting: Challenges, innovations, and future prospects, *Chem. Eng. J.*, 2025, **516**, 164224.

215 T. T. Nguyen, *et al.*, Flexible and transparent MXene-platformed ultrafast photodetector for encrypted signal communication in self-powered operation, *Nano Energy*, 2023, **109**, 108331.

216 Y. Liu, *et al.*, Flexible self-powered solar-blind Schottky photodetectors based on individual Ga 2 O 3 microwire/MXene junctions, *CrystEngComm*, 2023, **25**(37), 5324–5333.

217 W. Liao, *et al.*, van der Waals heterostructures for optoelectronics: Progress and prospects, *Appl. Mater. Today*, 2019, **16**, 435–455.

218 S. Aftab, *et al.*, Flexible perovskite solar cells: A revolutionary approach for wearable electronics and sensors, *Mater. Today Energy*, 2025, **51**, 101872.

219 A. Rani, A. Verma and B. C. Yadav, Advancements in transition metal dichalcogenides (TMDCs) for self-powered photodetectors: challenges, properties, and functionalization strategies, *Mater. Adv.*, 2024, **5**, 3535–3562.

220 X. Tang, *et al.*, Wafer-Scale Vertical 1D GaN Nanorods/2D MoS2/PEDOT: PSS for Piezophototronic Effect-Enhanced

Self-Powered Flexible Photodetectors, *Nano-Micro Lett.*, 2025, **17**(1), 1–15.

221 X. Tang, *et al.*, Wafer-scale vertical 1D GaN nanorods/2D MoS2/PEDOT: PSS for piezophototronic effect-enhanced self-powered flexible photodetectors, *Nano-Micro Lett.*, 2025, **17**(1), 56.

222 D. Periyanagounder, *et al.*, High performance, self-powered photodetectors based on a graphene/silicon Schottky junction diode, *J. Mater. Chem. C*, 2018, **6**(35), 9545–9551.

223 H. G. Shin, *et al.*, Vertical and in-plane current devices using NbS2/n-MoS2 van der Waals Schottky junction and graphene contact, *Nano Lett.*, 2018, **18**(3), 1937–1945.

224 M. H. Pervez, *et al.*, Recent Developments on Novel 2D Materials for Emerging Neuromorphic Computing Devices, *Small Struct.*, 2025, **6**(2), 2400386.

225 L. Tong, *et al.*, Self-driven Gr/WSe2/Gr photodetector with high performance based on asymmetric Schottky van der Waals contacts, *ACS Appl. Mater. Interfaces*, 2023, **15**(49), 57868–57878.

226 H. Ghanbari, *et al.*, 2D MoSe2 Geometrically Asymmetric Schottky Photodiodes, *Adv. Opt. Mater.*, 2024, **12**(34), 2401682.

227 L. Tong, *et al.*, Self-driven Gr/WSe2/Gr photodetector with high performance based on asymmetric Schottky van der Waals contacts, *ACS Appl. Mater. Interfaces*, 2023, **15**(49), 57868–57878.

228 D. Yoon, *et al.*, Perovskite Stannate Heterojunctions for Self–Powered Ultraviolet Photodiodes Operated in Extreme Environments, *Adv. Electron. Mater.*, 2024, **10**(5), 2300530.

229 C. Perumal Veeramalai, *et al.*, Lead–halide perovskites for next-generation self-powered photodetectors: a comprehensive review, *Photonics Res.*, 2021, **9**(6), 968–991.

230 S. Aftab, *et al.*, Perovskite Quantum Dots: Fabrication, Degradation, and Enhanced Performance Across Solar Cells, Optoelectronics, and Quantum Technologies, *Carbon Energy*, 2025, **7**, e70018.

231 M. Pramanik, *et al.*, High-Performance Broadband Self-Driven Photodetector Based on MoS2/Cs2CuBr4 Heterojunction, *ACS Appl. Mater. Interfaces*, 2024, **16**(29), 38260–38268.

232 L. Guo, *et al.*, A self–powered UV photodetector with ultra-high responsivity based on 2D perovskite ferroelectric films with mixed spacer cations, *Adv. Mater.*, 2023, **35**(47), 2301705.

233 T. Yan, *et al.*, Large–area 2D perovskite oxides/organic heterojunction enables highly–sensitive self–powered photodetector for ultraviolet light communication, *Adv. Funct. Mater.*, 2024, **34**(10), 2311042.

234 E. Elahi, *et al.*, Emerging avalanche field-effect transistors based on two-dimensional semiconductor materials and their sensory applications, *J. Mater. Chem. C*, 2025, **13**(31), 15767–15795.